Diploma Thesis

Nanoindentation of ultra-fine grained and nanoporous Au at elevated temperatures

Alexander Leitner

This work has been carried out at the Department of Materials Physics, Montanuniversität Leoben, Austria in cooperation with the Department of Nuclear Engineering, University of California, Berkeley, USA.

December 2, 2014

Affidavit

I declare in lieu of oath, that I wrote this thesis and performed the associated research myself, using only literature cited in this volume.

Eidesstattliche Erklärung

Ich erkläre an Eides statt, dass ich diese Arbeit selbstständig verfasst, andere als die angegebenen Quellen und Hilfsmittel nicht benutzt und mich auch sonst keiner unerlaubten Hilsmittel bedient habe.

December 2, 2014 Alexander Leitner

Acknowledgments

First of all I would like to thank my adviser Assoc. Prof. Daniel Kiener for making this thesis possible and giving me the opportunity to be capable of independent scientific work on the one hand but providing me great support for all intents and purposes on the other hand.

Needless to say, I am indebted to the entire Department of Material Physics, in particular I would like to thank Dr. Verena Maier for many useful advices concerning nanoindentation and Dr. Stefan Wurster for the strong support during my preparations in Leoben. Moreover my sincere thanks go to Silke Modritsch and Dipl.-Ing. Peter Kutleša for their technical assistance.

In addition I am much obliged to the entire Department of Nuclear Engineering at UC Berkeley, especially to Prof. Peter Hosemann for hosting me in his group and his scientific support. Thanks to Dr. Manuel David Abad for the extensive training on the nanoindenter and his assistance during my experiments as well as to AJ Gubser for the attendance at the FIB/SEM at UC Berkeley.

I owe the Austrian Marshall Plan Foundation a debt of gratitude for its generous financial support, without which this work would not have been possible.

My family has a big part on the success of my studies, especially my parents who enabled me a completely carefree study and always lend an ear for my issues and my brother for providing me lots of great advices in the past years.

Furthermore I would like to give props to all my fellow students who made the last few years very special, particularly the so-called "mule-troop" for having so many merrily adventures and discussions together.

Finally, I would like to thank my beloved wife, not just for supporting me in any possible way but for sharing so many cheerful moments in the past years, I could not imagine a better companion.

Abstract

Nanostructured materials provide unique mechanical properties and hence are convenient for high-performance applications. However, high temperature data is seldom and the governing deformation mechanisms are insufficiently explored so far. In order to investigate the behavior of face centered cubic metals in harsh environments, such as high temperature conditions, Au lend itself as an appropriate candidate to study deformation dynamics due to its high oxidation resistance.

The influence of different interphases was examined by opposing ultra-fine grained gold (ufg Au) with a grain size of about 250 nm to nanoporous gold (np Au). Gold powder was used as a base material and subsequently consolidated via high pressure torsion. Likewise a Au/Fe powder mixture was densified to create a nanostructured composite. For the latter a subsequent selective etching process removed the iron and left behind a novel foam with ligaments in the order of 100 nm and a porosity of 50 %. Additionally, a sample each with coarse grained (cg) and nanocrystalline (nc) structure was prepared through eligible annealing and by adding low amounts of Cu, respectively. The following microstructural evolution, using amongst other scanning electron microscopy, electron backscatter diffraction and energy dispersive X-ray spectroscopy, allowed a precise characterization of the fabricated nanomaterials.

Depth sensing nanoindentation enables the determination of fundamental mechanical properties such as hardness and Young's modulus. Strain-rate sensitivity m and activation volume V^* were inferred from relaxation data of a hold segment at maximum. The latter two are feasible parameters for the indication of the predominating deformation mechanism. Accurate nanoindentation experiments were performed at ambient temperature for all four types of samples and at high temperature up to 300 °C for ufg Au as

well as np Au. Subsequently, cross-sections of indents were prepared with a focused ion beam. Those allowed to show the plastic deformation beneath the indenter tip. In case of np Au porosity maps could be created to illustrate zones of significant densification.

The calculated yield strength of the ligaments of nanoporous Au at RT was determined to be 1.6 GPa and thus close to the theoretical strength of gold. A layer was absorbed to the surface at HT, most likely through insufficient thermal stability of ceramic components of the experimental setup. Nevertheless, nanoindentation tests provide feasible data and exhibit a decrease of hardness at elevated temperatures. Ufg Au exceeds the hardness of its coarse grained counterpart by far. High temperature data show, however, that the hardness decreases to less than 15 % with regard to the RT value of 1.6 GPa when 300 °C are reached. Within the entire tested temperature range np Au and ufg Au show a significant strain-rate dependence ($m > 0.03$) and low activation volumes (< 75 b^3). Hence, it is suggested that for both, np Au and ufg Au, that the plastic deformation is controlled by dislocation/interphase interactions. While the microstructure has a crucial impact on the governing deformation mechanism, the type of interphase does not have a decisive influence. On the other hand, cg Au exhibits a high activation volume at RT (> 100 b^3), which is associated with the cutting of forest dislocations.

Eventually, this study demonstrates the influence of interphase type and structure size on the mechanical properties and deformation dynamics of ultra-fine grained and nanoporous face centered cubic metals. Thus, this thesis contributes considerably to a better understanding of the mechanical behavior of novel metal nanostructures at room and elevated temperatures.

Kurzfassung

Nanostrukturierte Materialien zeichnen sich durch ihre einzigartigen mechanischen Eigenschaften aus und finden dadurch Anwendung in diversen Hochleistungsbauteilen. Die auftretenden Verformungsmechanismen dieser Materialklasse sind bisher unvollständig erforscht, insbesondere gibt es kaum Daten im Hochtemperaturbereich. Um das Verformungsverhalten kubisch flächenzentrierter Materialen bei erhöhten Temperaturen zu untersuchen, empfiehlt sich Gold aufgrund seines hohen elektrochemischen Potentials und der dadurch stark reduzierten Oxidationsneigung.

Der Einfluss zweier unterschiedlicher Grenzflächentypen wurde untersucht. Dazu wurde nanoporöses Gold mit hohem Oberflächen/Volumen-Verhältnis, ultra-feinkörnigem Gold (Korngröße rund 250 nm) mit hohem Korngrenzenanteil gegenübergestellt. Goldpulver wurde durch Hochdrucktorsionsverformung (HPT) zu scheibenförmigen Proben verdichtet wurde. Eine Au/Fe Pulvermischung diente als Basismaterial zur Herstellung des Goldschaumes. Nach der Konsolidierung wurde der Eisenanteil durch selektives Ätzen entfernt, wodurch eine Goldstruktur mit einer Porosität von etwa 50 % und Ligamenten mit einem Durchmesser von rund 100 nm entsteht. Durch geeignete Wärmebehandlung bzw. durch Legieren mit kleinen Anteilen von Kupfer je eine grobkörnige bzw. nanokristalline Goldprobe vorbereitet werden. Die Charakterisierung der Mikrostruktur aller Proben erfolgte mittels Rasterelektronenmikroskop, Elektronenrückstreubeugung und energiedispersiver Röntgenspektroskopie.

Nanoindentierung stellt eine adäquate Methode zur Bestimmung fundamentaler mechanischer Kennwerte, wie Härte (H) und E-Modul, dar. Ebenso können die Dehnratenabhängigkeit m und das Aktivierungsvolumen V^* aus den Relaxationsdaten während eines Haltesegments bei maximaler Last bestimmt werden. Diese Parameter geben Auskunft

über dominierende Verformungsmechanismen. Versuche wurden für alle Probentypen bei Raumtemperatur (RT) durchgeführt, nanoporöses Au und ultra-feinkörniges Au wurden zusätzlich bei erhöhten Temperaturen (HT) bis 300 °C getestet. Nachträglich angefertigte Querschnitte der Indents zeigen die plastische Verformung generell und im Fall des porösen Materials die Verdichtung unter der Indenterspitze.

Die berechnete Fließgrenze der Ligamente des Schaumes bei Raumtemperatur liegt mit 1.6 GPa nahe der theoretischen Festigkeit von Gold. Nach Hochtemperaturmessungen wurde ein Niederschlag auf den Probenoberflächen beobachtet, welcher sich vermutlich durch thermische Instabilität des Versuchsaufbaus gebildet hat. Nichtsdestotrotz liefern die Messungen aussagekräftige Ergebnisse und zeigen einen zu erwartenden Abfall der Härte bei erhöhten Temperaturen. Das ultra-feinkörnige Gold übersteigt die Härte seines grobkörnigen Gegenstückes deutlich. Eine massive Reduzierung der Härte bei steigender Temperatur ist beobachtbar, bei 300 °C entspricht H nur mehr 15 % des RT Wertes, der bei 1.6 GPa liegt. Beide nanostrukturierten Materialien weisen im gesamten getesteten Temperaturbereich eine signifikante Dehnratenabhängigkeit auf ($m > 0.03$), verbunden mit niedrigem Aktivierungsvolumen (< 75 b^3). Dies lässt vermuten, dass Grenzflächen/Versetzungs-Wechselwirkungen den Verformungsprozess dominieren. Offensichtlich spielt der Typ der Grenzfläche nur eine untergeordnete Rolle, wohingegen die Strukturgröße einen entscheidenden Einfluss auf Eigenschaften des Materials nimmt. Im Gegensatz dazu weist das grobkörnige Gold bereits bei RT ein hohes Aktivierungsvolumen (> 100 b^3) auf, welches mit dem Schneiden von Waldversetzungen assoziiert wird.

Die Arbeit zeigt den Einfluss von Parametern, wie Grenzflächentyp und Strukturgröße auf die mechanischen Eigenschaften und das Verformungsverhalten in ultra-feinkörnigem und nanoporösem kubisch flächenzentrierten Metallen. Dadurch kann wesentlich zu einem besseren Verständnis des mechanischen Verhaltens dieser recht jungen Materialklasse beigetragen werden.

Abbreviations and Symbols

A_c	.....	Projected contact area
ARB	.....	Accumulative roll bonding
bcc	.....	Body centered cubic
C^*	.....	Constraint factor
cBN	.....	Cubic boron nitride
cg	.....	Coarse grained
DC	.....	Displacement controlled
E	.....	Young's modulus
E_r	.....	Reduced modulus
ECAP	.....	Equal channel angular pressing
EDX	.....	Energy dispersive X-ray spectroscopy
fcc	.....	Face centered cubic
FIB	.....	Focused ion beam
GBS	.....	Grain boundary sliding
H	.....	Hardness

hcp	.....	Hexagonal closed packed
HV	.....	Vickers Hardness
HPT	.....	High Pressure Torsion
HT	.....	High temperature
LC	.....	Load controlled
LM	.....	Light microscope
m, SRS	.....	Strain-rate sensitivity
nc	.....	Nanocrystalline
np	.....	Nanoporous
pc	.....	Polycrystalline
Q_a	.....	Activation energy
R	.....	Universal gas constant
RT	.....	Room temperature
S	.....	Stiffness
sc	.....	Single crystalline
SEM	.....	Scanning electron microscope
T	.....	Temperature
ufg	.....	Ultra-fine grained
V^*	.....	Activation volume
ϵ	.....	Geometry factor
ε	.....	Strain

ν ..... Poisson's ratio

ρ ..... Density

σ_f ..... Flow stress

Contents

1. Introduction

During the past decades the interest in nanoporous foams significantly increased, which is proofed by the recent rise of publications regarding to this class of matter. On the one hand, this is justified by excellent mechanical properties of these materials for various technical applications such as catalytic substrates [1]. On the other hand, equipment and examination methods with a resolution down to the magnitude of nanometers became accessible in the past decades and made it possible to investigate nanostructures [2–4].

Nanoporous materials possess a high surface-to-volume-ratio which is crucial for high effective catalyze processes. Recent outcomes also show that porous materials feature a radiation-resistant behavior through annihilation effects if they have a well-defined ligament size as reported by Bringa *et al.* [5] and consequently retrieve a high potential for reactor applications. In the sector of alternative power engineering, foams are presumed to be a promising material for purposes relating to solar modules and fuel cells. The same holds true for the dedication in the field of biology where foams are used for different types of sensors, for instance DNA-sensors which are made of nanoporous gold electrodes [6]. Another interesting property was recently discovered from Xue *et al.*, who observed that imbibition effects can be controlled by an applied electric potential [7].

Due to their nanostructure the deformation behavior and consequently their mechanical properties cannot be described by classical theories anymore [8, 9]. By way of example, the reduced number of dislocation sources has to be considered as well as the limited motion of dislocations and their interaction with limiting interfaces [10]. If the ligament

size decreases to 10 nm or smaller they are even supposed to be dislocation-free which was verified by Volkert *et al.* [11]. The influence on mechanical and physical properties regarding to different types of interfaces, such as grain boundaries compared to free surfaces, is still insufficiently explored.

The majority of nanoporous metal foams is fabricated by dealloying techniques [11, 12]. Scientific reports about the production of porous materials based on powders with subsequent selective etching are seldom. However, in order to acquire a better understanding of those materials it is necessary to examine their response to mechanical stresses. Therefore, it is inevitable to experimentally determine fundamental strength parameters using methods such as nanoindentation [2], which is an eminent technique to investigate foams at room temperature (RT) as wells as at elevated temperatures.

There is no doubt that nanoporous materials play a major role in cutting-edge science and involve an enormous innovation potential. Thus, it is indispensable to determine the ruling deformation mechanisms by measuring deformation dynamic parameters such as strain-rate sensitivity and activation volume. We hope that our study concerning the mechanical properties of ufg and np Au will contribute to the body of knowledge.

2. Theoretical background

2.1. Gold

From time immemorial humanity was fascinated of gold (lat. Aurum). At excavations of settlements in the area of Euphrat and Tigris, today's Iraq, gold could be substantiated in human's property in the age of Paleolithic. It was the first metal which found its way into the life of human being. Most likely this results from the fact that solid gold can be found in nature since the high electrochemical potential makes Au highly resistant against corrosive attack under environmental conditions on earth. For the first time ever gold was used as a mean of payment in 2700 BC, therefore it can be called the oldest currency in the world with a clear conscience [13].

It is a fortunate coincidence that gold is available on planet earth as it cannot emerge from fusion, the process in which more frequent metals such as iron are generated. How gold can be created in the universe is unexplained so far but current research projects investigate the cases of collisions between neutron stars and supernovas [14]. Fragments of those exceeding events could have clashed with the earth during its formation 3.9 billion years ago and hence be responsible for the gold occurrence. Consequently, sources of Au are widespread and unequally distributed, the largest gold mine (Grasberg Mine) is situated in Papua, Indonesia. High amounts of this noble metal have also been found around South Africa, Iceland and Uzbekistan.

Chemical, physical as well as known mechanical properties of conventional pure gold, which will be used in the instant report, are displayed in table 2.1.

Table 2.1 Properties of pure bulk Au [15–19].

Atomic number	79
Standard atomic weight	197.0
Density	19.3 $g \cdot cm^{-3}$
Melting point	1063.0 K
Thermal conductivity	297.1 $W \cdot m^{-1} \cdot K^{-1}$
Bulk tensile strength	120 MPa
Young's modulus	80 GPa
Shear modulus	28 GPa
Poisson's ratio	0.44
Hardness	0.45 GPa
Lattice type	*face centered cubic* (fcc)
Burgers vector	0.2884 nm
Stacking fault energy	32 $mJ \cdot m^{-2}$
HPT - Steady state hardness	804 MPa
HPT - Steady state grain size	520 nm

2.2. Methods of severe plastic deformation

In order to fabricate materials with grain sizes down to the magnitude of nanometers methods of severe plastic deformation can be used. Beside High Pressure Torsion (HPT), which was used to manufacture specimens for the present report, equal channel angular pressing (ECAP) and accumulative roll bonding (ARB) fall into this category. However, technical details aside, the principle is similar, by applying high shear stresses and

consequently large strains the microstructure of metals can be refined to an ultra-fine grained ($d < 500$ nm) or even nanocrystalline ($d < 100$ nm) level. HPT additionally provides the opportunity to consolidate powders easily and was therefore chosen for the production of the investigated gold and compound samples.

2.2.1. High Pressure Torison

HPT was established in the course of investigations concerning the behavior of materials under high pressure. Prof. Bridgman, a lecturer of Harvard University, realized that a material can endure very high strains through torsion, if it is exposed to compressive forces. A schematic sketch can be seen in figure 2.1. There are different procedures, mainly distinguished between constrained and unconstrained mode. The samples of this report were produced under quasi-constrained conditions at which the better part of the specimen is placed in the cavities of the two anvils but through a small gap a limited outflow of material is possible (2.1 c)). The properties of the deformed material strongly depend on the applied pressure as wells as on the number of revolutions. Finally the shear strain is given by

$$\gamma = \frac{2 \cdot \pi \cdot N \cdot r}{h}, \tag{2.1}$$

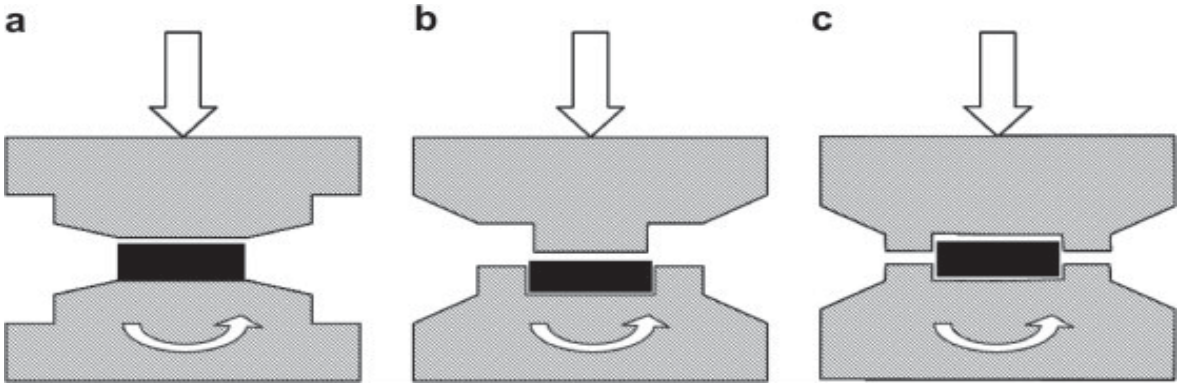

Figure 2.1 Different possibilities for HPT disk fabrication: a) unconstrained, b) constrained and c) quasi-constrained [20].

where N is the number of revolutions, r is the distance to the center of the disk and h is the thickness of the sample. The accumulative strain ε can be calculated by an estimate which was suggested by researchers in 1980 and is used most frequently in scientific publications [20]:

$$\varepsilon = ln(\frac{2 \cdot \pi \cdot N \cdot r}{h}). \tag{2.2}$$

It is obvious that no shear strain is induced in the center of the specimen at $r = 0$ and consequently no hardening is expected through the HPT process. In radial direction the hardness of the sample increases with rising distance to the center due to higher occurring strains. Additionally to the number of revolutions, the applied pressure influences this curve, too [20]. Principally, higher compressive forces and a rising number of revolutions lead to higher hardness levels. However, every material has specific steady state properties thus the grain size and hardness are limited to certain values and cannot be changed by further processing of HPT [21]. Face centered cubic materials with high stacking fault energies such as aluminum show a peak of hardness during deformation which decreases after continuing the distortion [22]. Gold is not expected to show that behavior as its stacking fault energy is considered low with a value of 32 $\mathrm{mJ} \cdot \mathrm{m}^{-2}$ [19].

2.3. Microhardness

The hardness value of materials is an important parameter for its mechanical behavior and can be determined by different methods such as Brinell, Vickers or Rockwell. In this report the microhardness was measured by Vickers, where a pyramid made of diamond with an opening angle of 136° penetrates the specimen under a selected load. By using the diagonals d_1 and d_2 of the indent after the load is relieved and known weight F the hardness can be calculated by dividing the force by the surface area of the indentation

$$HV = \frac{0.189 \cdot F}{(\frac{d_1+d_2}{2})^2}. \tag{2.3}$$

In literature it is more common to convert the hardness into the unit of MPa by multiplying the value with a factor of 9.807. Microhardness measurements across the specimen's diameter provide information about the success of the HPT-processing due to the correlation between the hardness and the degree of deformation.

2.4. Mechanical behavior of np metal foams

Most of the published investigations on foams are based on the work of Gibson and Ashby [23], where the elastic-plastic behavior is extensively described. Particularly their equations for the flow stress (equation 2.4) as well as the Young's modulus (equation 2.5) in dependence of the foams porosity are often cited and are given by:

$$\sigma_f^* = C_1 \cdot \sigma_{f_s} \cdot \left(\frac{\rho^*}{\rho_s}\right)^p \tag{2.4}$$

$$E^* = C_2 \cdot E_s \cdot \left(\frac{\rho^*}{\rho_s}\right)^q \tag{2.5}$$

with σ_{f_s} as flow stress, E_s the Young's modulus and ρ_s the density of a solid bulk sample, while using σ_f^* as flow stress, E^* the Young's modulus and ρ^* of the porous foam. C_1 and C_2 are constants ascribed to the cell geometry, whereas for open-cell foams in the present work the values are supposed to be $C_1 = 0.3$ and $C_2 = 1$, respectively. p and q refer to the deformation process of the cells, with suggested values of $p = 1.5$ and $q = 2$ typically associated with ligament bending [23]. However, those assumptions relate to macroscopic foams, therefore a modification for nanoporous foams were previously discussed [11, 12, 24, 25]. Good accordance was found for the Young's modulus, otherwise the flow stress of np foams appear much higher than expected from equation 2.4. As the ligament size decreases down to the magnitude of nanometers and thus dislocation movement is limited it was proposed to use the theoretical strength of the material instead of σ_{f_s}. Another possibility is to use a Hall-Petch like ansatz, first published by

Hodge *et al.* [26], whereupon the physical background is disputable.

In addition further mechanical properties have to be discussed for metal foams. The Poisson's ratio ν is expected to have significant lower values for foams and is often assumed to be $\nu = 0$ for low density foams [27]. This fact could neither be validated from Volkert *et al.* [11] for np Au foams, nor from Olurin *et al.* [28] for aluminum foams, both authors propose rather $\nu = 0.2$. A similar value was recently suggested by Briot *et al.* after their study on np Au compression and tensile tests [24]. Frequently, authors assume the condition under the indenter tip during the experiments to be unconstrained, which provides a constraint factor of $C^* \approx 1$ and results in $\sigma_f \approx H$ [29]. However, considering the non-zero value of ν the and the relation to C^*, a constraint factor of 2.5 seems to be more accurate [23]. Furthermore it must be noted that σ_f is related to the flow stress at 8 % strain for a Berkovich indenter [30], while Gibson and Ashby considered σ_y in their initial works [23].

2.5. Nanoindentation

The depth sensing method of nanoindentation displays a modern experimental procedure to measure mechanical properties at the nanoscale [2]. A tip penetrates a sample while recording load-displacement curves. By analyzing plots of load or depth controlled indentations, properties such as the sample's hardness, Young's modulus or strain-rate sensitivity can be determined. There are different tips which are used for nanoindentation, such as Berkovich, cube corner, conical or spherical indenters. In the following paragraphs the detailed calculation of mechanical properties values from nanoindentation data will be explained, whereas all equations refer to a Berkovich indenter since this is the type of tip used for the instant report. Figure 2.2 illustrates a schematic indent. As metals show a significant elastic recovery it is necessary to define different values for the height which distinguish between the plastic depth h_{plast} and the elastic depth

h_{elast}. Furthermore a curvature of the material appears around the indent during the load is applied which consequently reduces the projected contact area A_c. The actual contact area is calculated using the contact depth h_c which is the original indentation depth h subtracted by h_s. A schematic load-displacement graph is plotted in figure 2.3. The load can be applied in different modes, such as time controlled or with a fixed loading rate. Furthermore a constant strain-rate as well as a constant displacement rate can be realized. After reaching the set limit, a subsequent dwell segment follows which obtains data for calculating the strain rate sensitivity m. The unloading curve provides information about the sample's stiffness S and during a dwell segment at 20 % of the maximum load F_{max} the thermal drift correction data is calculated.

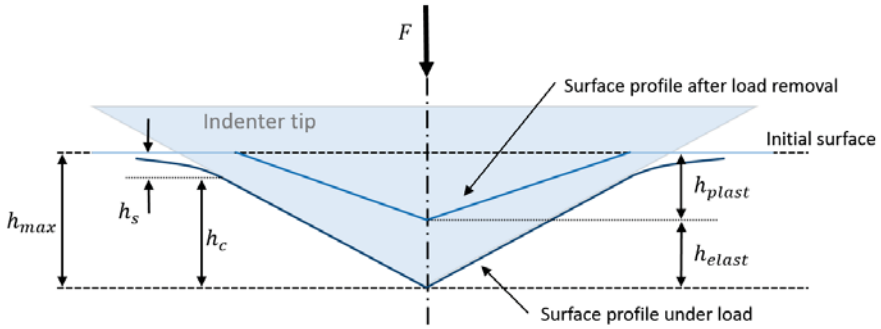

Figure 2.2 Illustration of an indent and during an experiment, defining different values for the height.

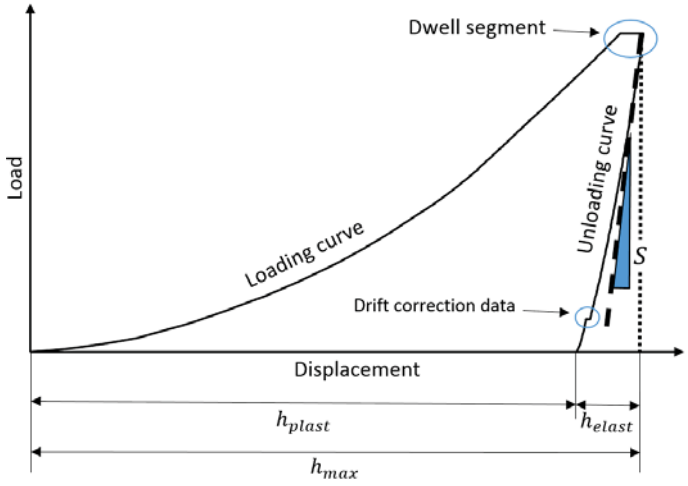

Figure 2.3 Typical load displacement plot of nanoindentation experiments.

2.5.1. Hardness and Young's modulus

Nanoindentation experiments output data provide amongst others values of F_{max}, S and h_c. Thereby the total stiffness of the system S_{tot} is determined by fitting the unloading curve first with

$$F = A \cdot (h - h_f)^q \tag{2.6}$$

whereat A, h_f and q are the fitting parameters. By deriving equation 2.6 and inserting h_{max} the stiffness is given as

$$S_{tot} = A \cdot q \cdot (h_{max} - h_f)^q. \tag{2.7}$$

It has to be taken into account that S_{tot}, respectively it's inverse the so-called compliance C_{tot} also contains the frame compliance C_f which depends on the entire machine setup. For this reason C_{tot} has to be subtracted by C_f to gain the compliance of the sample C_s in the end, as summed up by:

$$C_s = C_{tot} - C_f \tag{2.8}$$

$$S = \frac{1}{C_{tot} - C_f}. \tag{2.9}$$

As a result, h_c for a Berkovich indenter with the geometrical factor $\epsilon_{\mathrm{B}} = 0.75$ can be determined by equation

$$h_c = h_{max} - \epsilon_B \cdot \frac{F_{max}}{S}. \tag{2.10}$$

In order to calculate H by

$$H = \frac{P_{max}}{A_c} \tag{2.11}$$

it is necessary to know A_c which is estimated by using an approximate solution, called the area function $A_c(h_c)$, suggested by Oliver and Pharr [2], of the form

$$A_c(h_c) = C_1 \cdot h_c^2 + C_2 \cdot h_c + C_3 \cdot h_c^{\frac{1}{2}} + C_4 \cdot h_c^{\frac{1}{4}} + ... + C_9 \cdot h_c^{\frac{1}{128}}, \tag{2.12}$$

whereat $C_1 = 24.5$ describes an ideal Berkovich indenter and consequently the remaining constants $C_2, C_3 .... C_9 = 0$. Deviations from these numbers result from a dissenting geometry and can be accounted for calibrations which will be explained later.

Moreover, the Young's modulus can be calculated using the reduced modulus E_r given by

$$E_r = \frac{\sqrt{\pi}}{2 \cdot \beta} \cdot \frac{S}{\sqrt{A_C}}, \tag{2.13}$$

in which β is a depth independent factor, considering that the pyramidal shape of the indenter is not a body of revolution, with a value of 1.034 for a Berkovich indenter. E_r is affected by the mechanical properties of indenter and sample. However, considering the Young's modulus E_i and the Poisson's ratio ν_i of the indenter and ν_s for the specimen the Young's modulus of the tested material E_s can be determined from the relation

$$\frac{1}{E_r} = \frac{1 - \nu_i^2}{E_i} \cdot \frac{1 - \nu_s^2}{E_s}. \tag{2.14}$$

2.5.2. Calibrations

As can be seen from this procedure, the area function (equation (2.12)) and frame compliance (equation (2.9)) have a serious influence on the results and can cause significant errors. In order to get correct data it is inevitable to calibrate the nanoindenter by using an isotropic material with known mechanical properties, commonly fused silica ($E = 69.6$ GPa, $H = 8.85$ GPa, $\nu = 0.17$, [31]). About 100 indents with maximum loads over the whole accessible range are set, typically performed on fused quarz. From this data C_f can be identified by solving equations (2.11) and (2.13) for A_c and plotting the results over the corresponding maximum force. Using the least squares method by varying values for C_f, a solution can be found where the deviation of A_c values calculated from H and E_r for the corresponding force reach a minimum.

Likewise, the constants for $A_c(h_c)$ can be determined as well. As hardness and Young's

modulus for fused silica are supposed to be independent of the penetration depth, the function given by equation (2.12) is fitted with the method of least squares for the calculated values of A_c out of (2.11) and (2.13) this time varying the constants C_1 to C_9. The values of those constants also permit to draw conclusions on the actual shape of the indenter, e. g. in terms of tip rounding.

2.5.3. Determination of the strain-rate sensitivity

For describing the deformation dynamics of a material, the strain-rate sensitivity can serve as an indicator for the type of process occurring during plastic deformation. Values of $m \approx 0.5$ are referred to grain boundary sliding (GBS) [32], on the other hand $m \approx 1$ indicates boundary diffusion, also known as Coble creep [33]. Contrary to those highly thermally activated processes, athermal deformation mechanisms are characterized by a rather low value of m, such as dislocation glide in coarse grained fcc metals. By way of example cg Cu reveals a SRS lower than 0.01 [34].

There are different procedures described in literature to determine the strain-rate sensitivity, such as constant indentation strain-rate experiments [35], constant load (CL) tests [36], strain-rate jump tests [37] or microscratch testing [38]. Particularly CL and jump tests are of interest, as the strain-rate sensitivity m can be obtained from a single indent and therefore reduces the experimental effort. Peykov *et al.* verified that analyzing the data of a dwell segment at a constant load can provide reliable values for m [39], whereat a split in two time regimes is suggested. Maier *et al.* [40] proposed to plot the strain-rate sensitivity in dependence of the flow stress since two different values obtained from Peykov *et al.* can not be interpreted physically. Due to limited experimental capabilities the CL method was chosen to determine the stress-dependent m in this report and will be explained in the following paragraphs.

The strain-rate sensitivity m for a constant temperature T can be determined by using

the well-known power-law relation between strain-rate $\dot{\varepsilon}$ and stress σ

$$\sigma = K \cdot \dot{\varepsilon}^m. \tag{2.15}$$

Applying the logarithm and deviating equation (2.15) at constant temperature ends up in

$$m = \left(\frac{\partial \, ln \, H}{\partial \, ln \, \dot{\varepsilon}} \right)_T \tag{2.16}$$

since H is proportional to σ via the constraint factor C^*.

Figure 2.4 depicts the plot of a dwell segment at maximum load. In order to calculate the strain-rate an absolute depth h_a is defined, consisting of a time dependent part h_r and time independent depth h_0 at the beginning of the dwell time. To derive the time dependent strain-rate

$$\dot{\varepsilon} = \frac{\dot{h_a}}{h_a} \tag{2.17}$$

it is convenient to fit the time dependent part by a smooth function $h_r(t)$, where commonly

$$h_r(t) = A \cdot (t - B)^C + D \cdot t \tag{2.18}$$

is used, with A, B, C and D being fitting parameters calculated by using the method of least squares [39, 41]. Figure 2.4 demonstrates that this ansatz is well suited for the problem at hand.

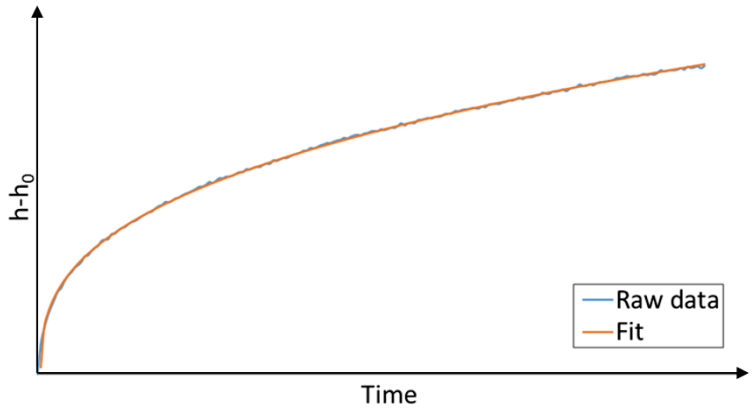

Figure 2.4 Schematic plot of dwell data and according fit.

By obtaining H from using equation (2.11) whereat $A_c(h_c)$ is calculated from the instantaneous contact depth h_c it is finally possible to assess m. Figure 2.5 a) illustrates a graph used for obtaining m by the method of Peykov [39]. In contrast figure 2.5 b) shows the dependence of m of the flow stress σ_f as suggested from Maier *et al.* [40]. The two stages a and b arbitrarily set by Peykov correlate to two points on the graph from Maier *et al.*

It must be noted that a further assumption has to be made. Since the stiffness is just known for the point of load relieve, h_s was supposed to be constant over the whole dwell segment. High creep depths in the following np and ufg Au nanoindentation tests arrange for a minimum error and therefore this effect should be negligible. The same holds true for thermal drift, which is corrected anyway for every indent.

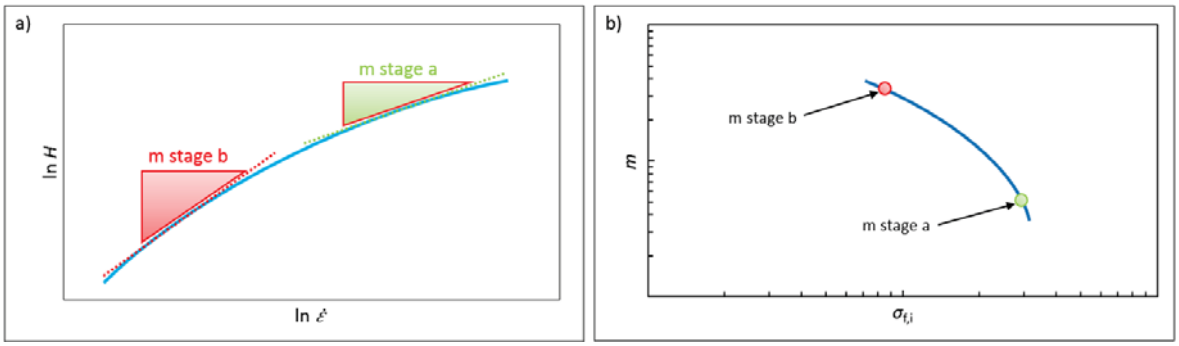

Figure 2.5 Plots for the determination of m. a) Obtaining m through regression lines. b) Double-logarithmic diagram for obtaining m in dependence of the flow stress of the material.

2.5.4. Activation volume

Similar to the strain-rate sensitivity, the activation Volume V^* can be used to describe the deformation dynamics in a material. Beside m, V^* is furthermore including the hardness, constraint factor C^* and temperature at which the experiments take place. Based on the fundamental thermodynamic relation for the Gibbs free energy the activation

volume at a constant temperature is defined as [42]

$$V^* = -\left(\frac{\partial \Delta G}{\partial \tau}\right)_T, \tag{2.19}$$

with ΔG is the Gibbs free energy and τ is the applied shear stress. For thermally activated deformation mechanisms an exponential equation is used to describe the resulting strain-rate [43]:

$$\dot{\gamma} = \dot{\gamma}_0 \cdot exp\left(-\frac{\Delta G(\tau)}{k_B \cdot T}\right). \tag{2.20}$$

$\dot{\gamma}_0$ contains several structural parameters for obstacles in the material and is considered to be independent of τ, k_B is the Boltzmann constant. Solving the equation for ΔG leads to

$$\Delta G = -k_B \cdot T \cdot ln(\dot{\gamma}) + k_B \cdot T \cdot ln(\dot{\gamma}_0). \tag{2.21}$$

Following equation (2.19) and by using relation (2.20), V^* results in

$$V^* = k_B \cdot T \cdot \frac{\partial ln(\dot{\gamma})}{\partial \tau}. \tag{2.22}$$

Taking into account the von Mises yield criterion

$$\tau = \frac{\sigma}{\sqrt{3}} \qquad \& \qquad \dot{\gamma} = \dot{\varepsilon} \cdot \sqrt{3} \tag{2.23}$$

and by rewriting the differential $d\tau$

$$y = ln(\tau),\ \frac{dy}{d\tau} = \frac{1}{\tau} \Rightarrow dy = \frac{1}{\tau} \cdot d\tau = d(ln(\tau)) \Rightarrow d\tau = \tau \cdot d(ln(\tau)) \tag{2.24}$$

the activation volume can be written as:

$$V^* = \sqrt{3} \cdot k_B \cdot T \cdot \frac{1}{\sigma} \cdot \frac{\partial ln(\dot{\varepsilon})}{\partial ln(\sigma)}. \tag{2.25}$$

Hardness and yield strength are linked by the constraint factor C^*

$$H = C^* \cdot \sigma, \tag{2.26}$$

and furthermore the strain-rate sensitivity was defined in equation (2.16). Hence, V^* finally ends up in

$$V^* = \sqrt{3} \cdot C^* \cdot k_B \cdot T \cdot \frac{1}{m \cdot H}. \tag{2.27}$$

Commonly V^*, is divided by the volume of a unit cell given in b^3 where b is the Burgers vector of the used material. High values of V^* (around 1000 b^3) are often related to cutting of forest dislocations and observed in coarse grained samples [44]. With decreasing grain size fcc materials such as Cu, Al or Ni show a different behavior, featured by an increase of m and decrease of V^* down to a few b^3, confirmed by several recent studies attributed to boundary /dislocation interactions [34, 37, 45]. Controversial results were published concerning the temperature dependence of V^*, where a decrease [43, 46] or increase [40, 47] was observed for ufg fcc materials at elevated temperatures. Coarse grained counterparts are supposed to have higher activation volumes at higher temperatures [43].

2.5.5. Activation energy

Last but not least the activation energy Q_a can make allowance for the emerging deformation mechanism and can be obtained from

$$\frac{H}{E} = G' \cdot e^{\frac{Q_a}{R \cdot T}} \tag{2.28}$$

with R as universal gas constant and G' as a material dependent constant. A graphical analysis of a logarithmic diagram allows to obtain Q_a when multiplying the slope by R.

3. Experimental

3.1. Powder investigations

Gold as well as iron powders, both with a purity higher than 99.9 % and particle sizes between 5 - 10 μm, were used. In order to guarantee a homogenous consolidation during the severe plastic deformation process the powders were investigated in a scanning electron microscope (LEO SEM 1525) to ensure that their properties are in accordance with the specification. It was determined that the Au as well as the Fe particles have a spherical form and the declared sizes, as depicted in figure 3.1. Consequently, this leads to the result that the powders are well suited for HPT sample production.

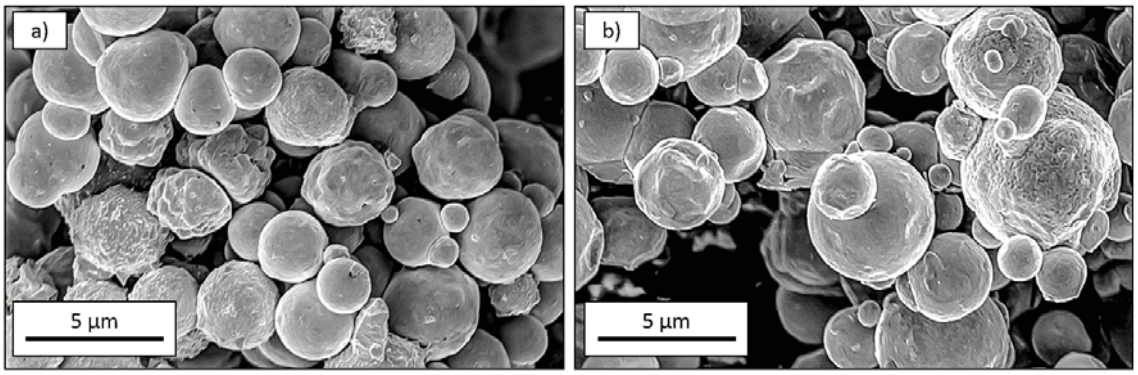

Figure 3.1 SEM images showing the used a) gold and b) iron powder for sample fabrication.

3.2. Powder mixing

Beside bulk gold, also Au/Fe samples were prepared in order to produce a nanoporous foam through a selective etching process. With the objective to obtain a porosity of about 50 %, the significant different specific densities of Au ($19.32\ \mathrm{g \cdot cm^{-3}}$) and Fe ($7.87\ \mathrm{g \cdot cm^{-3}}$) had to be considered. For this reason a 50/50 mixture in reference to percent of volume was prepared which leads to a ratio of 41 at.-% Au and 59 at.-% Fe ($Au_{41}Fe_{59}$). Since the densities of those elements show a wide difference a multi-axial mixing method was applied.

3.3. High Pressure Torsion

Several disk shaped samples of Au and the premixed $Au_{41}Fe_{59}$ compound were prepared by performing the HPT process which is accurately described in chapter 2.2.1. It was aimed to produce samples with a minimum height of 1 mm. Hence anvils with a depth of 0.5 mm were fabricated. So as to avoid a waste of the expensive gold powder a copper ring (8 mm in diameter, 4 mm height) was glued on the lower anvil. The powder was filled in by a spatula and pre-pressed by hand, an image of the setup is shown in figure 3.2 a) and b). Afterwards the powder was deformed with the HPT tool where a pressure of 4.0 GPa was applied for 3 seconds to form a blank. The machine was unloaded and the deformed copper ring separated with a nipper from the compacted gold. Subsequently the preformed blanks were deformed in a second step in the HPT tool through 200 revolutions with a speed of 0.6 turns per minute under a constant pressure of 7.8 GPa. To guarantee a constant temperature during the process, an air cooling system was installed. Ultimately, eight Au samples, three with a thickness of 0.4 mm (Au 1 - 3) and five with 1 mm (Au 4 - 8), were produced. On the other hand six AuFe specimens where fabricated, each with a disk thickness of about 1 mm.

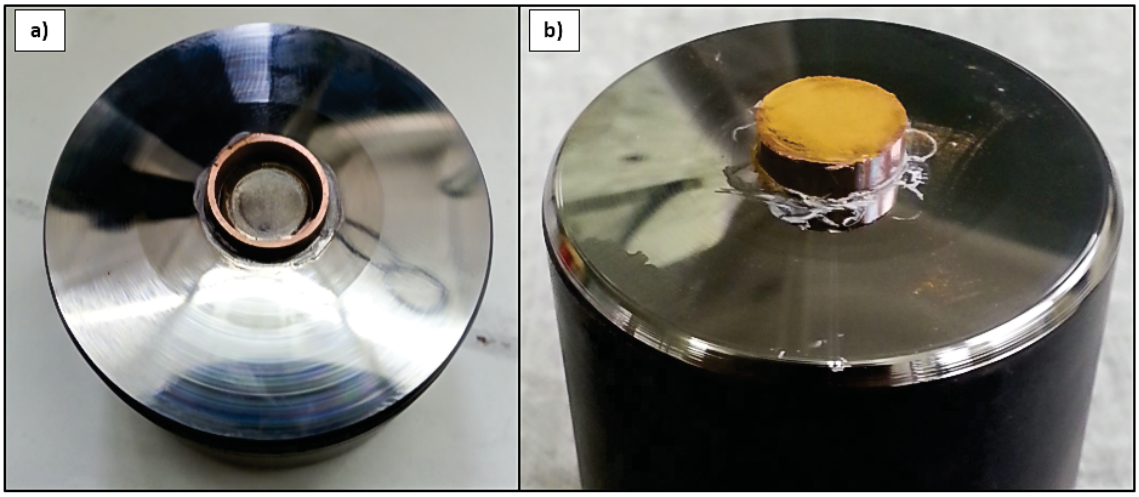

Figure 3.2 Images showing a) the glued Cu ring on the anvil and b) pre-pressed gold powder in the ring ready for HPT process.

3.4. Preparation of microsections

The investigation of the microstructure and likewise the measurement of the hardness requires a smooth surface. Furthermore, subsequent nanoindentation should be carried out in a preferably homogenous zone which is considered to be located right in the middle of the disk height. For this reason the samples were ground down from a starting thickness of 0.8 - 1.0 mm to 0.4 - 0.5 mm and polished by diamond suspensions (9 μm, 3 μm, 1 μm). Subsequently, a 0.05 μm colloidal silica oxide suspension was used to ensure an adequate surface quality for the upcoming experiments. No continuing treatment of the compound samples was necessary but investigations of the Au specimens with the LM revealed that the surface is still too rough and strewn with tiny scratches. Those prohibit a qualitative examination of the microstructure via BSD mode or EBSD in an SEM. Therefore an appropriate method for electrolytic polishing of the ufg Au had to be found. The best results were achieved by using concentrated hydrochloric acid (32 vol.-%) with a voltage of 5 V for about 15 s. However, as Au is a very soft material a wavy surface cannot be avoided nonetheless, the quality was found sufficient for subsequent EBSD scans and nanonindentation experiments.

3.5. Microhardness

In order to proof the success of the HPT procedure microhardness experiments were conducted with a BUEHLER Micromet 5100 after the polishing process. Au samples were proofed with a weight of 200 gf, AuFe samples with 500 gf. Hardness profiles were generated over the whole cross-section of the specimens with a distance of 500 μm between the indents, as depicted in figure 3.3. Au samples were tested again after 30 days in order to assess whether any effects of recrystallization appear at a storage temperature of about 22 °C as previously reported by Matsunaga *et al.* [17]. Furthermore, hardness measurements were conducted after annealing as well, initially to study the thermal stability.

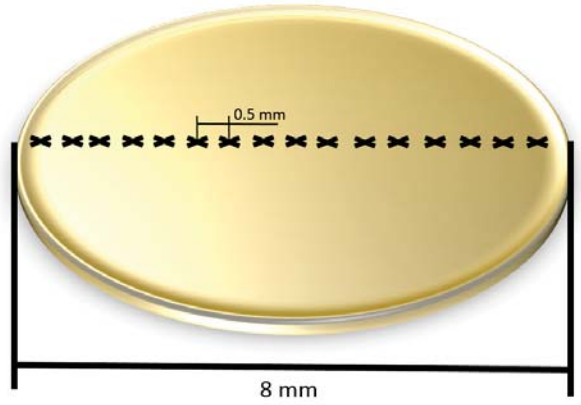

Figure 3.3 Illustration of indent positions of microhardness measurements.

3.6. Microstructural evolution of Au

In order to appraise if any changes of the fine grained microstructure will occur during HT nanoindentation, the recrystallization temperature $T_{R_{xx}}$ has to be identified. For this reason an ultra-fine grained Au sample was characterized by EBSD scans in an SEM at room temperature as well as after subsequent heat treatments with a dwell time of 1 h

at elevated temperatures of 100 °C, 150 °C, 200 °C, 250 °C, 300 °C, 350 °C, 400 °C and 450 °C in a vacuum oven (SERIES XRETORT, Xerion Advanced Heating Ofentechnik GmbH, Germany), which guarantees a maximum pressure of 5 - 10 mbar during the annealing. The heating-up rate was set with 10 °C per minute. By determining the average grain size after each heating, a temperature limit for annealing was set. Since the high current used for EBSD investigations lowers the specimen's surface quality by causing carbon contamination, scans were not performed on the same spot but within a region of 50 μm x 50 μm. Last but not least, energy dispersive X-Ray spectroscopy (EDX) was used to investigate local compositions of the samples. Subsequent measurements of hardness profiles were conducted in order to the hardness in contrast to samples tested shortly after HPT-processing.

3.7. Foam processing and characterization

AuFe samples are expected to contain supersaturated phases [48] which should be avoided since the mechanical behavior of a pure gold foam is the matter of interest. For the purpose of preventing this supersaturated state the AuFe disks were annealed at 300 °C for 1 h. In order to produce a nanoporous foam, the iron has to be selectively removed by etching. Since the specimens will be embedded in high temperature cement for nanoindentation, the samples shall not be porous over their whole height to avoid capillary percolation. A dealloying depth between 50 μm and 150 μm should be achieved by using a low concentrated hydrochloric acid (5 ml of a 32 % HCl on 95 ml distillate water) at 55 °C for 24 hours, following result experimentally determined by Kreuzeder [49]. The acid was heated up in a glass container and after achieving the desired temperature the samples were put into the HCl. A magnetic stirrer was arranged for a fair agitation in the basin to achieve a consistent etching process. Subsequent argon ion milling (E-3500 Ion Milling, Hitachi High Technologies Pte Ltd, Japan) was conducted to confirm the dealloying depth. The parameters were set with 6 kV accelerating voltage

and 4 kV discharge voltage for 150 min, whereby a penetration depth of 350 μm could be reached. As the porosity could not be investigated with an optical microscope due to the nano-scale structure, an ensuing SEM examination had to be performed. By this opportunity, EDX spectroscopy was done as well in order address whether there is still supersaturated iron remaining in the gold foam. Additionally, EBSD was performed to obtain the grain structure of ligaments.

Due to a major influence of porosity in regard to the mechanical properties of the material it was attempted to estimate this value by transforming SEM images of the foam to binary images. By metering the count of black and white pixels a first appraisal on the porosity was achieved (see chapter 3.9.1 for details).

3.8. Nanoindentation

3.8.1. Equipment

All nanoindentation experiments were conducted on a Micro Materials Nano Test facility (figure 3.4 a)) combined with the "Nano Test Three Platform" software provided from the manufacturer [50]. Figure 3.4 b) shows the hardware concept. The force measurement is based on a electromagnetic system (permanent magnet / coil) and provides a resolution of 30 nN, whereat forces up to 500 mN can be reached. On the other hand a capacitive system is responsible for displacement measurement with noticeable 10 pm and maximum achievable depths of 50 μm [51]. Additionally, a damping plate is installed in order to reduce the signal's noise. Furthermore, this nanoindenter is capable of performing high temperature (HT) experiments up to 700 °C. For HT indentation it is necessary to replace common superglue, which is used for room temperature experiments, by high temperature cement. In the instant report sodium silicate based "Omegabond 700" (Omega Engineering, Inc) was used. The manufacturer guarantees

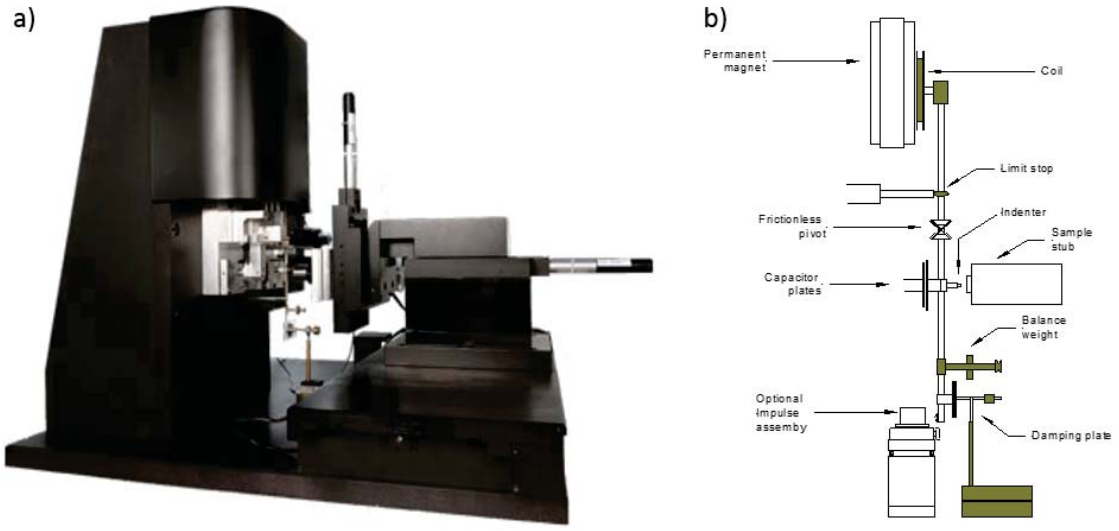

Figure 3.4 a) Used Micro Materials Nano Test facility and b) used measurement concept [50].

accurate mechanical bonding to metals as well as appropriate thermal properties up to 827 °C [52]. The ceramic powder has to be mixed with water (weight ratio 80 : 20). After placing the specimen and the paste on the sample holder, also called hot stage, a subsequent drying time of 18 - 24 h has to be adhered. Supplementary, a reference sample was placed close to the specimen and connected with a thermocouple (figure 3.5 a)). This approach was aimed to control the temperature at the sample's surface by reason to exclude errors, since the thermocouples of the indenter and hot stage, which are used for the adjustment, not necessarily have the same temperature as the surface. Thus, it was assessed that slightly higher temperatures have to be set in order to reach the desired value at the measurement position. Special HT-indenter modules with heat shields and water cooling installments (for temperatures higher 400 °C) are used as depicted in figure 3.5 b). Additionally, the cabinet provides the opportunity to purge it with protective gas. For experiments of the present reports at HT a reductive mixture of argon and hydrogen was used so as to minimize the risk of oxidation due to remaining impurities in the samples. A Berkovich diamond indenter was mounted at RT, on the other hand a cBN Berkovich indenter was used for HT experiments. By conducting tests on fused silica both area function and frame compliance were determined before

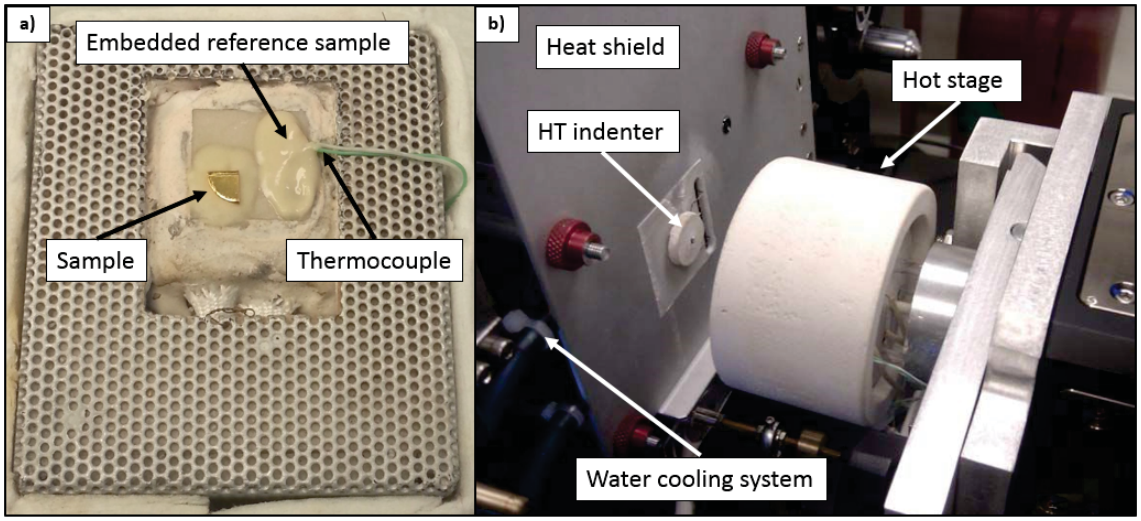

Figure 3.5 a) Sample placement on the hot stage and b) experimental setup prior HT indentation [53].

starting experiments on gold samples. The area function was measured again after the experiments in order to assess changes of the tip geometry during indentation.

3.8.2. Experimental schedule

Experiments with various parameters were planned in order to obtain the Young's modulus, hardness and strain-rate sensitivity of the material, where at least 10 indents were made for every condition. Thereby, displacement controlled (DC) runs with proportional load ramps (equivalent to a constant strain-rate) with 5 s dwell time were performed to obtain E, H and m from constant strain-rate measurements. On the other hand, load controlled (LC) experiments were conducted with higher dwell times (30 s and 200 s) in order to gain values for the strain-rate sensitivity. All specific parameters are displayed in table 3.1 for ufg Au and table 3.2 for np Au, respectively. F_{max} for ufg Au nanoindentation at 300 °C had to be decreased to 10 mN, as pile-ups appeared for high indentation depths. Supplementary LC measurements were conducted prior and after experiments in order to check changes of the material or setup respectively, occurring predominantly after indenting at elevated temperatures.

Table 3.1 Experimental schedule for ufg Au.

Type	LC	LC	DC	DC	DC
F_{max}	50 mN 10 mN	50 mN 10 mN	-	-	-
h_{max}	-	-	1000 nm	1000 nm	1000 nm
Loading rate	5 mN/s	5 mN/s	-	-	-
Strain rate	-	-	0.1	0.05	0.025
Unloading rate	10 mN/s	10 mN/s	10 mN/s	10 mN/s	10 mN/s
Dwell time	30 s	200 s	5 s	5 s	5 s
Obtained values	E, H, m	m	E, H	E, H	E, H

Table 3.2 Experimental schedule for np Au.

Type	LC	LC	DC	DC	DC
F_{max}	10	10	-	-	-
h_{max}	-	-	2000 nm	2000 nm	2000 nm
Loading rate	1 mN/s	1 mN/s	-	-	-
Strain rate	-	-	0.1	0.05	0.025
Unloading rate	2 mN/s	2 mN/s	10 mN/s	10 mN/s	10 mN/s
Dwell time	30 s	200 s	5 s	5 s	5 s
Obtained values	E, H, m	m	E, H	E, H	E, H

3.8.3. Data analysis

Numerous indents are needed to obtain distinctive and statistical verified mechanical values. Since the experimental schedule at every temperature comprises 70 indents a manual analysis for H, E and especially m is hard going. The provided "Nano Test Platform Three" software is able to output values for H and the reduced modulus E_r though, however, there is no possibility to obtain E and in particular m as the procedure described in section 2.5 is not fully implemented. Therefore, a VBA based software was developed in order to automatize the analysis and to reduce the calculating time from several hours to a few minutes. The software includes a graphical user interface (figure 3.6) which allows to define various experimental parameters plus sample and indenter properties. Finally, values including H, E, m and V^* as well as several graphical plots are displayed in MS Excel® worksheets. Main fragments of the VBA code are provided in appendix A.

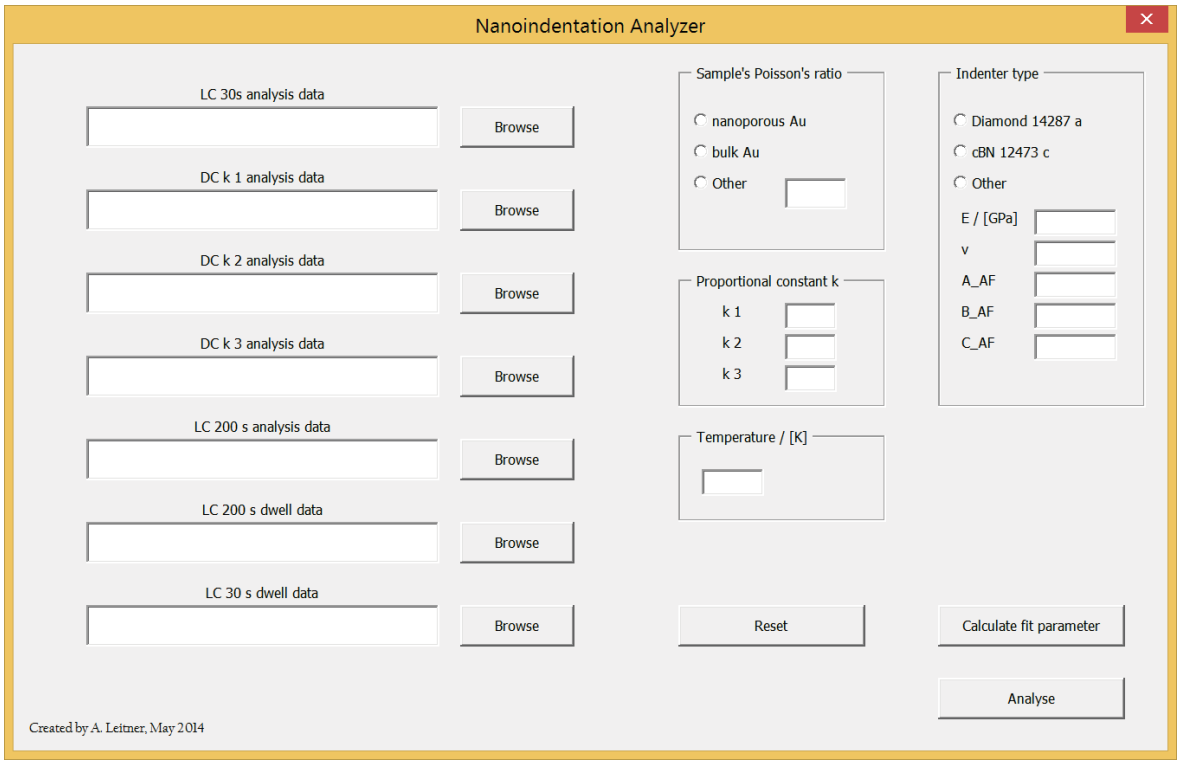

Figure 3.6 Illustration of the GUI of the developed analyzing software.

3.9. FIB cross-sections

In order to study the extent of densification for np Au samples beneath the indenter tip and to examine possible changes of the microstructure of the investigated gold samples, cross-sections were prepared with an FIB LEO-1540XB. Curtaining effects could be reduced by depositing a thin layer of platinum or tungsten respectively on the sample's surface. Material was removed until the deepest point of the indent was reached. Sections of the indents measure about 10 μm depth and 20 μm width.

3.9.1. Porosity maps of np Au indents

It is well known, that compression of porous materials leads to compaction. Since the stress field beneath an indenter tip is not homogenous, the occurring deformation is not self-evident either. Therefore a method was introduced to describe the porosity or density, respectively, of the foam as a function of the position. For this purpose SEM images of the cross-sections were edited in order to balance contrast effects caused by the SEM detector. Thus, the contrast of the cut ligaments can be intensified and hence be distinguished from material, which is situated behind the sectional plane. In the next step, ImageJ [54] is used to set a threshold value at the gray-scale to create a binary black / white image. This procedure is demonstrated for the surface of nanoporous gold in figure 3.7 a)-c). The ratio of black to white pixels in a certain frame is equivalent to the porosity.

A porosity map can be created by scanning an image with a set frame and step size. 500 nm x 500 nm was considered to be an appropriate size to avoid local, unreal variations on the one hand but is still giving a sufficient local resolution on the other hand (figure 3.8 a)). This corresponds to about 40 px x 40 px, therefore the used step size of 5 px leads to a maximum change of porosity of 12.5 % between two adjacent points. The porosity value is always ascribed to the center of the square, consequently the information of

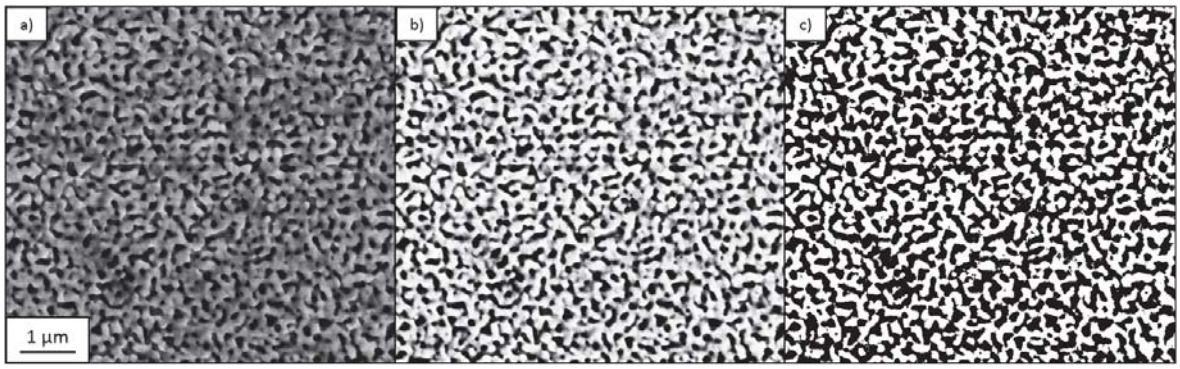

Figure 3.7 a) SEM micrograph of np Au, b) image after first editing and c) binary image generated with ImageJ.

250 nm width at the edge is lost, illustrated in in figure 3.8 b). The results of a scan are written in an array corresponding to the coordinates of the position of the square. At near-surface areas this zone will be extrapolated by taking the mean of surrounding valid points. In order to proof this method two markers were added in an image which should be clearly visible in the density map (figure 3.8 b)). A colormap was created and overlaid with the binary image (figure 3.9). The result confirms that variations of the porosity, in this case the markers, are detected properly, therefore this tool can be used to describe the densification of np Au during nanoindentation.

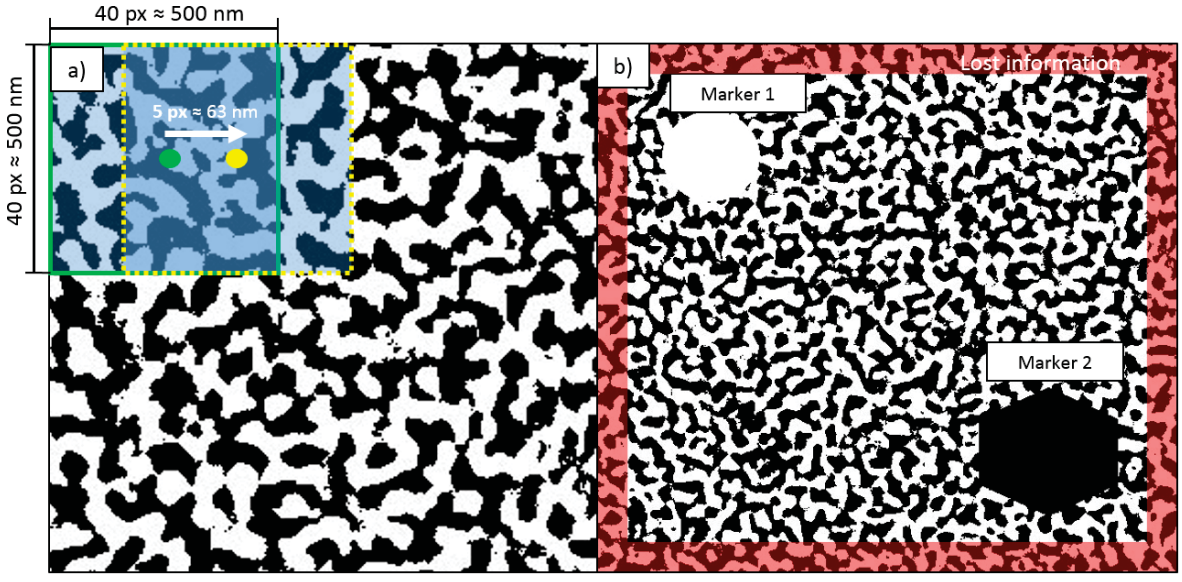

Figure 3.8 a) Magnified depiction of the scanning procedure and b) exemplary image used to proof the method and the zone of lost information.

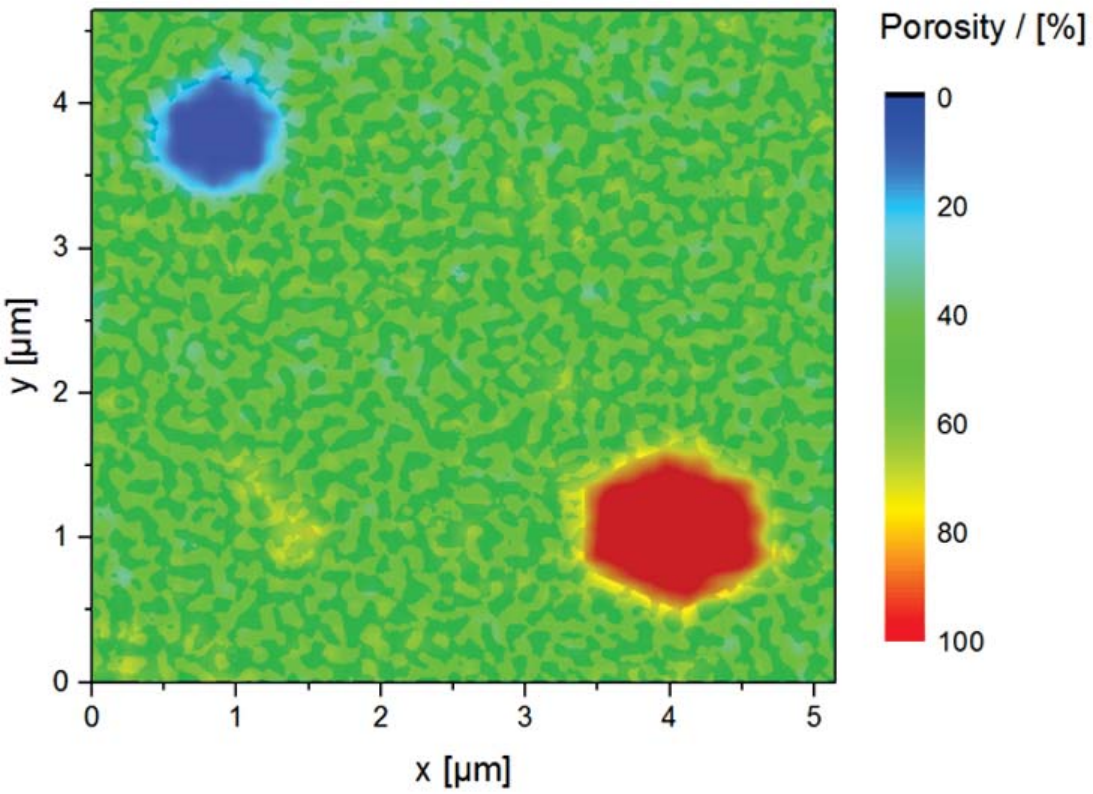

Figure 3.9 Resulting colormap with overlaid binary image.

4. Results

4.1. HPT processing

During HPT processing torque and time data were recorded. When a constant torque level is reached one can assume that that no further hardening in the material occurs and the microstructure has reached a steady state level. In figure 4.1 two representative torque / time plots are depicted for Au and AuFe samples, respectively. As expected, the compound samples reach a higher torque during processing as the amount of iron increases the sample's hardness significantly. As supposed both curves gain a steady state torque level. The oscillation of the graph might rather derive from an out-of-roundness of the HPT-tool and should not be ascribed to microstructural changes.

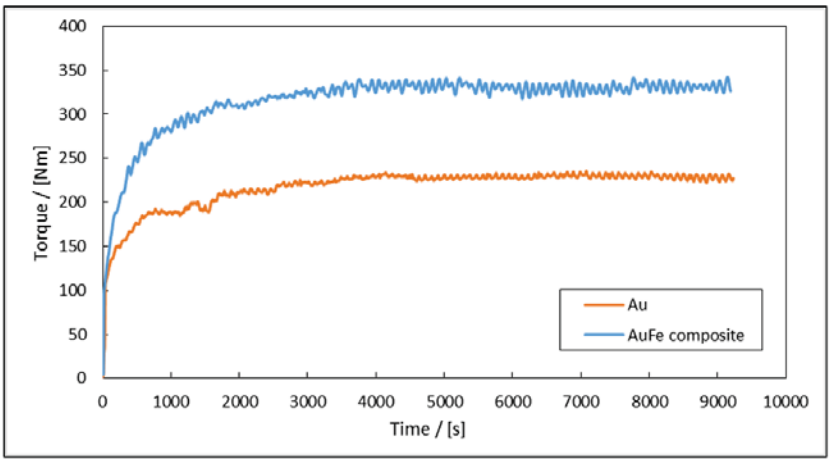

Figure 4.1 Diagram displaying torque / time graphs of Au and AuFe samples during HPT processing corresponding to the first 90 revolutions.

4.2. Macroscopic appearance after HPT-processing

After the preparation of microsections, as described in 3.4, the structure of the samples was at first assessed with the light microscope (Olympus BX51, Olympus Corporation, Japan).

4.2.1. LM investigations of ufg Au

The gold samples appear homogenous although a few irregularities in thickness and inclusions are present after polishing, as demonstrated in figure 4.2 a). Moreover, no cracks could be detected in the microsections. Figure 4.2 b) shows the surface in detail after the electrolytic polishing, which quality is adequate for EBSD scans.

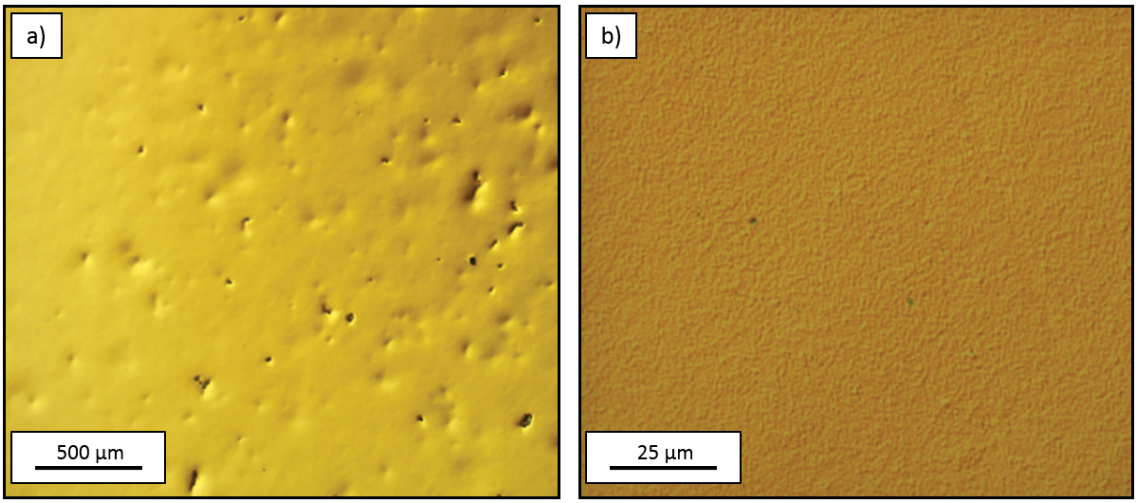

Figure 4.2 Light microscope images showing a) an overview and b) a detailed picture of the Au sample's surface after HPT and subsequent polishing.

4.2.2. LM investigations of AuFe

The AuFe compound samples show a couple of cracks at their surfaces (figure 4.3 a)), most likely they are initiated through high stress levels which occur during the HPT procedure. Furthermore, it is remarkable that there are different zones in the cross-section. In the center of the disk Au and Fe can easily be distinguished which is not the case in peripheral zones. One of the AuFe composite samples even shows a sharp transition line between those areas, illustrated in figure 4.3 b), which could not be observed for the other AuFe samples.

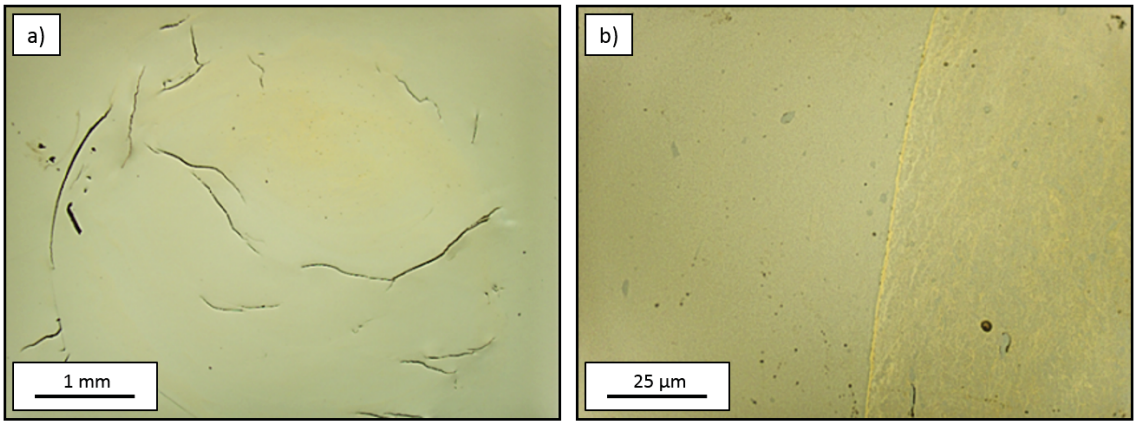

Figure 4.3 Light microscope images depicting a) cracks in the microsection and b) a transition line between homogenous and heterogeneous areas.

4.3. Microhardness

4.3.1. Microhardness of ufg Au

The Au disks show very different hardness profiles. Some of them manifest the expected curve for HPT deformed materials, such as Au 2 (figure 4.4 a)) with a high hardness at the outer regime and a hardness drop towards the sample center. On the other hand specimens, by way of example Au 1 or Au 3 show lack of an increase in hardness at the

edge of samples, which could be ascribed to an insufficient deformation. All the hardness profiles are depicted in figure 4.4. However, the hardness value in peripheral zones is extraordinary high opposed to the hardness of common bulk gold (around 45 HV [17]) as well as to HPT deformed bulk gold where a hardness of about 90 HV is reported [19]. By reason that gold is a soft metal and a quasi-constrained HPT-mode was performed, excessive material flows out between the anvils. It was suspected that the different hardness profiles originate from an insufficient deformation when anvils start to grind against each other after a certain time instead of shearing the Au. In order not to waste expensive material those specimens were re-processed in a subsequent HPT step where a pressure of 7.8 GPa was applied for 50 revolutions at a speed of 0.6 turns per minute and where one of the anvils was exchanged for a shallower one with a depth of 0.2 mm instead of 0.5 mm. The hardness profile is shown in figure 4.5 and leads to the result that the hardness was hardly influenced by this procedure.

Matsunaga *et al.* [17] report recrystallization of HPT - gold at room temperature when the storage duration exceeds a time of 30 days. In contrast to this report they deformed bulk gold with a purity of 99.999 % instead of gold powder with a purity of 99.96 %. To exclude the incidence of such effects, Au samples were tested again after 30 days. As can be seen in figure 4.6, no significant change of the disks hardness was noticed.

After the heat treatment the hardness profiles hardly changed for which reason no major difference of microstructure is suspected. Since no steady state hardness level could be reached, further microstructural investigations such as EBSD and EDX are required.

4.3.2. Microhardness of AuFe

Just as for the Au samples, the microhardness of the AuFe disks were investigated too, illustrated in figure 4.7. In homogenous regions 3 mm in radial direction away from the center, the hardness level seems to be almost constant with a value of 390 HV 0.5.

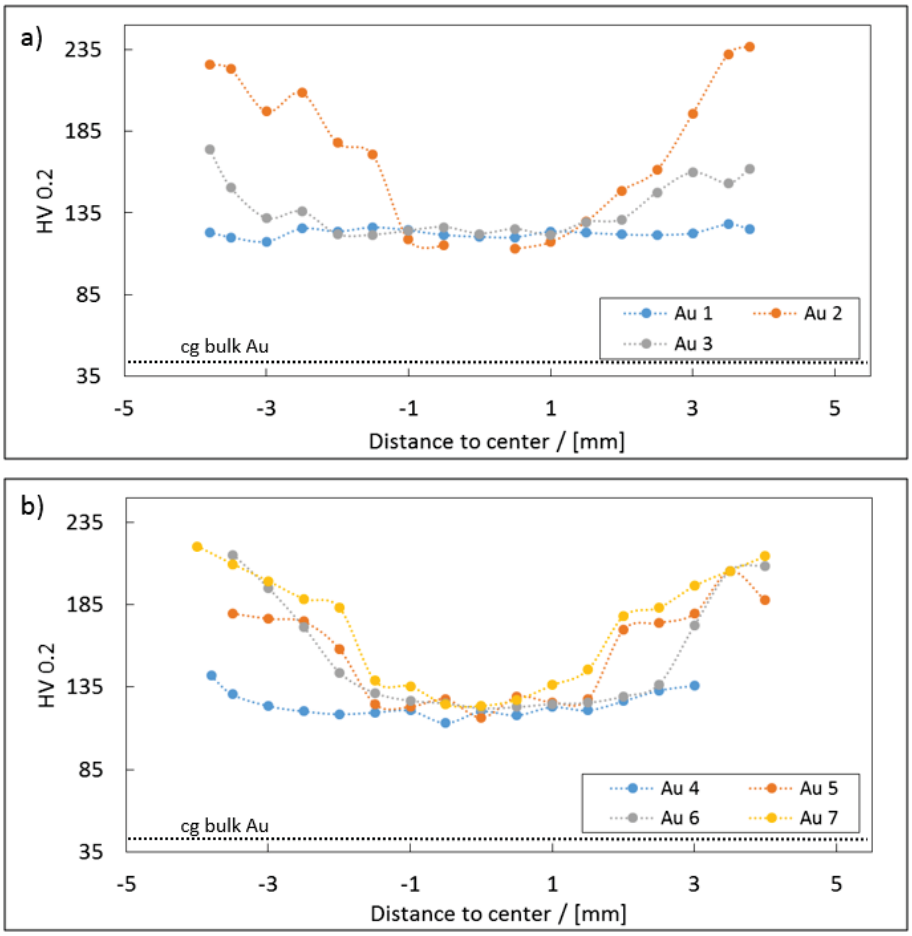

Figure 4.4 Hardness profiles of a) 0.4 mm thick Au samples and b) 1 mm thick Au samples after HPT processing.

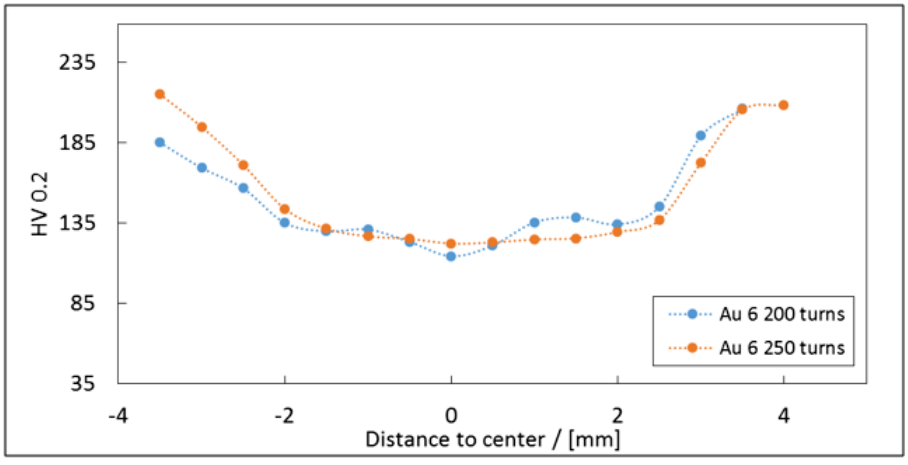

Figure 4.5 Hardness profiles of a gold sample before and after an additional HPT step.

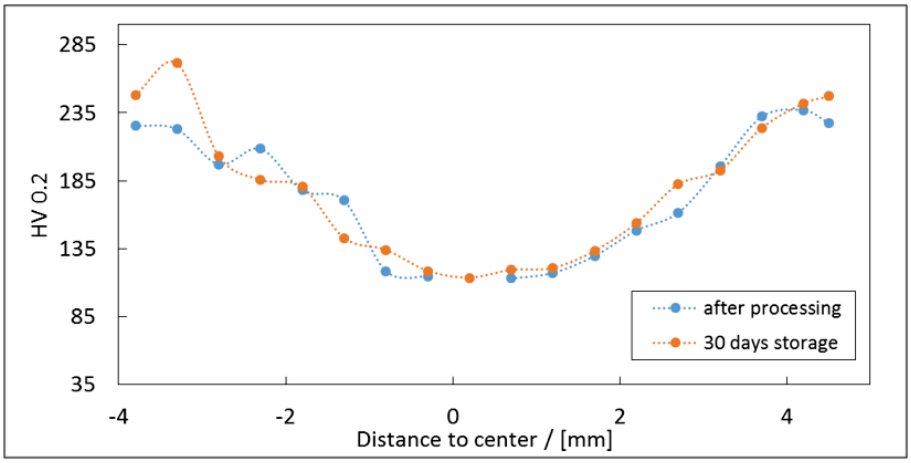

Figure 4.6 Hardness profile of a gold sample directly after HPT processing and after 30 days of storage at room temperature.

Overall, the hardness profiles scatter over cross-section, which might result from cracks in the sample which could decisively influence the mechanical behavior.

After annealing a decisive change of the hardness profile can be observed, particularly in peripheral zones as depicted in figure 4.8 for sample AuFe 2. Unexpectedly, hardness increased in those areas around 90 HV when the heat treatment of 300 °C for one 1 h in a vacuum oven was completed. At the center an opposite behavior was observed which becomes noticeable through a decrease of hardness of approximately 90 HV. However, just as for the Au samples, a homogenous zone for nanoindentation had to be found as well to produce comparable data. It was decided to choose areas where light microscope images show a homogenous microstructure which goes along with steady hardness levels of an average hardness of 515 HV $\pm$ 23 HV prior etching. These areas are suspected to show the most reliable properties.

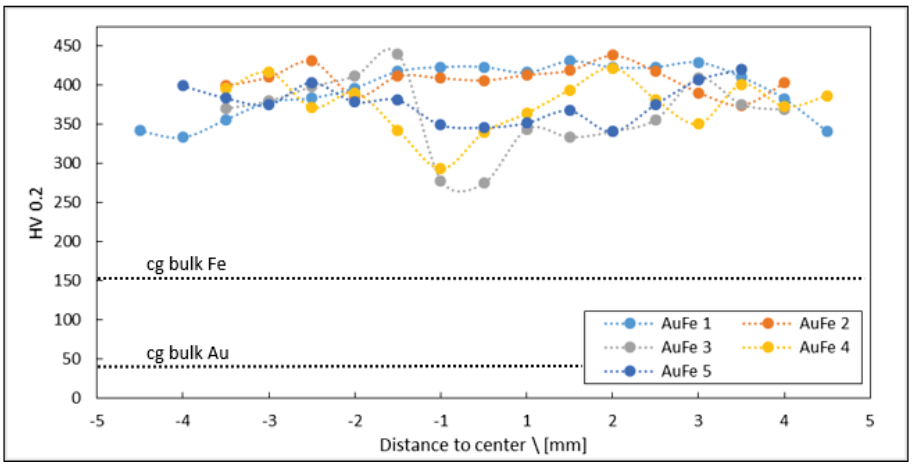

Figure 4.7 Hardness profiles of the AuFe compound samples instantly after HPT - fabrication.

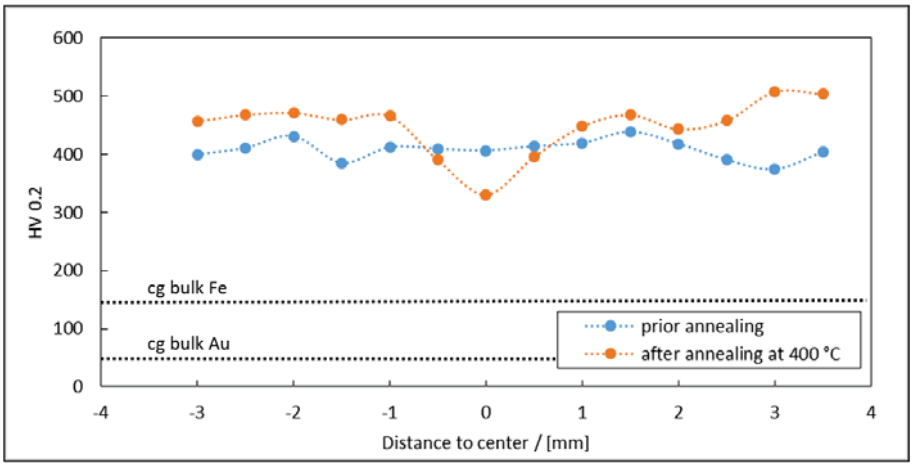

Figure 4.8 Hardness profiles of a AuFe compound sample illustrating a change of hardness after annealing.

4.4. Microstructural evolution

4.4.1. Microstructural evolution of ufg Au

Back scattered electron detection (BSD) and EBSD scans were performed to investigate the microstructure of ultra-fine grained gold. Through optimal preparation of the sample's surface by electrolytic polishing EBSD scans with high resolution can be provided. BSE images as well as EBSD scans confirm a grain size in the magnitude of 100 nm at a radial distance of 3 mm away from the disk center, as depicted in figure 4.9 a) and b). Zones in the center of the samples were investigated alike to establish if the lower hardness in this region results from a larger grain size. Indeed grains show an average size of 250 nm in the middle of the disk, which leads to a significant lower contribution of the Hall-Petch effect in consideration of the material's hardness [8, 9].

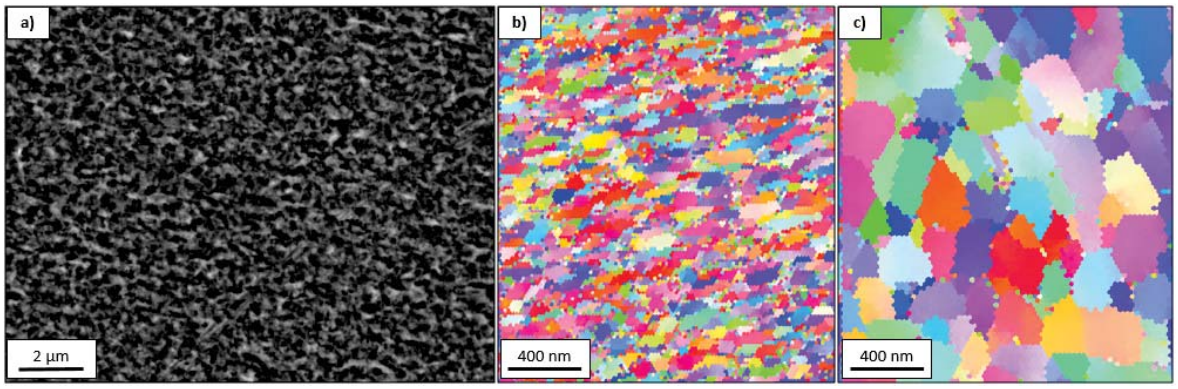

Figure 4.9 Microstructure of a fabricated gold sample a) with BSD-mode, b) EBSD mode at r = 3 mm and c) EBSD mode in the specimen's center.

As mentioned in chapter 3.6 the Au samples were encountered heat treatments with a step size of 50 °C. After each annealing procedure the microstructure was analyzed by EBSD-scans, illustrated in 4.10 a) - f). A slight increase of grain size occurs until a temperature of 400 °C. Considering the different scale of figure 4.10 f), it becomes obvious that enormous grain growth takes place when the annealing temperature reaches a value of 450 °C. Since hardness profiles of the different disks vary slightly and the

recrystallization temperature is dependent of the degree of deformation, an annealing temperature of 300 °C was determined for the residual specimens to minimize the risk of unexpected grain growth. Furthermore, an unexpected color change was noticed in peripheral zones appeared when temperature reached a level of 250 °C.

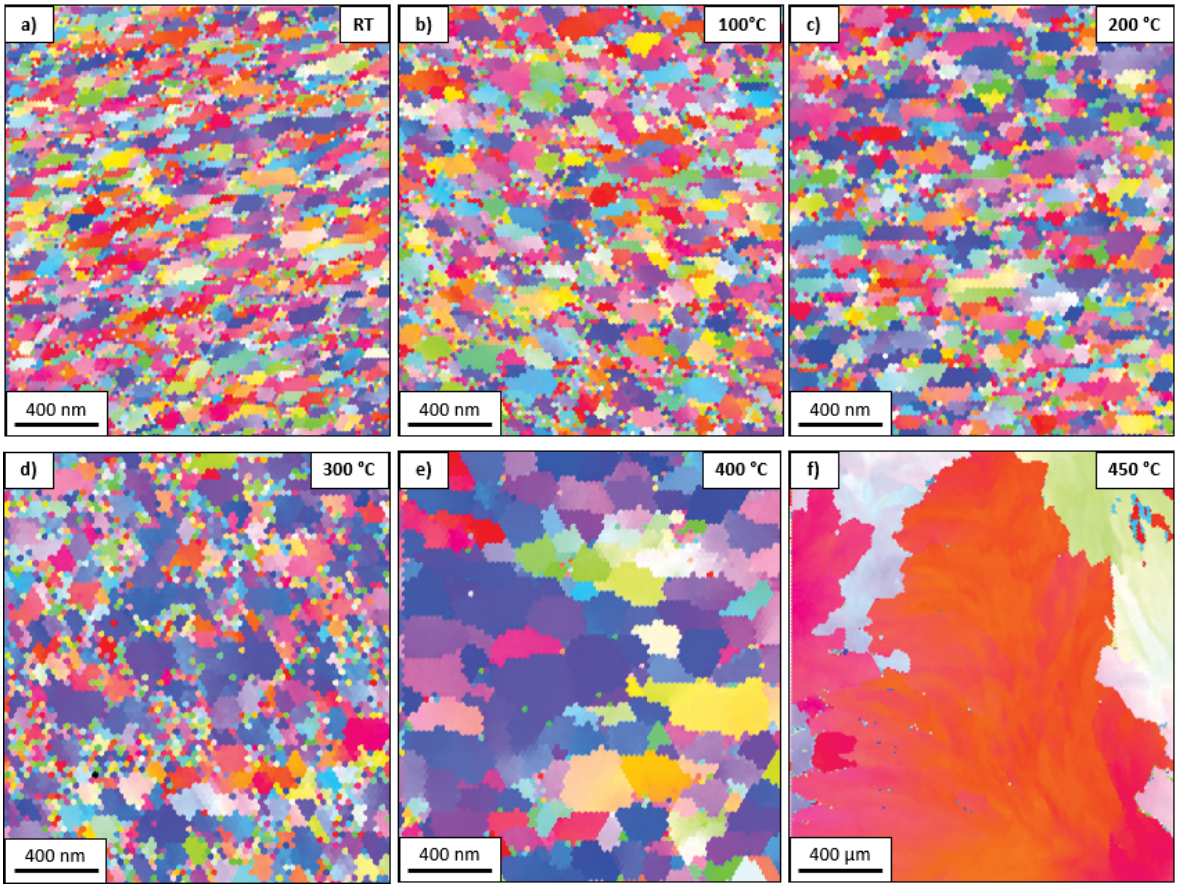

Figure 4.10 Microstructural evolution of Au illustrated by EBSD scans after annealing at various temperatures between 100 °C and between 450 °C.

4.4.2. Microstructural evolution of AuFe

SEM images, recorded in BSD mode, show two significant different zones on the sample's surface. As depicted in figure 4.11 zone 1 is supposed to be homogenous since no distinction between Au and Fe particles can be made. This area can particularly be found in peripheral zones more than 2 mm away from the specimen's center. On the

other hand, zone 2 appears mainly in the middle of the disk where Au and Fe can easily be distinguished. However, zone 2 can be found in outer regions too where these fields measure a few hundred μm^2, whereas zone 1 appears in peripheral areas only. Most transitions between those zones show sharp limits, nevertheless flowing transitions were observed as well.

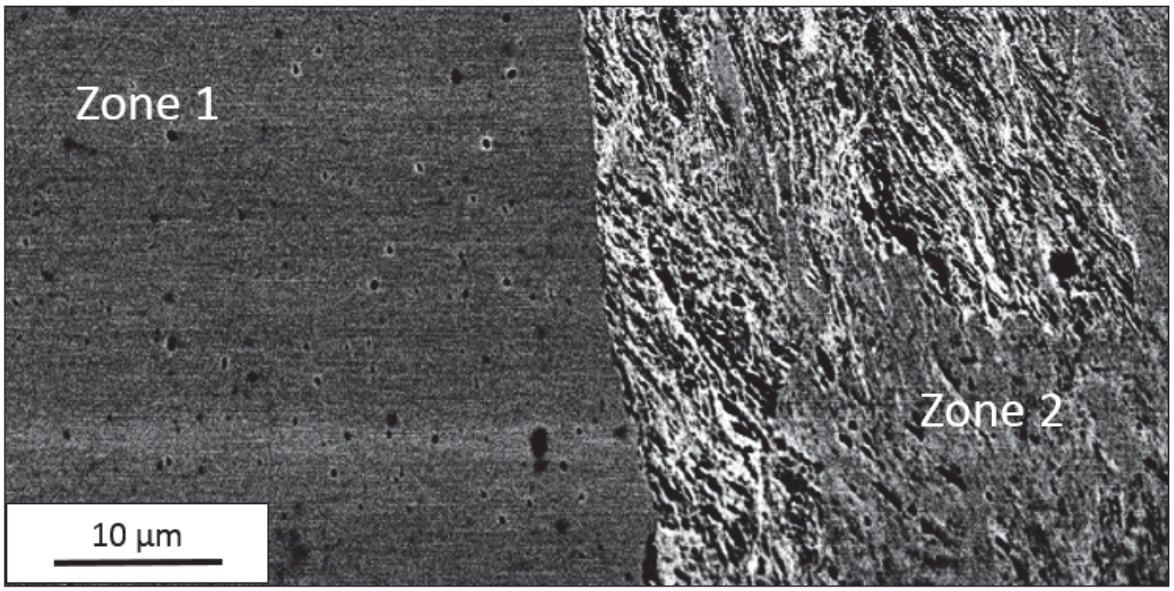

Figure 4.11 SEM micrograph in BSD mode illustrating different zones on the compound sample.

After annealing the microstructure slightly changes. In zone 1 gold and iron can be discriminated when the SEM is used in BSD mode, whereas the distribution of those grains is much finer than in zone 2. In zone 2 no changes could be recognized after the heat treatment, it still appears coarse distributed. Zone 1 shows the desired structure which lets hope for a homogenous foam with ligament sizes down to the nano-scale after the etching process.

4.5. EDX measurements

In order to examine the local composition of the HPT disks, the method of energy dispersive X-ray spectroscopy (EDX) was chosen.

4.5.1. EDX of ufg Au

The examination of the gold samples led to an interesting result, namely that in peripheral zones a significant amount of Cu is present. In regions near the edge Cu could diffuse into the sample during the HPT process, although most of the Cu ring, which was used for the pre-consolidation of the powder as mentioned in chapter 3.3, was cut from the blank. The Cu concentration profile shows a similar trend compared to the microhardness (figure 4.12 a)) which leads to the assumption that pure gold has rather reached the steady state level in the center of the specimens. Considering this fact, it was decided that nanoindentation experiments should be carried out in areas close to the center to guarantee that results are not influenced from the remaining copper. Beside Au and Cu no further elements could be detected by EDX measurements. Additionally EBSD scans along the radial direction revealed a constantly increasing average grain size toward the center (figure 4.12 a)).

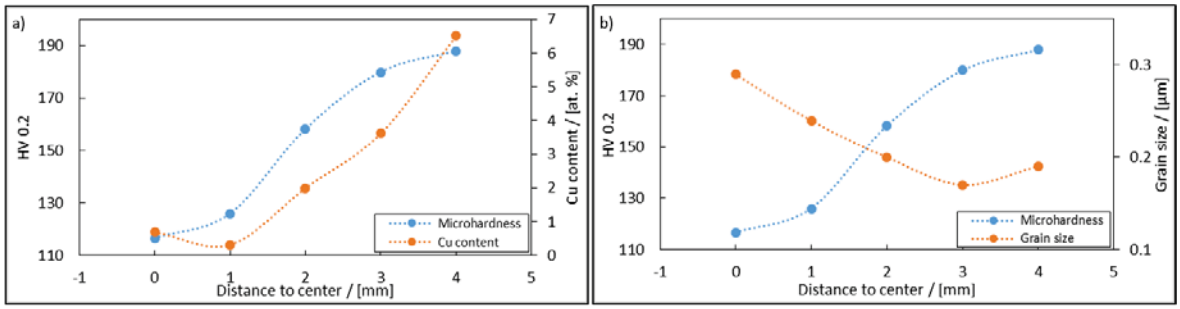

Figure 4.12 a) Comparison of Cu content and microhardness profile of an ufg Au sample with respect to the radial distance. b) Microhardness values with the corresponding average grain size.

The color change in peripheral zones, mentioned in 4.4.1, can be attributed to the formation of CuO respectively CuO_2, since around 27 at.-% oxygen and 22 at.-% copper could be detected by EDX in this zones.

As a consequence of the preceding investigations it was decided to conduct nanoindentation experiments close to the center of the samples, where the influence of remaining Cu is negligible and the disks show a steady state hardness of 123 HV 0.2.

4.5.2. EDX of AuFe

Although the compound samples were produced the same way, no Cu could be found at any measured position on the disk. The powder mixture was supposed to provide a ratio of 41 at.-% Au to 59 at.-% iron. However, EDX results show a slightly different ratio of 44 : 56 which may result from mistakes during weighing or from an insufficient powder mixing process. No other elements than those mentioned above could be found.

4.6. Foam processing and characterization

First trials on etching were made with HCl with various concentrations at 55 $°C$. This temperature is necessary to have Fe sufficiently attacked by hydrochloric acid [49]. The surface of the etched AuFe samples were checked by LM every hour when 5 vol.-% HCl was used and every 5 hours when 1 vol.-% HCl was used. First changes in surface microstructure were detected after 34 h for the low concentrated HCl and after 24 hours for the higher concentrated acid. However, subsequent ion milling of those samples showed that the dealloying depth reached the thickness of the sample, since no dense regions remained.

4.6.1. Appearance of np Au

Figures 4.13 a) - e) display the structure of the np Au at different radial positions. Close to the center, where lower strains are reached through HPT, the structure turns up nonuniform and will therefore not be used for nanoindentation experiments. The surface of the etched sample appears homogenous in peripheral zones with ligament sizes around 100 nm, as shown in figure 4.14 a) and b). A binary picture was created (figure 4.14 c)) as described in chapter 3.9.1, whereat the ratio between black and white pixels was determined to be about 1:1, leading to a porosity of approximately 50 %.

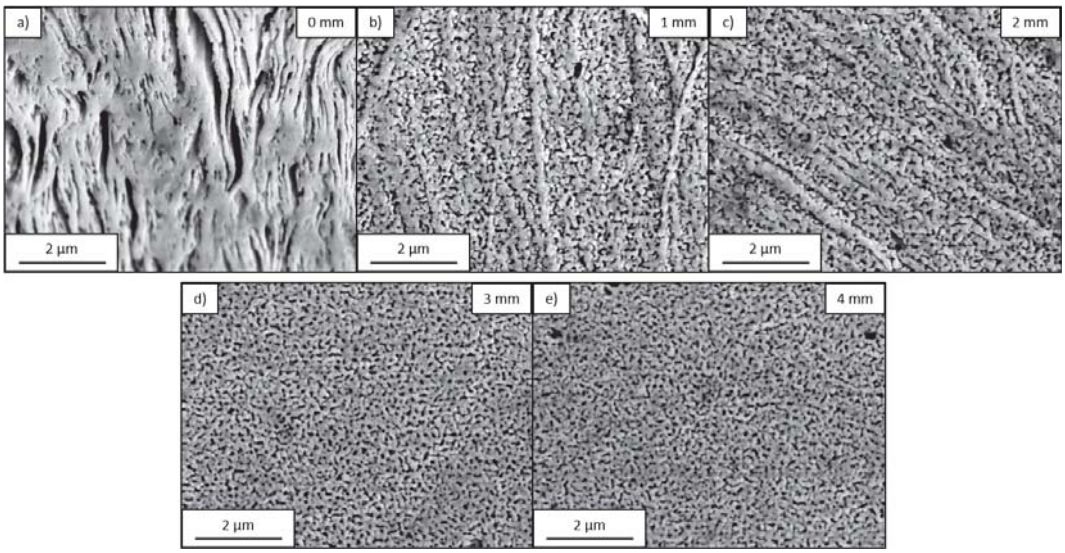

Figure 4.13 SEM micrographs of the foam at various radial positions from a) in the center to e) close to the edge.

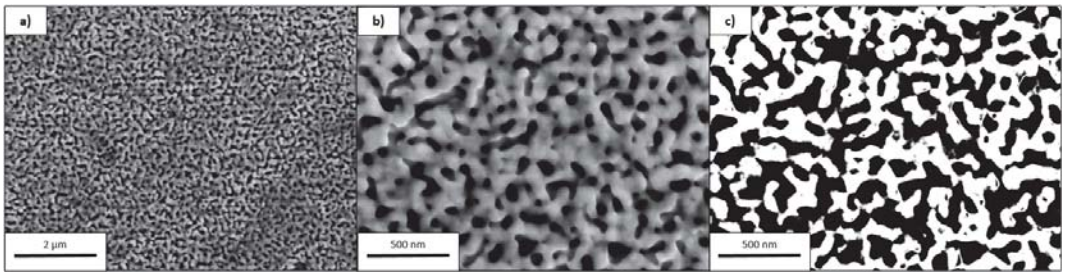

Figure 4.14 SEM images of the Au foam after etching at a) 10000 x, b) 40000 x magnification and c) a binary image created from b) for characterization of the porosity of the foam.

4.6.2. Composition, ligament structure and texture

EDX scans were conducted on the foam to obtain information about the content of remaining iron. Up to 5.5 at.-% Fe could be detected in the np Au, no traces of other elements were found. EBSD scans were executed on the samples (figure 4.15 a)). The analysis of those patterns gives a mean grain size of 70 nm with a narrow distribution, resulting in the fact that the majority of the ligaments have a diameter of about 100 nm and thus are made up of few grains. Information of the black area was not considered since the image quality of the Kikuchi patterns in this zone falls below a critical value of 35 %. The sample has to be tilted 70° for EBSD, therefore the microstructure appears different compared to the horizontal position (figure 4.15 b) & c)).

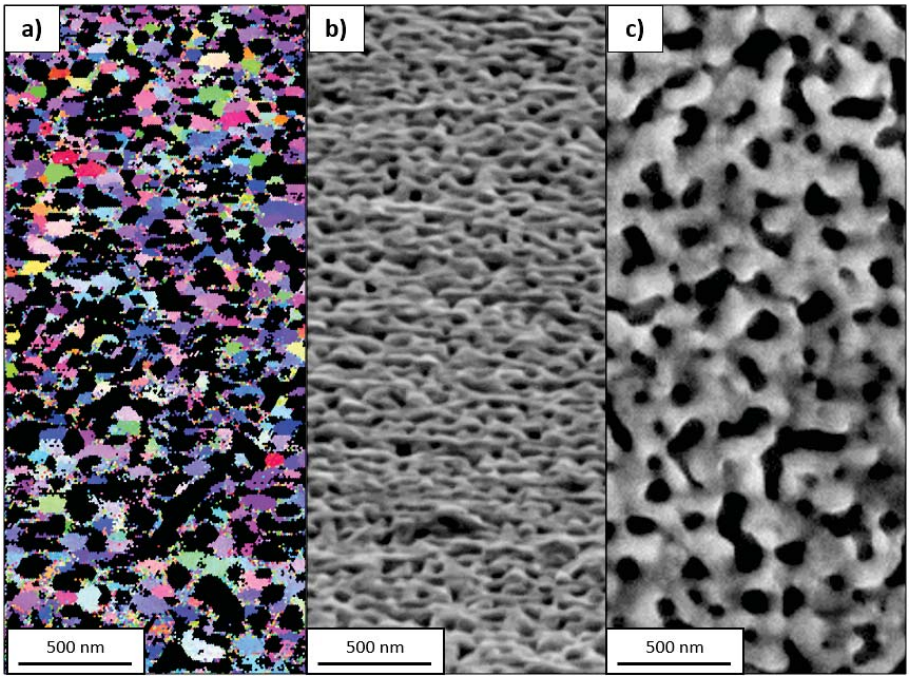

Figure 4.15 a) Structure of the np Au revealed by EBSD. SEM images of b) the tilted position (70°) necessary for EBSD and c) in horizontal position.

As to see in figure 4.16, a texture was noticed when the foam is examined in axial direction close to the edge by EBSD. The analysis determines a distinct preferred orientation of {112} planes.

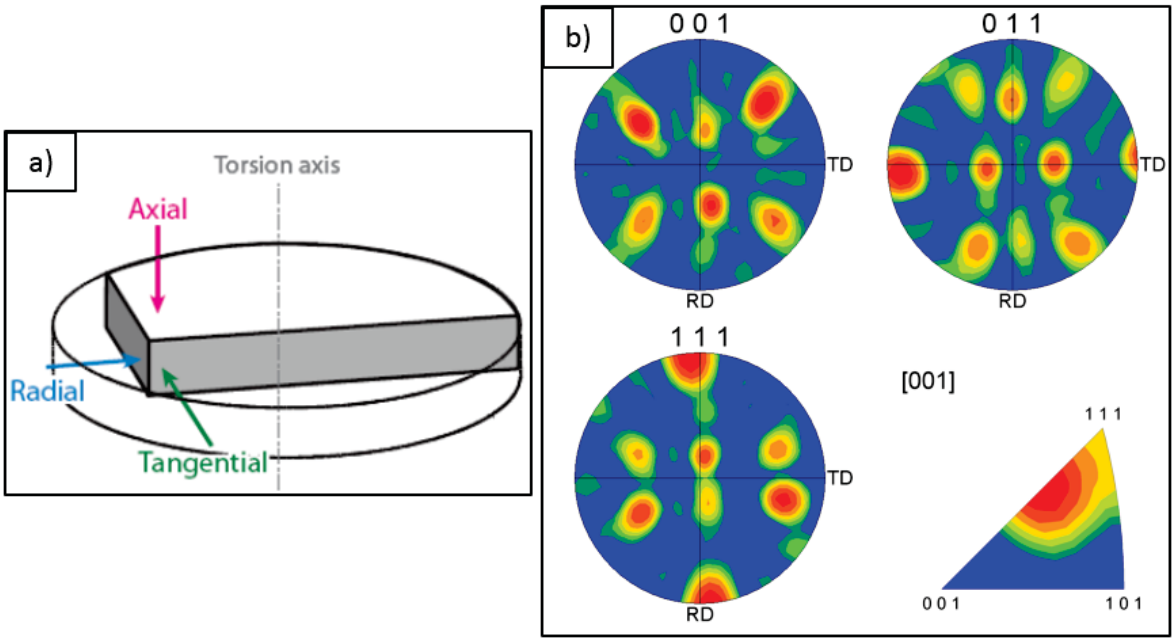

Figure 4.16 a) Coordinate system of the HPT samples. b) Texture illustrated by pole figures and inverse pole figure.

4.6.3. Imbibition effects

In order to exclude errors from absorbed glue or high temperature cement, which is necessary for nanoindentation experiments, samples were fixed with those substances and investigated in an SEM. After drying, cross-sections with a minimum depth of 9 μm were prepared by FIB to proof whether any capillary rise appeared. A platinum layer was deposited prior cutting in order to avoid curtaining and to protect near-surface areas. Fortunately neither superglue, nor cement was absorbed, as is confirmed by SEM images displayed in figure 4.17. The difference in structure might come from different beam currents used for cutting.

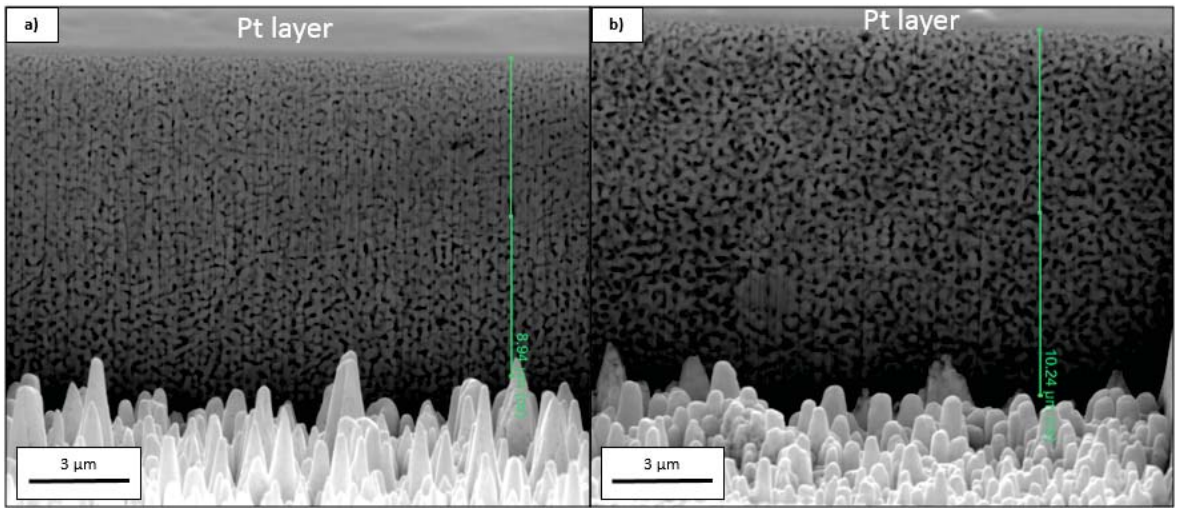

Figure 4.17 SEM micrographs of FIB cross-sections confirming that a) no superglue and b) no high temperature cement is absorbed by the nanoporous gold foam.

4.7. Nanoindentation

As elaborately discussed in section 3.8, at least 70 indents were set at every temperature condition. In order to exclude influences of individual indents, they were spread 40 μm in horizontal as well as vertical direction. An exemplary indent pattern of a np Au sample after executing the experiments is shown in figure 4.18 a). It was abandoned to display all load-displacement curves due to the high number of indents, but an exemplary data is given in figure 4.18 b), depicting a LC measurement on np Au with a dwell time of 30 s. Generally speaking the setup obtained stable and repeatable data during the whole experimental time coming along with low noise levels and low deviations for the measured mechanical values. Indents where thermal drift exceeded $\pm$ 0.3 nm/s were identified and not considered in the data analysis. All plotted values for H and E were obtained from DC measurements with 5 s dwell time.

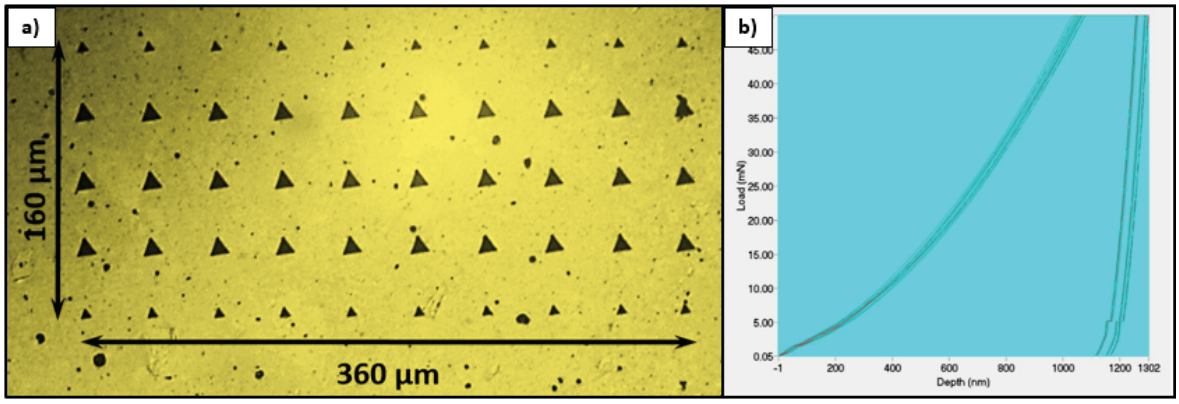

Figure 4.18 a) LM-micrograph of the indent pattern after executing the set schedule and b) exemplified load-displacement curves of LC measurements of a np Au sample at RT.

4.7.1. Young's modulus and hardness of ufg Au

The Young's modulus of ultra-fine grained gold shows a strong decrease with increasing temperature. At ambient temperature the Young's modulus reaches a value of $E = 88.0 \pm 2.0$ GPa which eventually decreases to a level as low as $E = 54.3 \pm 2.7$ GPa at 300 °C (figure 4.19 a)). Just as the modulus the hardness shows a similar trend with a continuous decrease from $H = 1.58 \pm 0.04$ GPa at RT to $H = 0.22 \pm 0.01$ GPa at 300 °C (figure 4.19 b)). Experiments conducted after HT back at RT show significant lower values of E but no change in H compared to measurements prior HT. The consequences of this behavior will be discussed in the section 5.4.1 later on.

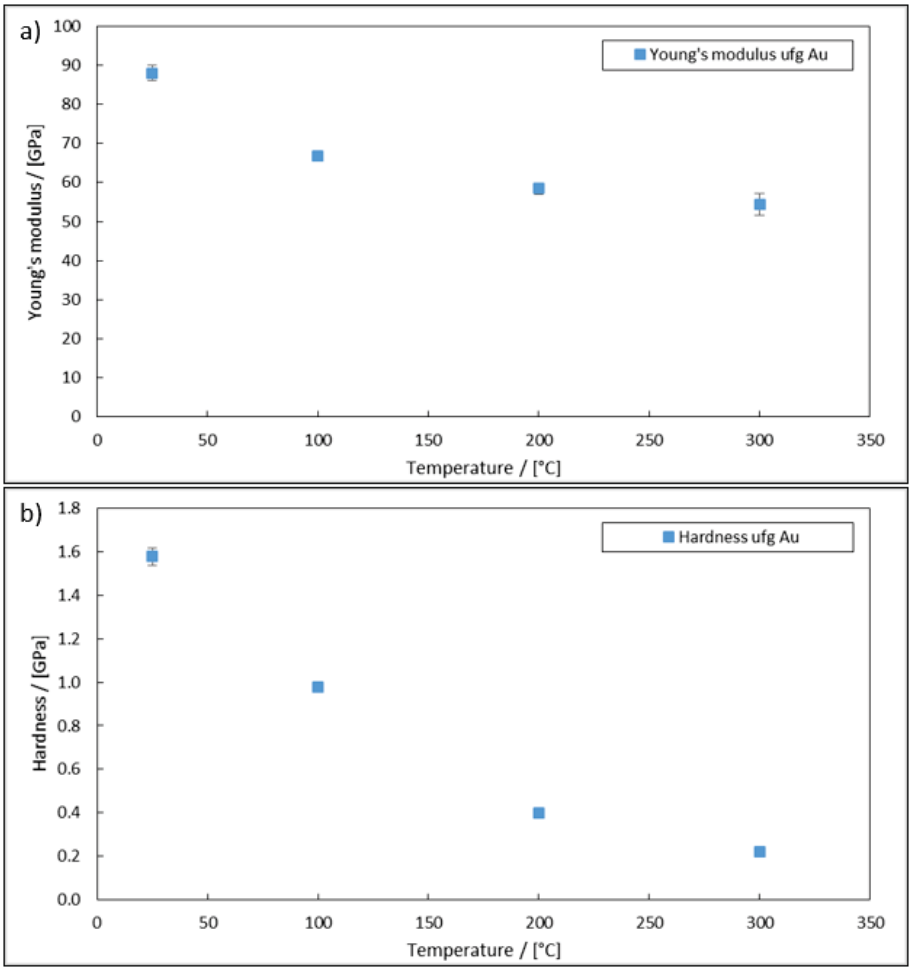

Figure 4.19 Diagrams depicting the a) Young's modulus and b) hardness of ufg Au at temperatures up to 300 °C.

4.7.2. Young's modulus and hardness of np Au

Nanoporous gold shows a different behavior. The initial hardness measured prior HT experiments reveals values with low deviations (< 0.05 GPa) for every prepared disk itself but varies between individual samples with $H = 0.53$ GPa and a standard deviation of 0.14 GPa. Therefore the Young's modulus and the hardness are plotted normalized with regard to the initial hardness of each sample at RT. Contrary to expectations, E increases at 100 °C to 140 % of the RT value, decreases at 200 °C and 300 °C and finally comes up to the highest value at 400 °C as illustrated in figure 4.20 a). The hardness

on the other reaches a level of 128 % after increasing temperature to 100 °C and shows a continuous decrease up to 400 °C where H reduces to 45 % compared to the hardness at RT prior to HT experiments.

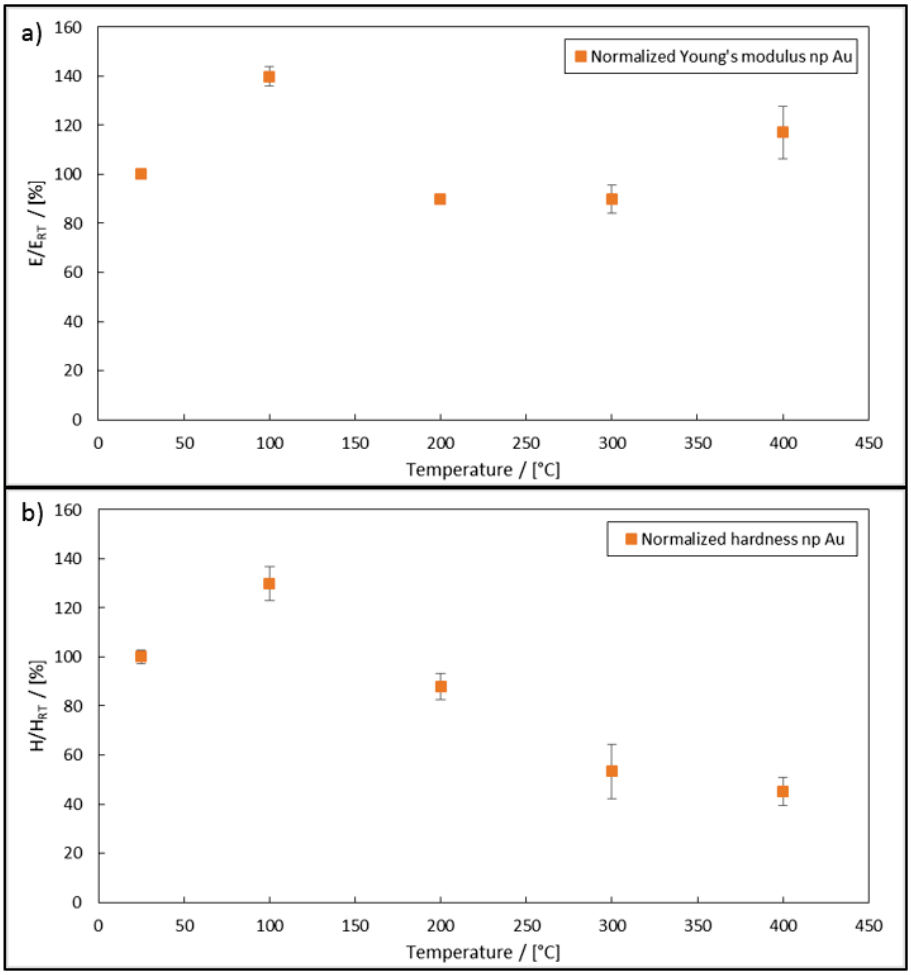

Figure 4.20 Diagrams depicting the relative change of a) the Young's modulus and b) the hardness of np Au at temperatures up to 400 °C with regard to values measured at RT for each sample prior HT tests.

4.7.3. Deformation dynamics

As the grain size of fcc metals decreases, a significant increase of SRS is observed and low activation volumes are measured [45]. In order to avoid the discrepancy of two different values for the SRS which would emerge from the procedure developed by Peykov

et al. [39], mentioned in chapter 2.5.3, the value is displayed in dependence of the corresponding indentation flow stress $\sigma_{\mathrm{f,i}}$. At each temperature at least seven valid indents were made, whereby among one another low deviations occur. In order to provide a clear overview, one representative curve of each condition is displayed in the following diagrams.

4.7.4. SRS, activation volume and activation energy of ufg Au

RT experiments result in m values reaching from 0.06 up to 0.16 with rising dwell time and thus decreasing $\sigma_{f,i}$. When the samples are measured at HT, m shifts to slightly higher numbers accompanied by a reduction of $\sigma_{f,i}$, respectively (figure 4.21). At 300 °C the maximum m value increases to 0.25. The activation volume rises when higher temperatures are reached (figure 4.22). At RT rather low numbers are observed with less than 10 b^3. V^* increases with ascending temperature up to 70 b^3. Furthermore, the activation volume becomes more independent of the indentation flow stress. Finally, the activation energy was determined as described in section 2.5.4, the results of which are depicted in figure 4.23. Between ambient temperature and 100 °C an energy of 5.94 kJ/mol was determined. Further heating up to 300 °C reveals a doubling of the value to 12.73 kJ/mol. Since problems occurred to determine E, which are going to be elaborately discussed later on, literature values of bulk gold samples from Simmons *et al.* [55] were used instead for this calculation.

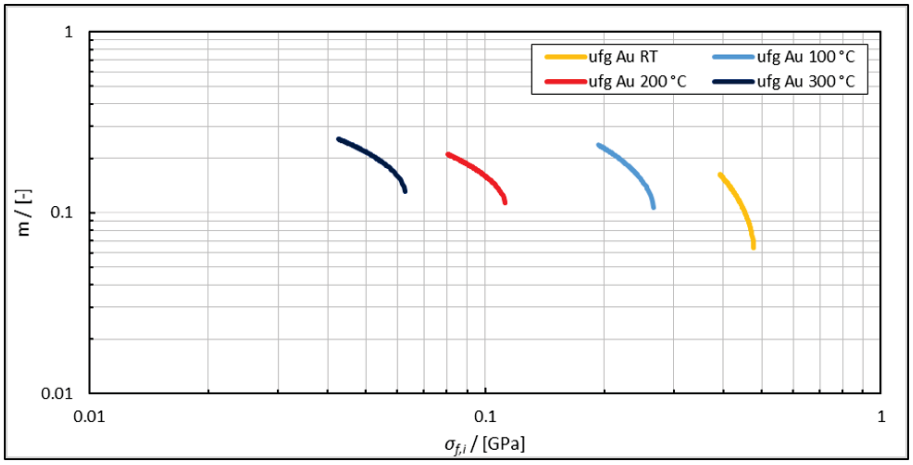

Figure 4.21 Illustration of SRS in dependence of the corresponding indentation flow stress for ufg Au in the range of RT to 300 °C.

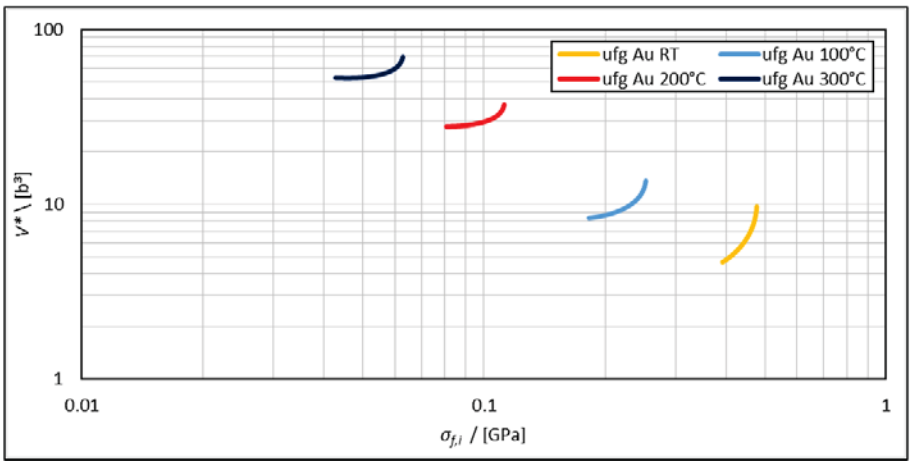

Figure 4.22 Diagram displaying the activation volume of ufg Au at different temperatures in regard to $\sigma_{f,i}$.

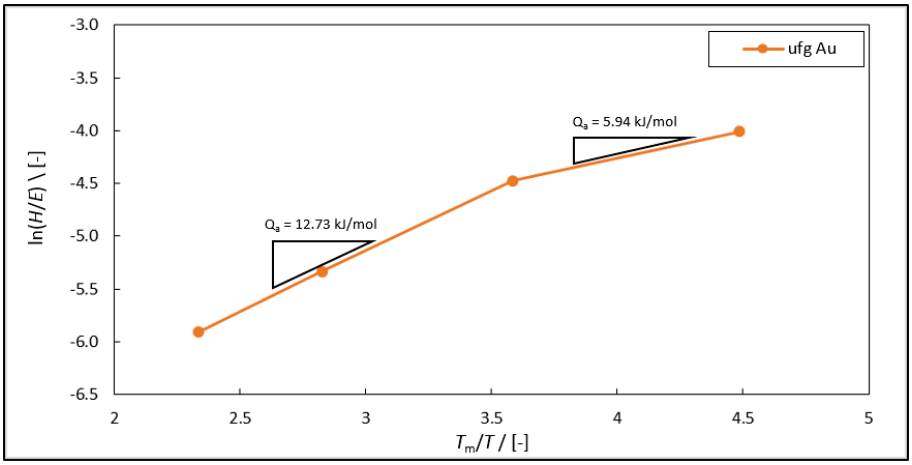

Figure 4.23 Analysis of the activation energy by measuring the slope of a plot $\ln(H/E)$ versus T_m/T.

4.7.5. SRS and activation volume of np Au

At ambient temperature m extends from values starting at around 0.03 and eventually ends up at 0.15. The change of $\sigma_{f,i}$ from 0.13 GPa at the beginning to 0.11 GPa results from creep. High temperature experiments at 100 °C and 200 °C show an increase in hardness, whereas m only shows slight changes and remains at the level observed at RT. The same holds true for 300 °C but the flow stress decreases significantly. The material shows an enormous influence of creep at 400 °C which comes along with a strong increase of the strain-rate sensitivity. The activation volume, considering SRS as well as temperature, constraint factor and hardness, results in values in the range between 10 b^3 and 72 b^3 at RT. It is conspicuous that the values for m at HT never leave the range measured at RT. The spread concerning the hardness may arise from an occurring layer at the surface.

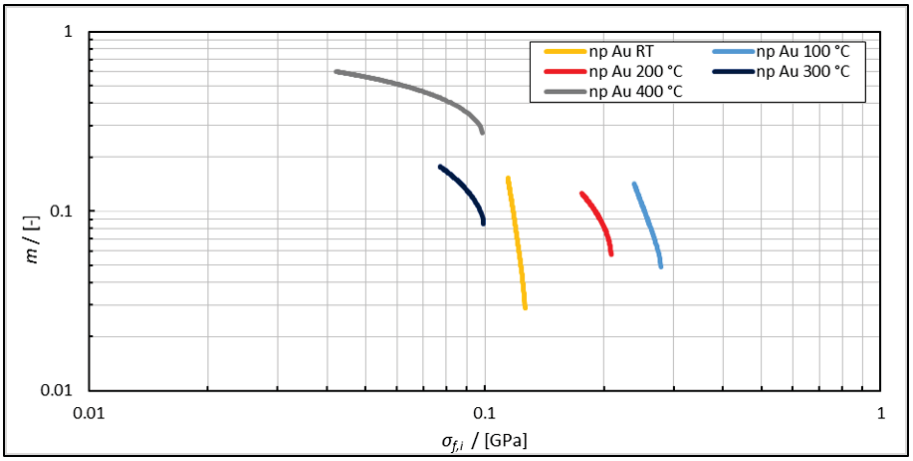

Figure 4.24 Graph of the strain-rate sensitivity for np Au for temperatures up to 300 °C.

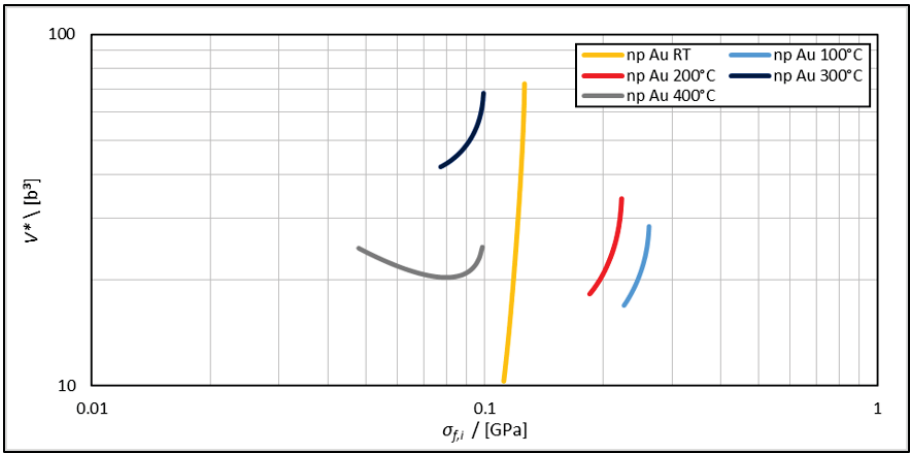

Figure 4.25 Depiction of the resulting activation volume of np Au at different temperatures.

4.7.6. Properties of cg Au at RT

The experiments on annealed cg Au reveal a hardness of 0.87 $\pm$ 0.02 GPa and a Young's modulus 85.3 $\pm$ 2.8 GPa. As expected, the strain-rate sensitivity is low with values ranging from 0.005 to 0.009 and which, considering the hardness, leads consequently to high activation volumes between 126 b^3 and 205 b^3.

4.7.7. Properties nc Au at RT

Values obtained from nc Au show significant higher levels, the hardness reaches 2.8 $\pm$ 0.06 GPa and comes along with a noticeable elevated Young's modulus of 104.6 $\pm$ 1.4 GPa. The analysis of creep data results in a broad range of m from 0.005 to 0.15 and activation volumes between 3 b^3 and 60 b^3.

4.8. FIB investigations

Prepared FIB cross-sections shed light on the dimension of the contamination and revealed that only near-surface areas are affected (figure 4.26). Furthermore, ligaments were measured at this opportunity which exhibit a limited coarsening from 100 nm to around 150 nm when higher temperatures are reached.

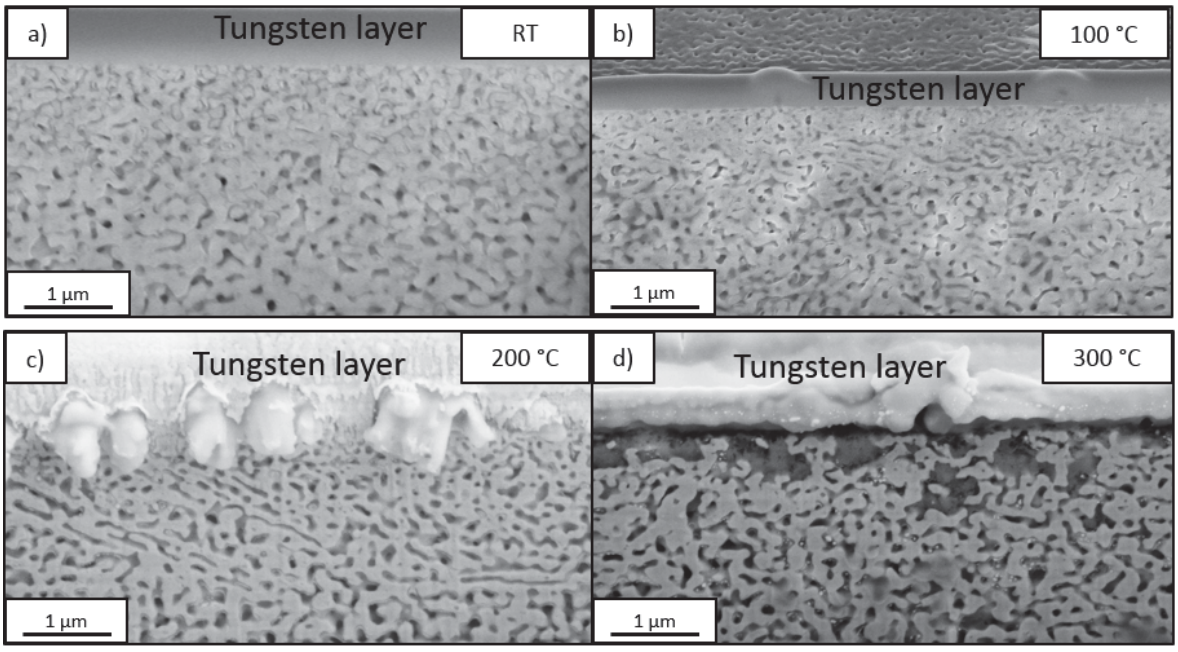

Figure 4.26 Cross-sections of the foam samples after nanoindentation experiments from a) RT to d) 300 °C reveal that just near-surface areas are affected from the absorbed layer.

4.8.1. Indent cross-sections and porosity maps

After nanoindentation experiments the zone beneath the indenter tip was investigated for samples tested at different temperatures (figure 4.27). Unfortunately, the indents of the 200 °C specimen could not be traced, due to local contamination of the area where the indentation schedule was executed. However, SEM images of the made cross-sections show that the deformation changes at higher temperature. In order to achieve a more perspicuous illustration of the plastification, porosity maps, displayed in figures 4.28 a)-c), were generated, following the procedure described in section 3.9.1. Thereby some distinct features are noticed. At RT the densification is concentrated to areas close to the center of the indent and continuous to higher depths. In turn, at 100 °C the plastic deformation is mainly localized to near-surface areas, even areas beside the residual indent seem to have a higher density. Further increasing of T to 300 °C changes the densification behavior again. Even though some dense regions are found, significant less compaction is observed. At some spots the foam actually appears to have a higher porosity than the base material, furthermore one can note that the ligament size slightly increases from 100 nm to 150 nm.

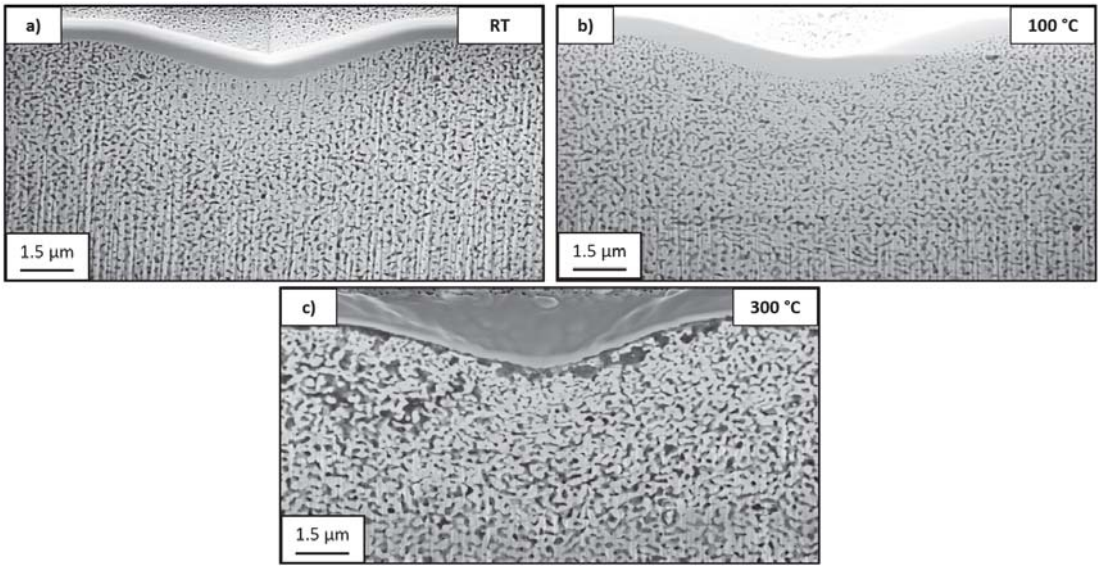

Figure 4.27 SEM images of prepared indent cross-sections of a) RT, b) 100 °C and c) 300 °C experiments.

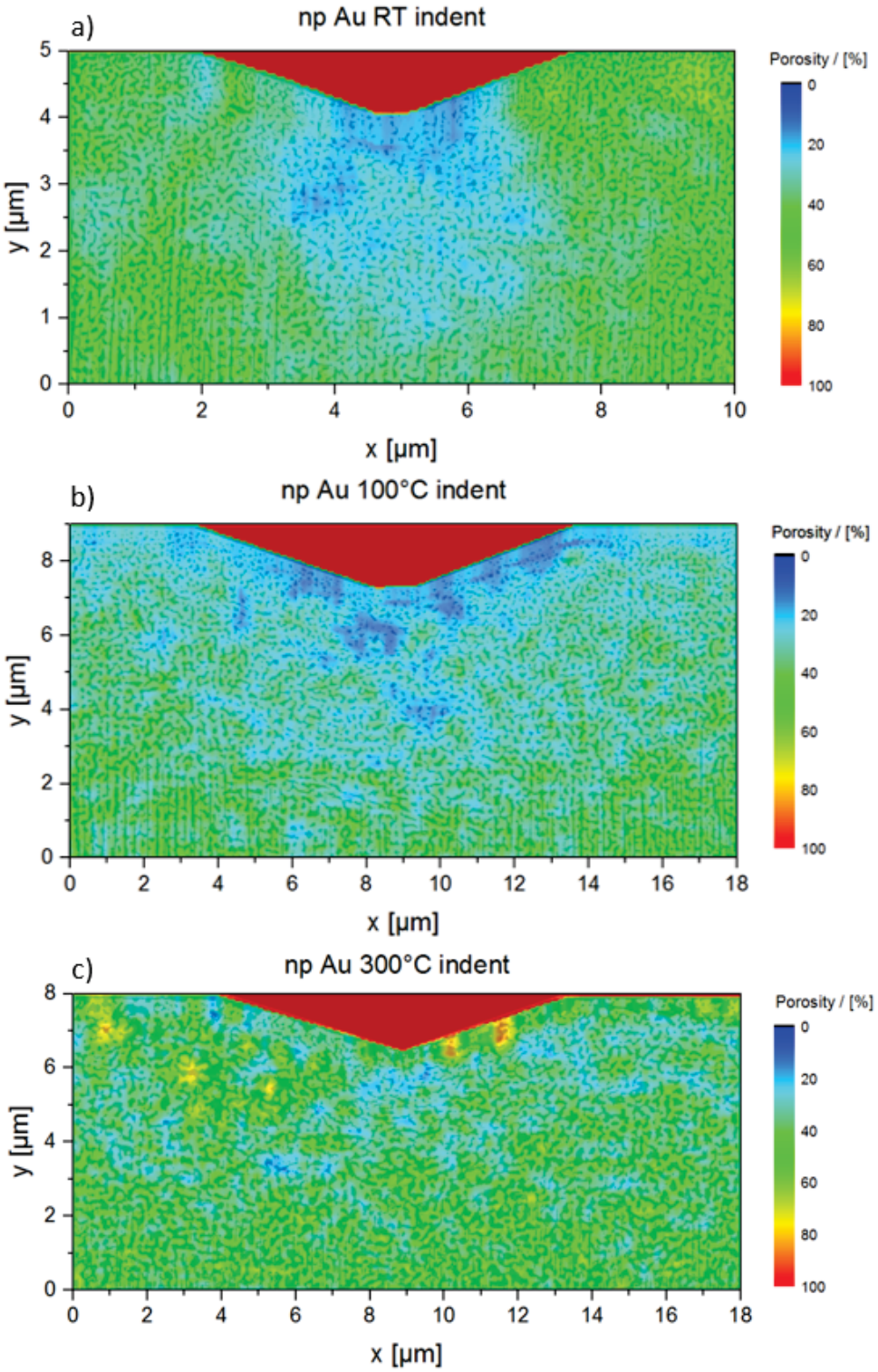

Figure 4.28 Porosity maps with overlaid binary images of the indents of a) RT, b) 100 °C and c) 300 °C experiments.

5. Discussion

5.1. Overview

Several types of specimens were tested at different temperature conditions. Figure 5.1 illustrates the structural dimensions in dependence of T. The coarse grained gold sample was not charted since the grain size exceeds those of the other types by a few orders of magnitude. One can identify that a marginal coarsening of the np and ufg structure takes place when the HT regime is reached. In evidence, beside porosity two other parameters can be ascribed to the nanoporous foam. Therefore both, the ligament diameter and the corresponding grain size at RT, have been plotted in the figure below.

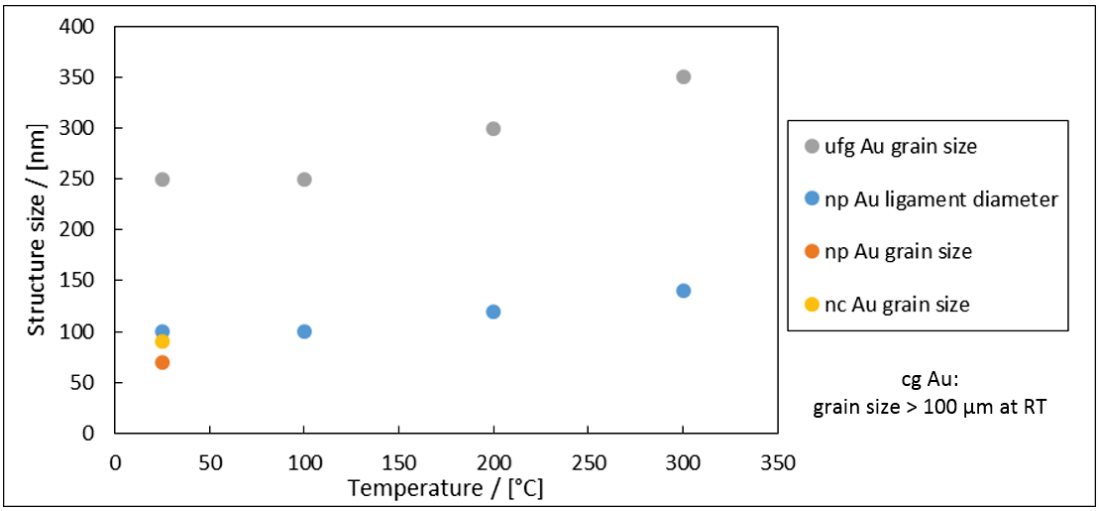

Figure 5.1 Diagram displaying the structure sizes of different sample types at various temperatures.

5.2. Fabrication and structure of np Au

To the best knowledge of the author, np Au has never been produced through powder consolidation, HPT processing and subsequent selective etching so far. Through this report it can be validated that the described proceeding is suitable to fabricate np Au with a unique microstructure. In contrast to np Au made from Au/Ag precursors, were grains comprise several ligaments or the foam features even a single crystalline structure [12, 24] the present foam differs in the grain size which is about 70 nm. For this reason most of the ligaments only contain a few grains and grain boundaries and therefore it is not guaranteed that the values are nonrestrictive comparable to literature data. This fact will be considered in the chapters below. Just as the instant foam, some other HPT deformed materials are known to exhibit a similar shear texture in radial direction, such as Ni investigated by Hafok *et al.* [56] or Al-Mg alloys [57]. However, it has not been reported so far, that this texture also remains, when a np foam is created as per description.

5.3. Nanoindentation at room temperature

5.3.1. Mechanical properties of ufg Au

The RT hardness of ufg Au result in 1.21 GPa $\pm$ 0.04 GPa and is almost identical with the value obtained by microhardness measurements of 1.18 GPa $\pm$ 0.02 GPa. Edalati *et al.* deformed bulk Au via HPT until it reached a steady state grain size of 520 nm with a corresponding hardness of 0.8 GPa [19]. Due to the fabrication of the instant samples, based on Au powder, higher amounts of impurities, which might stabilize the microstructure, remain so that the grain size is significantly lower and reaches around 250 nm. Consequently, the hardness is increasing as the well-known grain boundary hardening (Hall-Petch relation) contributes to higher strengths. Remaining Cu (figure

4.12) could additionally induce solid solution hardening. Overall, the hardness value obtained at RT is considered to be reliable. Likewise, the Young's modulus with a value of 80.3 GPa $\pm$ 1.2 GPa is reasonable, as literature data varies between 57 GPa and 87 GPa [12].

5.3.2. Mechanical properties of np Au

As mentioned in chapter 2.4 the yield strength of the ligaments can be determined by modified Ashby equations allowing for the influence of the ligament size. This results in a ligament yield strength of 1.6 GPa, a value approaching the theoretical strength of gold. Literature data for σ_{th} varies between 1.5 - 8 GPa [12]. Different authors, using nanoindentation techniques, observed ligament strengths in the same order of magnitude. By way of example Hakamada *et al.* [58] obtained values of 5 GPa, otherwise Volkert *et al.* [11] as well as Lee *et al.* [59] measured lower values of around 1.5 GPa but used a constraint factor of 1. In contrast to that, Briot *et al.* [24] performed tensile tests with millimeter-sized samples of polycrystalline and single crystalline np Au. Values obtained by those experiments are significantly lower and estimate a yield strength around 440 MPa in the ligaments.

Even though the determined data for hardness and yield strength show similar results compared with literature data, the procedure has to be critical reflected. One must not forget that the Ashby equations refer to macroscopic low density foams and do not take into account the more complex situation of the nanometer-sized microstructure and consequently different conditions for dislocation motion. However, using the same equations as other authors allows to compare the values, even though it cannot be guaranteed that these lead to the actual intrinsic yield strength of the ligaments.

The appearance of an indent in an SEM image (figure 5.2) confirms that a plastic indentation was produced and that partial compacting near the surface occurs, especially

at the indent center. Additional, the created porosity maps depicted in figure 5.3, demonstrates the dimension of plastic deformation in the material of a RT DC indent. Beneath the center of the tip, a densified region with maximum depth of around 3 μm is noted, where the material experiences a significant reduction of porosity of less than 30 %, marked with the red dashed line. The residual material does not seem to show any signs of distinct consolidation. Furthermore, it was ascertained, that the values of H and E do not vary when the indentation depth is doubled up from 1000 nm to 2000 nm. The outcome of this is, that the densification does not yet influence the mechanical properties when the np Au is penetrated to the set depths.

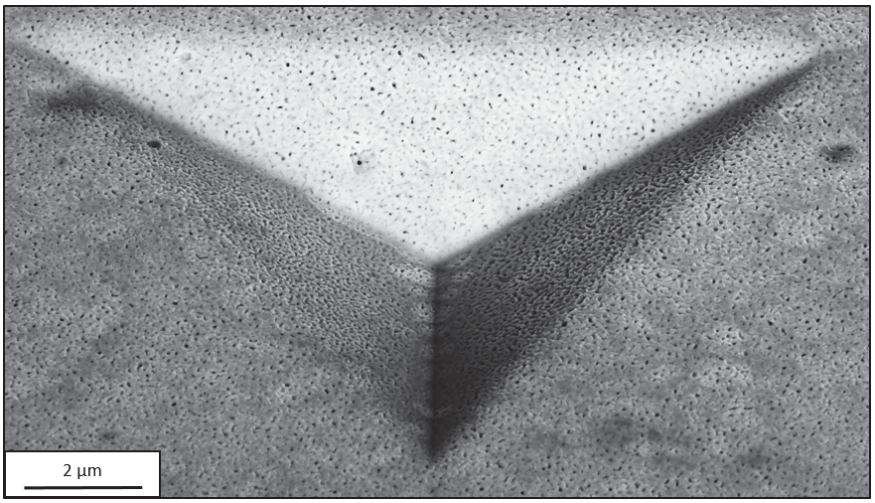

Figure 5.2 SEM micrograph of a 2000 nm np Au indent.

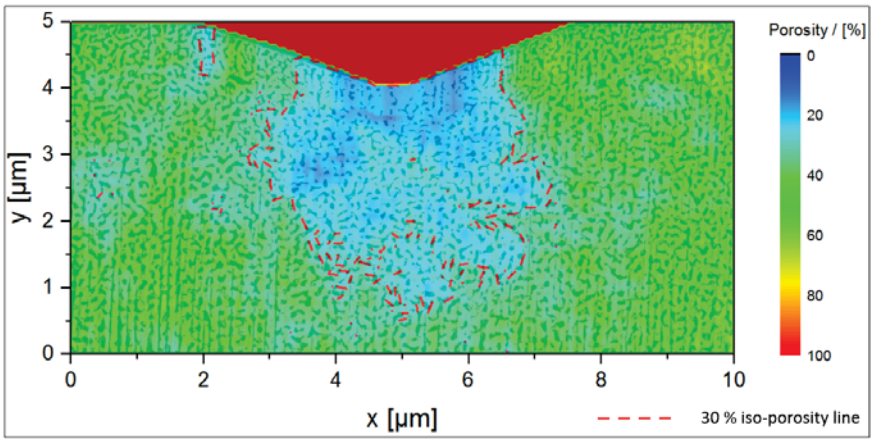

Figure 5.3 Porosity map of a RT indent. The red dashed line relates to a porosity of 30 %.

The present foam was produced in a different way and features a higher density compared to publications cited so far. The pc samples of Briot *et al.* were fabricated through a Au/Ag precursor where grain boundaries still cross a large number of ligaments [24]. Biener *et al.* report from nanograins and therefore an average grain size in the ligaments of around 30 nm [12]. Apparently, the microstructure still differs from the one of the present np Au, which seems to have a narrower grain size distribution, as demonstrated in figure 5.4. Furthermore, the influence of the remaining Fe cannot be appraised so far.

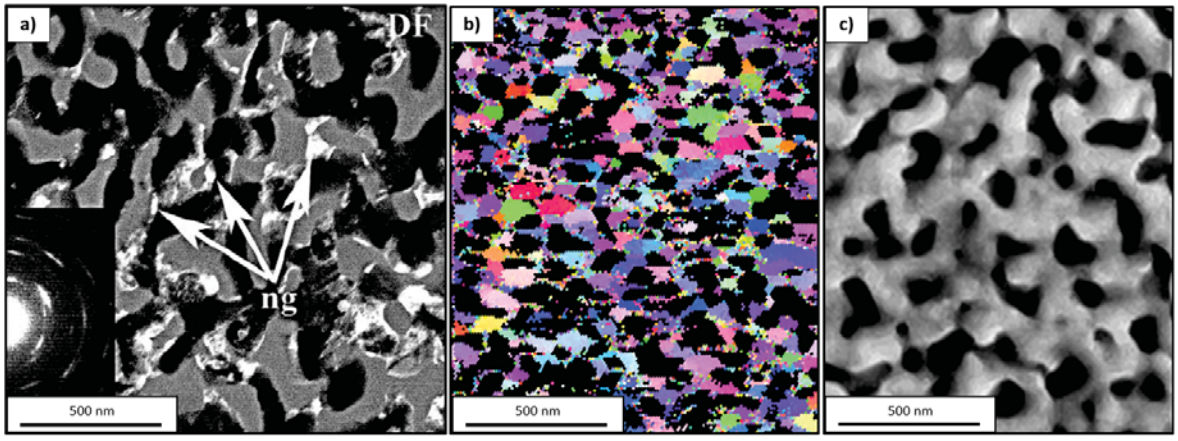

Figure 5.4 Comparison of the microstructure of a) the np Au produced by Biener *et al.* [12] with a Au/Ag precursor and the present foam b) investigated by EBSD and c) SEM secondary electron detector, respectively.

The enormous strength cannot be explained by classical grain boundary hardening resulting from the Hall-Petch relation [8, 9]. Indeed, the instant Au foam has a fine microstructure with an average grain size of about 70 nm, but the data does not fit in a Hall-Petch plot as its strength is considerable higher. For this reason another explanation has to be considered. Hodge *et al.* mention a depletion of dislocations in the nanocrystalline ligaments where consequently new dislocation sources have to be activated, resulting in high yield stresses [26]. Sun *et al.* performed *in-situ* nanoindentation in a TEM and concluded that a constraint dislocation motion and dislocation/dislocation interaction is possible along ligament axes of 15 - 30 nm struts [60].

Recalculating the Young's modulus using equation (2.5) of the ligaments results in 81 GPa, which corresponds with studies of other authors and the fact that E is hardly influenced by the nano-sized microstructure, assuming the Ashby equations as accurate approximation [11] [12] [59].

5.3.2.1. Fracture behavior of np Au

The investigation of a created fracture surface indicates that the material behaves microscopically ductile due to distinctive necking of the ligaments (figure 5.5) even though the macroscopic fracture has a brittle appearance. Same observations were made by other authors [24] [61]. They report strains of more than 200 % for the deformed ligaments and make a highly localized deformation responsible for the macroscopic brittle behavior. Since they could not observe any slip steps in np Au, in contrast to foams with larger ligaments (> 1 μm), they construed a suppression of dislocation activity due to the small dimension of the struts. Hence, approaching of the theoretical strength fits in this theory. However, a total suppression would be contradictory to TEM studies done by Sun *et al.* but it is assumed, that the strictly limited motion of dislocations constitutes a significant increase of yield stress too.

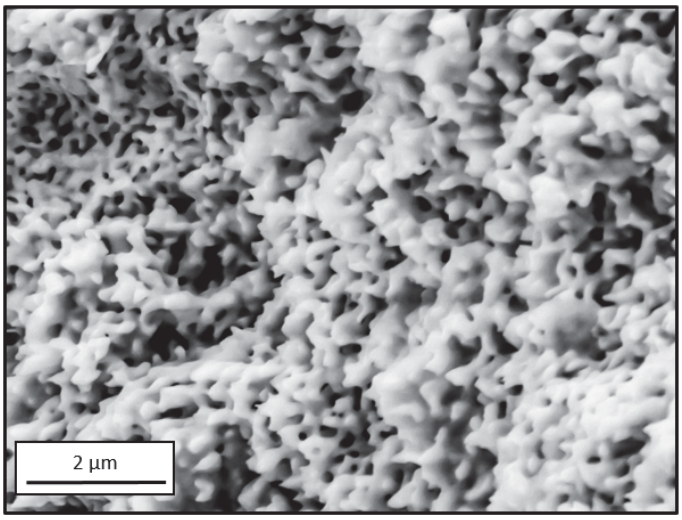

Figure 5.5 SEM micrograph showing the ductile deformation of ligaments on a fracture surface.

5.3.3. Mechanical properties of cg Au

The obtained values at ambient temperature for both hardness and Young's modulus ($H = 0.87$ GPa, $E = 85.3$ GPa) resemble the data provided from Beake *et al.* through nanoindentation [31]. Even though the measured hardness is extraordinary high compared to microhardness experiments, by way of example Matsunaga *et al.* report a hardness of about 0.45 GPa for annealed gold [17], there are several reasons for this effect. Due to grains with mean diameters in the range of mm the indents did not cover a representative volume. Therefore the known pronounced indentation size effect in fcc metals contributes to higher hardness values [62]. Additionally, annealing twins were observed after the heat treatment which may lead to a higher value for H as well. As expected, less creep occurs compared to ufg Au.

5.3.4. Mechanical properties of nc Au

One must consider that the remaining Cu (up to 7 at.-%) could play a crucial role concerning the deformation behavior. Unexpectedly, it was noticed, that the creep depth was considerably lower compared to the ufg counterpart, although the higher grain boundary fraction would let one assume the reverse. It could not be clarified whether precipitations (Au_3Cu) or simple solid solution effects are responsible, since the composition is close to the thermodynamic phase boundary as depicted in the phase diagram in figure 5.6. The diagram was calculated through MTDATA - phase diagram software of the National Physical Laboratory [63].

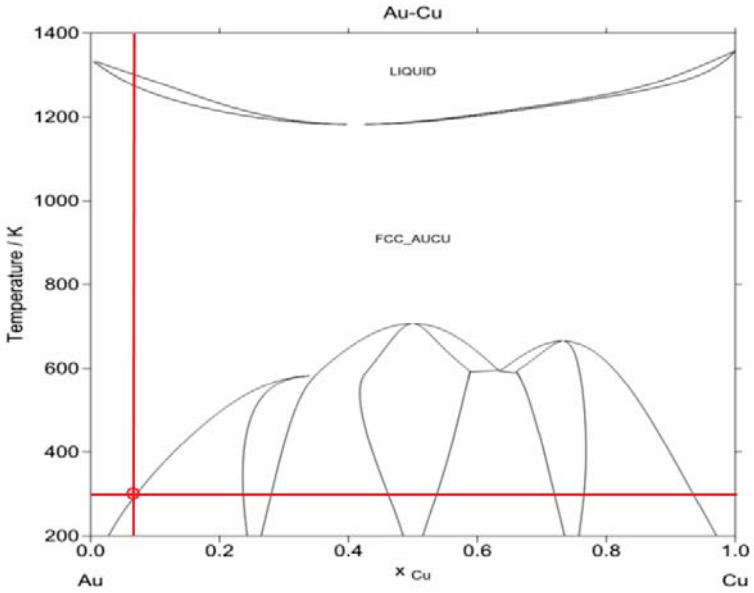

Figure 5.6 Au/Cu phase diagram with marked conditions of the instant nc Au. The position is close to a thermodynamic phase boundary between a Au/Cu solid solution and Au_3Cu precipitations.

5.3.5. Hall-Petch behavior of Au

Two different methods were used to determine the Hall-Petch coefficients. Both are depicted in figure 5.7. As to see in figure 4.12 b), the average grain size simultaneously decreases with increasing Cu amount. Solid solution hardening was assumed to be negligible. Hence, the microhardness profiles can be used to obtain the coefficients for a grain size range between 70 nm and 250 nm. This results in a regression line with a slope of $k = 0.13$ MPa·m$^{\frac{1}{2}}$ and an intercept of 181.34 MPa, linked to the yield strength σ_0 of Au single crystals. On the other hand, nanoindentation data was used to calculate the locking parameter k as well as σ_0. Thereby the properties of the foam were not taken into account, since authors of previous studies reported, that np Au does not follow the Hall-Petch behavior related to bulk gold [26]. However, similar numbers were found compared to the first method, the determined coefficients are $k = 0.19$ MPa·m$^{\frac{1}{2}}$ and $\sigma_0 = 240$ MPa. This data is in good accordance with literature values where k is in the

range between 0.02 and 0.28 MPa $\cdot$ m$^{\frac{1}{2}}$ [64, 65]. The yield strength of Au single crystals was determined to be 20 to 200 MPa [66] but tests on Au nanowires revealed higher values around 330 MPa [26, 64]. The accuracy of the second method is doubtful since not enough data is available to obtain representative numbers.

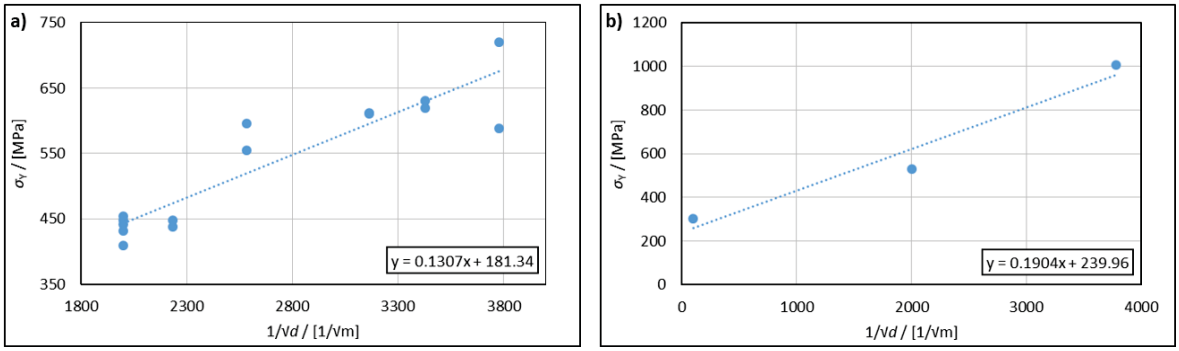

Figure 5.7 Hall-Petch plots determined a) from microhardness measurements and b) from nanoindentation tests.

As mentioned before, the yield strength of np Au ligaments ends up at explicitly higher values of about 1.6 GPa and and does not fit into the Hall-Petch plots. Therefore, it is reasonable to assume that a different deformation mechanism is dominating in this material.

5.4. Nanoindentation at high temperature

5.4.1. Critical reflection of measured data at HT

Comparing the obtained results of ufg Au with literature data [55], especially the Young's modulus, one might speculate that measurement errors occur at high temperature experiments. As indents were made prior and after the HT schedule, it is conspicuous that the Young's modulus drops after HT (figure 5.8). Measuring the sample again with the room temperature setup leads to similar values as gained prior to the HT experiments.

Those changes of the stiffness of the system most likely result from the HT cement. As a consequence, the measured E is disputable. One way to reduce this error is the possibility to calibrate the frame compliance by the presumption that E should reach values determined by Simmons *et al.* [55] in tensile-tests. This leads to a significantly higher frame compliance of up to 1.5 nm/mN, particularly at 200 °C and 300 °C. On the one hand the impact of this error on values for E is enormous, however, on the other hand the error concerning hardness is negligible, as the penetration already reaches depths of more than 1000 nm with loads lower 20 mN. In order to obtain reliable results for the Young's modulus an extensive study on the dependence of frame compliance with different setup methods at different temperatures would have to be done. To avoid errors from thermal drift, equipment with implemented continuous stiffness measurement (CSM) is strongly recommended [40].

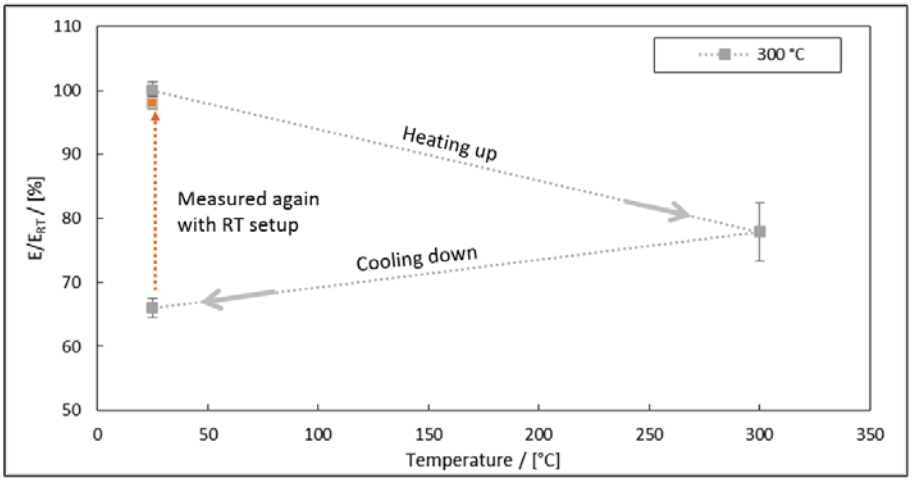

Figure 5.8 Diagram displaying problems of HT measurements at 300 °C. The Young's modulus decreases when measured with the HT setup but comes back to initial values with RT setup.

For the purpose of excluding further errors, indents were investigated in an SEM. The projected area was manually measured using the software ImageJ [54]. The results are consistent with the data obtained directly from nanoindentation and deviate by not more than 10 %. Another problem emerges at HT. SEM micrographs of the indents show that a layer has formed during nanoindentation at elevated temperatures, whereupon the

layer gets more distinctive with increasing temperature. Subsequent EDX measurements detected an appreciable amount of Na, F and Si. Those elements are contained either in the HT cement or the ceramic shielding of the indenter tip. Figure 5.9 shows the surface of np Au after experiments at different temperatures.

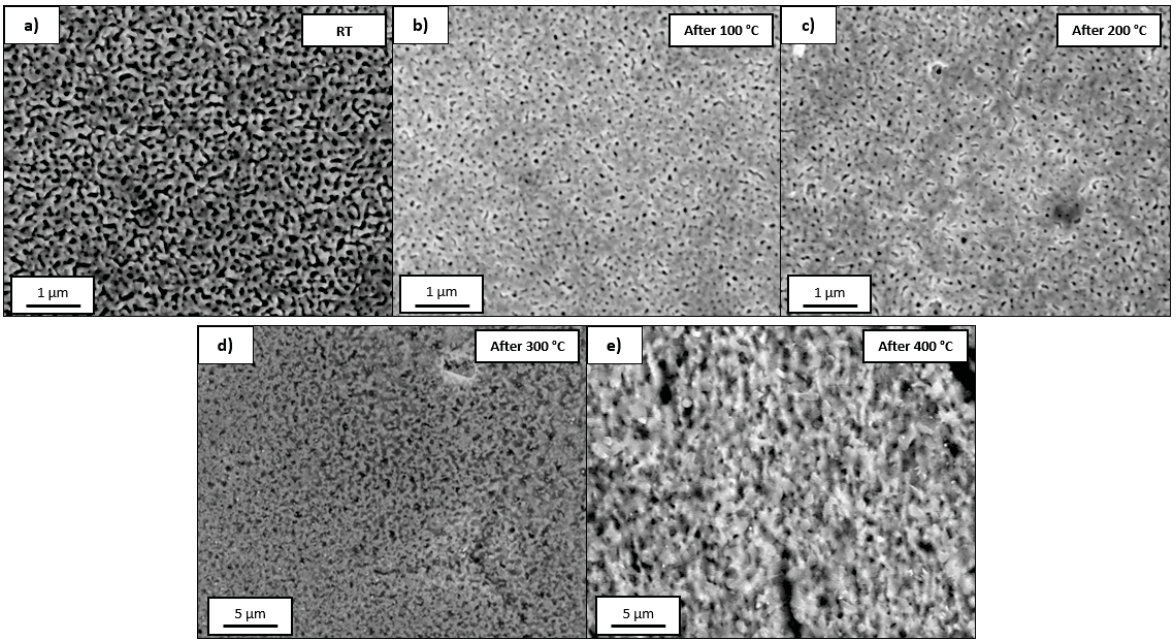

Figure 5.9 SEM images of the instant gold foam after experiments at different temperatures in contrast to the RT structure (a)). After b) 100 °C and c) 200 °C a reduction of porosity is detectable. Particularly at d) 300 °C and e) 400 °C the absorbed layer is well defined.

5.4.2. Mechanical properties at elevated temperatures of ufg Au

A noticeable decrease of hardness is observed when temperature increases. Errors from nanoindentation can be excluded since the projected areas of the indents were measured in an SEM and are in good accordance with the data provided from the Micro Materials software. SEM micrographs reveal a strong change of the microstructure, particularly for gold at 300 °C. At HT the material tries to reduce its total energy by rounding the grains at the surface. Beside this thermal etching process, the indents made at HT appear blurred, which is most likely caused by adhesion effects (figure 5.10). In order

to exclude the occurrence of pores, a bulk cross-section was prepared and confirms that neither pores were formed nor grain growth took place (figure 5.11). Softening effects are known to occur in the HT regime, since grain boundary diffusion processes are activated [67].

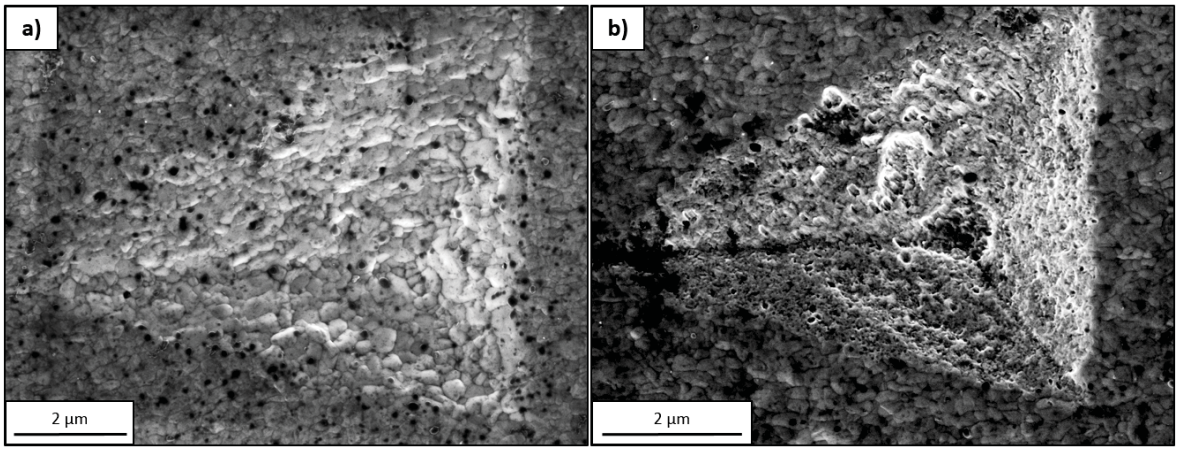

Figure 5.10 SEM images of a) an ufg Au indent made at 300 °C and b) an ufg Au indent made when the sample was again cooled down to RT, showing possible traces of pores at the contact area.

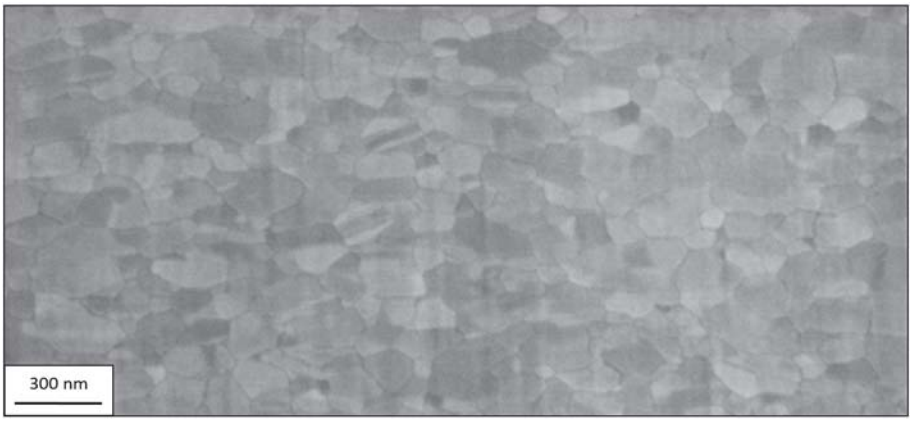

Figure 5.11 FIB bulk cross-section of ufg Au which was tested at 300 °C.

As discussed above, especially the measurement of the stiffness at HT is defective when nanoindentation is used. Even though a slight decrease of E was expected, the obtained data is not reliable and does most likely not reflect the actual Young's modulus of the material. Figure 5.12 demonstrates the difference between data of bulk tests of cg Au

from Simmons *et al.* [55], nanoindentation experiments of Beake *et al.* [31] and the present numbers of ufg Au determined by nanoindentation .

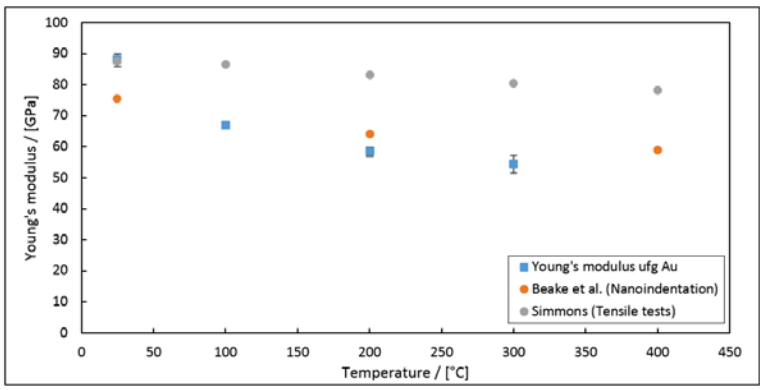

Figure 5.12 Diagram depicting the differences of the measured Young's modulus of ufg Au from this study and another nanoindentation paper [31] compared to bulk data [55].

5.4.3. HT mechanical properties of np Au

Figures 5.9 b)-e) confirm, that the surface of np Au has changed after HT experiments. However, the impact on H and E is hard to assess. Nonetheless, an increase in hardness and modulus at 100 °C is suspicious and suggests that the absorbed layer influences the results. As shown in section 4.7.2 the hardness decreases when the temperature further elevates. It seems that the impact of the forming layer at HT competes with the softening of the foam itself. Therefore, the actual hardness of the pure foam will most likely be overestimated. At 300 °C, for instance, nanoindentation experiments still reveal an intrinsic indentation yield strength of about 1 GPa. A rapid coarsening of the ligaments at higher temperatures, as observed from Seker *et al.* [68], was not noticed for the instant foam (see figure 4.26). To the best knowledge of the author, np Au has never been tested at elevated temperatures before, for this reason data cannot be compared.

5.4.4. Densification behavior of np Au

Interestingly, porosity maps reveal different compaction behaviors at higher temperatures. At RT the porosity map indicates an expected densification in zones of maximum stress beneath the indenter tip compared to the study of Greaves *et al.* for low ν materials (figure 5.13). Otherwise, the compressed areas for 100 °C indents appear more uniformly distributed which most likely results from softening of the material. At 300 °C there is lack of significant densification observed at all. One possible explanation could be enhanced surface diffusion resulting from the high temperature (0.43 $T_{homologous}$). This process is known to have a significant lower activation energy compared to volume or grain boundary diffusion.

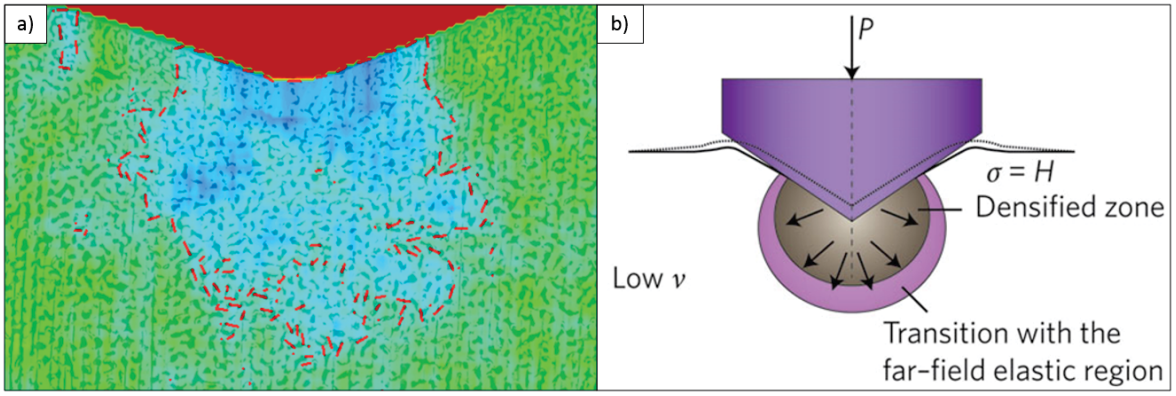

Figure 5.13 Comparison of the observed densified zone of a) the present np Au foam at RT and b) the determined densification after indentation of materials with low Poisson's ration from Greaves *et al.* [69].

5.5. Deformation dynamics

The consideration of SRS and V^* allows to conclude the dominating deformation mechanisms in materials. The following paragraphs will examine the processes for the tested gold structures and finally contrast the diverse behavior.

5.5.1. Deformation mechanisms in ufg Au

Generally, high values for m (0.06 upwards) and consequently low activation volumes (4.5 b^3 upwards) were observed for ufg Au, which is in good accordance with studies on freestanding gold films [70]. Volumes in this order of magnitude are often referred to thermally activated diffusion along grain boundaries and were noticed several times for nc materials [37]. Similar values obtained from nanoindentation strain-rate jump tests were noted for other ufg fcc metals as well, such as Al and Ni [40]. Compression tests at RT and 200 °C, conducted by another research group revealed a moderate increase of V^* at elevated temperatures [71], the same was recognized in the present report. At a constant strain, deformation processes which are ascribed to a small V^* cause a rapid decrease in hardness, when temperature increases [72]. This goes along with observations of the present report, where the ufg gold reaches lower hardness values at 300 °C compared to coarse grained Au measured by Beake *et al.* at 400 °C (figure 5.14) [31].

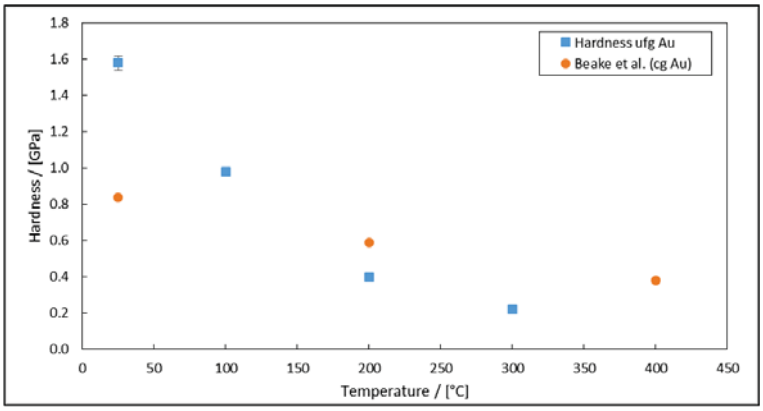

Figure 5.14 Comparison of the hardness of present ufg Au and cg Au measured by Beake *et al.* [31].

The measured activation energy at a homologue temperature between 0.22 and 0.28 T/T_m results in 5.94 kJ $\cdot$ mol^{-1}. In the range between 0.28 and 0.43 T/T_m the activation energy doubles up to 12.73 kJ $\cdot$ mol^{-1}. Examinations on Al suggested that the latter is a value more linked to climbing of dislocations along grain boundaries and the former

is related to lattice-controlled dislocation glide [47] [73]. However, even tough the activation volume slightly rises with increasing temperature, no profound changes of the deformation mechanism are detected. Summed up, the obtained data argue for climbing of edge dislocations which at HT may be accompanied by diffusional processes along grain boundaries.

5.5.2. Deformation mechanisms in np Au

Fortunately, a sufficiently big volume was tested that the influence of the absorbed layer can be neglected for temperatures up to 300 °C. At 400 °C FIB investigations reveal a thickness of the layer of more than 2 μm, thus indents could certainly not reach the np Au regime anymore (figure 5.15). This is further supported by disproportional values for m and V^*. Therefore, the tests at this temperature are excluded from the discussion. A similar behavior compared to ufg Au was observed. The strain-rate sensitivity is hardly affected by the temperature and does not exceed values higher than 0.19. The activation volume reaches values up to 72 b^3 but again no major change of the emerging deformation process was evident. Additionally, it is likely that surface diffusion plays an crucial role because of the high amount of free interphases. This assumption is supported by the investigations of the porosity maps.

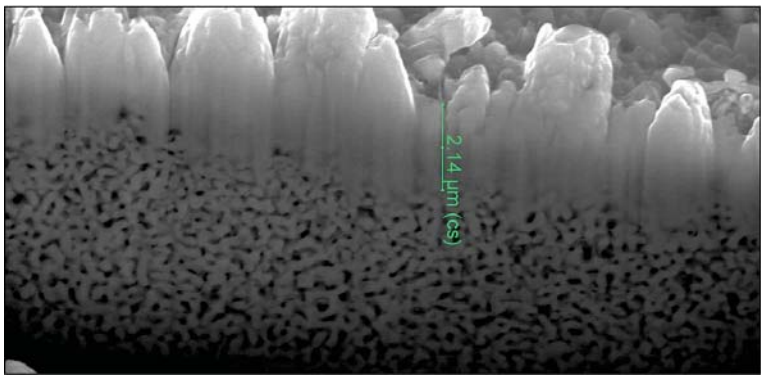

Figure 5.15 FIB cross-section of the 400 °C sample shows that the np material was not reached anymore.

5.5.3. Comparison of various gold structures

At RT four different gold structures were investigated. It is obvious that the coarse grained gold sample shows a significantly higher activation volume ($> 100\ b^3$) whereby this circumstance indicates a differing deformation mechanism compared to the nanostructured counterparts. Through the absence of high fractions of grain boundaries, the plastic deformation is supposed to be driven by the cutting of forest dislocations which are able to glide over wide distances in the grains.

Both, ufg and np Au, show a similar behavior concerning their plastic deformation. It seems that different interphases, grain boundaries as well as free surfaces, have the same effect on the strain-rate sensitivity of materials. The impact of surface diffusion in np Au cannot be appraised so far. Nc Au shows low activation volumes at RT too, presumably stabilizing effects from the solute Cu influence the deformation behavior. In contrast to cg Au, the deformation of these nanostructured materials is most likely governed by the interaction of interphases and dislocations. Figure 5.16 depicts the different structures in an $m/\sigma_{f,i}$ plot. When constant constraint factors are assumed and the difference of the burgers vectors between the charted materials is neglected, iso-activation-volume lines can be inserted. Maier *et al.* have investigated various Al and Ni structures (dashed lines) [40], thus a overview of all these materials can be depicted in figure 5.16. Apparently, coarse grained fcc metals exhibit a significant smaller SRS compared to their ufg or nc counterparts which is associated with different deformation mechanisms. It must be noted, that the measurements on nc and cg Au are more prone to experimental errors, since creep during the 200 s dwell segment is very low (< 40 nm).

In summary, one can assert that the nanostructure is decisively amending the properties of gold, thereby having a crucial impact not only on the material strength, but also on the strain-rate sensitivity and hence on the acting deformation mechanisms in the material.

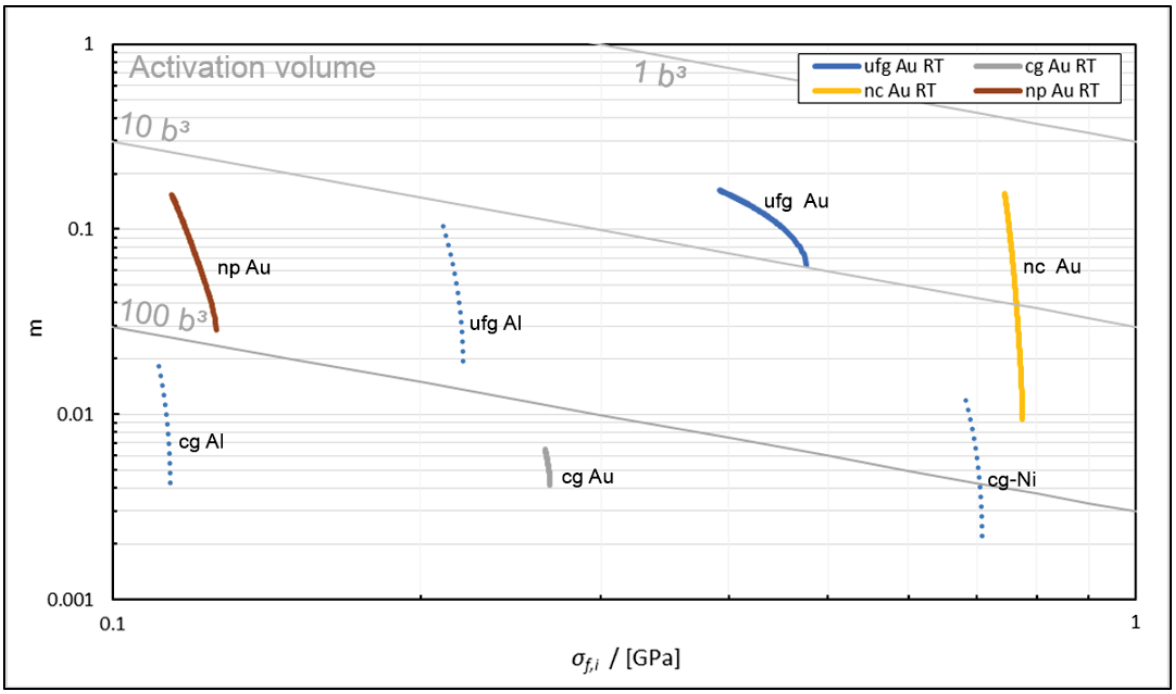

Figure 5.16 Comparison of m and V^* of the tested gold structures at RT, presuming equal constraint factors for all samples. The dashed lines are values for other fcc metals determined by Maier *et al.* [40].

6. Summary and Outlook

As demonstrated, the material fabrication via powder consolidation and subsequent selective etching provides a feasible method to produce np Au foams. An in-depth investigation of the microstructure of ufg and np Au revealed a grain size of 250 nm and a ligament size of 100 nm consisting of grains with an average grain size of 70 nm, respectively. Nanoindentation tests were performed in a temperature range between RT and 400 °C. At ambient temperature a hardness of 1.58 GPa was measured for ufg Au. Following assumptions of Gibson and Ashby for open-cell foams [27] allows to estimate the yield strength of the ligaments of np Au which results in 1.6 GPa. Ufg Au shows a strong decrease of hardness when T increases, np Au on the other hand, exhibits an increase of H at 100 °C followed by a decrease, when temperature is further increasing. It was noticed, that a layer was absorbed when the HT setup was used for np Au, which might be responsible for this behavior.

Creep data recorded at maximum load allows to calculate deformation dynamic parameters, such as the strain-rate sensitivity m and the activation volume V^*. Both, ufg and np Au, show high values of m and low values of V^* at RT and let one assume, that dislocation / interphase interactions are dominating the plastic deformation, resulting from the nanostructure. At higher temperatures no profound change of the emerging deformation mechanism was noticed, even tough m and V^* slightly increased. Cross-sections of the np Au indents, prepared by FIB milling, gave information about the actual deformation beneath the indenter tip. It is not yet clear, why the densified area

is less pronounced at 300 °C. Enhanced surface diffusion could be a possible explanation. This could be proofed by varying the duration of the hold segment during HT indentation. Since diffusion is a time-dependent process, short hold times should then lead to more distinctive densification.

Further investigations of the fabrication procedure would be necessary to identify impacts on the size of ligaments and grains to be able to adjust the desired structure. Nanoindentation technique could be improved by using a device with implemented CSM mode [40] and by using a more thermally stable indenter or by conducting the experiments under vacuum conditions, respectively. Extensive studies should be made for different methods of determining the strain-rate sensitivity in order to avoid errors and to verify that values are comparable without hesitation.

After the optimization of the testing technique further tests on np metal foams with various structure sizes could be conducted to investigate the influence of porosity and ligament diameters. Complementary body centered cubed and hexagonal closed packed metals could be examined to clarify if the same mechanisms are governing the deformation.

New scaling equations for nanoporous materials would be of great interest since deformation mechanisms differ from macroscopic foams. Finally, an conclusive theory could be found which explains the high strength of nano-ligaments and account for the influence of structure size.

Bibliography

[1] A. Wittstock, V. Zielasek, J. Biener, C. M. Friend, and M. Bäumer. Nanoporous gold catalysts for selective gas-phase oxidative coupling of methanol at low temperature. *Science*, 327(5963):319–322, 2010.

[2] W. C. Oliver and G. M. Pharr. An improved technique for determining hardness and elastic modulus using load and displacement sensing indentation experiments. *Journal of Materials Research*, 7:1564–1583, 6 1992.

[3] G. Dehm, J. M. Howe, and J. Zweck. *In-situ Electron Microscopy: Applications in Physics, Chemistry and Materials Science*. John Wiley & Sons, 2012.

[4] M. D. Uchic, D. M. Dimiduk, J. N. Florando, and W. D. Nix. Sample dimensions influence strength and crystal plasticity. *Science*, 305(5686):986–989, 2004.

[5] E. M. Bringa, J. D. Monk, A. Caro, A. Misra, L. Zepeda-Ruiz, M. Duchaineau, F. Abraham, M. Nastasi, S. T. Picraux, Y. Q. Wang, and D. Farkas. Are nanoporous materials radiation resistant? *Nano Letters*, 12(7):3351–3355, 2012.

[6] K. Hu, D. Lan, X. Li, and S. Zhang. Electrochemical DNA biosensor based on nanoporous gold electrode and multifunctional encoded DNA-Au bio bar codes. *Analytical Chemistry*, 80(23):9124–9130, 2008.

[7] Y. Xue, J. Markmann, H. Duan, J. Weissmüller, and P. Huber. Switchable imbibition in nanoporous gold. *Nature Communications*, 5:4237, 2014.

[8] E. O. Hall. The deformation and ageing of mild steel: Discussion of results. *Proceedings of the Physical Society. Section B*, 64(9):747, 1951.

[9] N. J. Petch. The cleavage strength of polycrystals. *J. Iron Steel Inst.*, 174:25–28, 1953.

[10] J. R. Greer and W. D. Nix. Nanoscale gold pillars strengthened through dislocation starvation. *Phys. Rev. B*, 73:245410, Jun 2006.

[11] C. A. Volkert, E. T. Lilleodden, D. Kramer, and J. Weissmüller. Approaching the theoretical strength in nanoporous Au. *Applied Physics Letters*, 89(6):–, 2006.

[12] J. Biener, A. M. Hodge, A. V. Hamza, L. M. Hsiun, and J. H. Satcher. Nanoporous Au: A high yield strength material. *Journal of Applied Physics*, 97(2):–, 2005.

[13] R. W. Boyle. Gold during the pre-classical (primitive) period (5000 b.c. - 600 b.c.). In *Gold*, pages 23–28. Springer US, 1987.

[14] S. Goriely, A. Bauswein, and H. Janka. r-process nucleosynthesis in dynamically ejected matter of neutron star mergers. *The Astrophysical Journal Letters*, 738(2):L32, 2011.

[15] H. E. Boyer and T. L. Gall, editors. *Metals Handbook*. American Society for Metals, 1985.

[16] The University of Sheffield. WebElements: The periodic table on the WWW. http://www.webelements.com/gold/physics.html, 2014.

[17] H. Matsunaga and Z. Horita. Softening and microstructural coarsening without twin formation in fcc metals with low stacking fault energy after processing by high-pressure torsion. *Materials transactions*, 50(7):1633–1637, 2009.

[18] M. L. Jenkins. Measurement of the stacking-fault energy of gold using the weak-beam technique of electron microscopy. *Philosophical Magazine*, 26(3):747–751, 1972.

[19] K. Edalati and Z. Horita. High-pressure torsion of pure metals: Influence of atomic bond parameters and stacking fault energy on grain size and correlation with hardness. *Acta Materialia*, 59(17):6831 – 6836, 2011.

[20] A. P. Zhilyaev and T. G. Langdon. Using high-pressure torsion for metal processing: Fundamentals and applications. *Progress in Materials Science*, 53(6):893 – 979, 2008.

[21] R. Pippan, F. Wetscher, M. Hafok, A. Vorhauer, and I. Sabirov. The limits of refinement by severe plastic deformation. *Advanced Engineering Materials*, 8(11):1046–1056, 2006.

[22] K. Edalati, Y. Ito, K. Suehiro, and Z. Horita. Softening of high purity aluminum and copper processed by high pressure torsion. *International Journal of Materials Research*, 100:12:1668–1673, 2009.

[23] L. J. Gibson and M. F. Ashby. Cellular solids: structure and properties. *Chap*, 11:429–452, 1997.

[24] N. J. Briot, T. Kennerknecht, C. Eberl, and T. J. Balk. Mechanical properties of bulk single crystalline nanoporous gold investigated by millimetre-scale tension and compression testing. *Philosophical Magazine*, 94(8):847–866, 2014.

[25] T. J. Balk, C. Eberl, Y. Sun, K. J. Hemker, and D. S. Gianola. Tensile and

compressive microspecimen testing of bulk nanoporous gold. *JOM*, 61(12):26–31, 2009.

[26] A. M. Hodge, J. Biener, J. R. Hayes, P. M. Bythrow, C. A. Volkert, and A. V. Hamza. Scaling equation for yield strength of nanoporous open-cell foams. *Acta Materialia*, 55(4):1343 – 1349, 2007.

[27] L. J. Gibson and M. F. Ashby. The mechanics of three-dimensional cellular materials. *Proc. R. Soc. Lond. A*, 382 1782:43–59, 1982.

[28] O. B. Olurin, N. A. Fleck, and M. F. Ashby. Deformation and fracture of aluminium foams. *Materials Science and Engineering: A*, 291(1-2):136 – 146, 2000.

[29] A. C. Fischer-Cripps. *Nanoindentation*, volume 1. Springer, 2011.

[30] A. G. Atkins and D. Tabor. Plastic indentation in metals with cones. *Journal of the Mechanics and Physics of Solids*, 13(3):149 – 164, 1965.

[31] B. D. Beake and J. F. Smith. High-temperature nanoindentation testing of fused silica and other materials. *Philosophical Magazine A*, 82(10):2179–2186, 2002.

[32] H. Lüthy, R. A. White, and O. D. Sherby. Grain boundary sliding and deformation mechanism maps. *Materials Science and Engineering*, 39(2):211 – 216, 1979.

[33] R. L. Coble. A model for boundary diffusion controlled creep in polycrystalline materials. *Journal of Applied Physics*, 34(6):1679–1682, 1963.

[34] J. Chen, L. Lu, and K. Lu. Hardness and strain rate sensitivity of nanocrystalline cu. *Scripta Materialia*, 54(11):1913 – 1918, 2006.

[35] B. N. Lucas and W. C. Oliver. Indentation power-law creep of high-purity indium. *Metallurgical and Materials Transactions A*, 30(3):601–610, 1999.

[36] M. J. Mayo and W. D. Nix. A micro-indentation study of superplasticity in Pb, Sn, and Sn-38 wt% Pb. *Acta Metallurgica*, 36(8):2183 – 2192, 1988.

[37] V. Maier, K. Durst, J. Mueller, B. Backes, H. W. Häppel, and M. Göken. Nanoindentation strain-rate jump tests for determining the local strain-rate sensitivity in nanocrystalline Ni and ultrafine-grained Al. *Journal of Materials Research*, 26:1421–1430, 6 2011.

[38] L. O. Nyakiti and A. F. Jankowski. Characterization of strain-rate sensitivity and grain boundary structure in nanocrystalline gold-copper alloys. *Metallurgical and Materials Transactions A*, 41(4):838–847, 2010.

[39] D. Peykov, E. Martin, R. R. Chromik, R. Gauvin, and M. Trudeau. Evaluation of strain rate sensitivity by constant load nanoindentation. *Journal of Materials Science*, 47(20):7189–7200, 2012.

[40] V. Maier, B. Merle, M. Göken, and K. Durst. An improved long-term nanoindentation creep testing approach for studying the local deformation processes in nanocrystalline metals at room and elevated temperatures. *Journal of Materials Research*, 28:1177–1188, 5 2013.

[41] H. Li and A.H.W. Ngan. Size effects of nanoindentation creep. *Journal of Materials Research*, 19:513–522, 2 2004.

[42] G. B. Gibbs. Creep and stress relaxation studies with polycrystalline magnesium. *Philosophical Magazine*, 13(122):317–329, 1966.

[43] Y. M. Wang, A. V. Hamza, and E. Ma. Temperature-dependent strain rate sensitivity and activation volume of nanocrystalline Ni. *Acta Materialia*, 54(10):2715 – 2726, 2006.

[44] M. A. Meyers, A. Mishra, and D. J. Benson. The deformation physics of nanocrystalline metals: Experiments, analysis, and computations. *JOM*, 58(4):41–48, 2006.

[45] Q. Wei, S. Cheng, K. T. Ramesh, and E. Ma. Effect of nanocrystalline and ultrafine grain sizes on the strain rate sensitivity and activation volume: fcc versus bcc metals. *Materials Science and Engineering: A*, 381(12):71 – 79, 2004.

[46] T. Kunimine, T. Aragaki, T. Fujii, S. Onaka, and M. Kato. Inverse temperature dependence of activation volume in ultrafine-grained copper processed by accumulative roll-bonding. *Journal of Materials Science*, 46(12):4302–4307, 2011.

[47] J. M. Wheeler, V. Maier, K. Durst, M. Göken, and J. Michler. Activation parameters for deformation of ultrafine-grained aluminium as determined by indentation strain rate jumps at elevated temperature. *Materials Science and Engineering: A*, 585(0):108 – 113, 2013.

[48] A. Bachmaier, M. Kerber, D. Setman, and R. Pippan. The formation of supersaturated solid solutions in Fe-Cu alloys deformed by high-pressure torsion. *Acta Materialia*, 60(3):860 – 871, 2012.

[49] Marius Kreuzeder. Fabrication and thermo-mechanical behavior of nanoporous copper. Master's thesis, Department of Material Physics, Montanuniversität Leoben, Leoben, Austria, 2013.

[50] Micro materials nanotest user manual.

[51] D. A. Lucca, K. Herrmann, and M. J. Klopfstein. Nanoindentation: Measuring methods and applications. *CIRP Annals - Manufacturing Technology*, 59(2):803 – 819, 2010.

[52] Specification of Omega 700 high temperature cement.

[53] M. Primorac. High-temperature mechanical testing of novel copper niobium

nanocomposites. Master's thesis, Department of Material Physics, Montanuniversität Leoben, Leoben, Austria, 2013.

[54] National Institue of Health. Image processing and analysis in java. http://imagej.nih.gov/ij/, 2004.

[55] G. Simmons and H. Wang. *Single Crytsal Elastic Constants and Calculated Aggregate Properties - A Handbook*. MIT Press, Cambridge, MA, 1971, 1971.

[56] M. Hafok and R. Pippan. Comparison of single crystalline and polycrystalline behavior under high pressure torsion. In *Materials science forum*, volume 550, pages 277–282. Trans Tech Publ, 2007.

[57] A. Bachmaier, M. Hafok, and R. Pippan. Rate independent and rate dependent structural evolution during severe plastic deformation. *Materials transactions*, 51(1):8, 2010.

[58] M. Hakamada and M. Mabuchi. Mechanical strength of nanoporous gold fabricated by dealloying. *Scripta Materialia*, 56(11):1003 – 1006, 2007.

[59] D. Lee, X. Wei, X. Chen, M. Zhao, S. C. Jun, J. Hone, E. G. Herbert, W. C. Oliver, and J. W. Kysar. Microfabrication and mechanical properties of nanoporous gold at the nanoscale. *Scripta Materialia*, 56(5):437 – 440, 2007.

[60] Y. Sun, J. Ye, A. M. Minor, and T. J. Balk. In situ indentation of nanoporous gold thin films in the transmission electron microscope. *Microscopy Research and Technique*, 72(3):232–241, 2009.

[61] J. Biener, A. M. Hodge, and A. V. Hamza. Microscopic failure behavior of nanoporous gold. *Applied Physics Letters*, 87(12):–, 2005.

[62] W. D. Nix and H. Gao. Indentation size effects in crystalline materials: A law for strain gradient plasticity. *Journal of the Mechanics and Physics of Solids*, 46(3):411 – 425, 1998.

[63] National Physical Laboratory. Phase diagram software from the national physical laboratory. http://resource.npl.co.uk/mtdata/mtdatasoftware.htm, 2011.

[64] Y. H. Chew, C. C. Wong, F. Wulff, F. C. Lim, and H. M. Goh. Strain rate sensitivity and hall-petch behavior of ultrafine-grained gold wires. *Thin Solid Films*, 516(16):5376 – 5380, 2008. Thin Films 2006, Singapore.

[65] R. D. Emery and G. L. Povirk. Tensile behavior of free-standing gold films. Part II. Fine-grained films. *Acta Materialia*, 51(7):2079 – 2087, 2003.

[66] S. G. Corcoran, R. J. Colton, E. T. Lilleodden, and W. W. Gerberich. Anomalous plastic deformation at surfaces: Nanoindentation of gold single crystals. *Phys. Rev. B*, 55:R16057–R16060, Jun 1997.

[67] Y. J. Li, X. H. Zeng, and W. Blum. Transition from strengthening to softening by grain boundaries in ultrafine-grained Cu. *Acta Materialia*, 52(17):5009 – 5018, 2004.

[68] E. Seker, J. T. Gaskins, H. Bart-Smith, J. Zhu, M. L. Reed, G. Zangari, R. Kelly, and M. R. Begley. The effects of post-fabrication annealing on the mechanical properties of freestanding nanoporous gold structures. *Acta Materialia*, 55(14):4593 – 4602, 2007.

[69] G. N. Greaves, A. L. Greer, Lakes R. S., and T. Rouxel. Poisson's ratio and modern materials. *Nature Materials*, 10:823–837, 2011.

[70] Benoit Merle. *Mechanical Properties of Thin Films Studied by Bulge Testing*. PhD thesis, Universität Erlangen, 2013.

[71] H. W. Höppel, J. May P., Eisenlohr, and M. Göken. Strain-rate sensitivity of ultrafine-grained materials. *Zeitschrift für Metallkunde*, 96,6:566–571, 2005.

[72] R. W. Cahn, editor. *Thermally activated mechanisms in-in crystal plasticity*, volume 8. Caillard, D. and Martin, J. L., 2003.

[73] J. Shen, S. Yamasaki, K. Ikeda, S. Hata, and H. Nakashima. Low-temperature creep at ultra-low strain rates in pure aluminum studied by a helicoid spring specimen technique. *Materials transaction*, 52(7):1381–1387, 2011.

A. VBA Code

```
Sub User_new()     'launch GUI

    NanoAnalyzer.Show

End Sub
'----------------

Sub refresher()          'Refreshing document

        Application.Calculate

End Sub
'----------------

Sub empiric_fit()  'Numerical solution (least square method) for dwell data fit

    ActiveWorkbook.Sheets("fit_parameter").Select
    SolverReset

    '1 0s - 20s
    SolverAdd CellRef:="$T$4", Relation:=1, FormulaText:="1"
    SolverOk SetCell:="$E$203", MaxMinVal:=2, ValueOf:=0, ByChange:="$T$3:$T$6", _
        Engine:=1, EngineDesc:="GRG Nonlinear"
    SolverSolve UserFinish:=True
    SolverReset

    '1 30s - 200s
    SolverAdd CellRef:="$V$4", Relation:=1, FormulaText:="29"
    SolverOk SetCell:="$K$203", MaxMinVal:=2, ValueOf:=0, ByChange:="$V$3:$V$6", _
        Engine:=1, EngineDesc:="GRG Nonlinear"
    SolverSolve UserFinish:=True
    SolverReset
```

```
    '1 30s
    SolverAdd CellRef:="$X$4", Relation:=1, FormulaText:="1"
    SolverOk SetCell:="$Q$203", MaxMinVal:=2, ValueOf:=0, ByChange:="$X$3:$X$6", _
        Engine:=1, EngineDesc:="GRG Nonlinear"
    SolverSolve UserFinish:=True
    SolverReset

End Sub
'----------------

Sub continuous_m_fit() 'Numerical solution for one single fit over entire 200s data

                ActiveWorkbook.Sheets("Stress_dependent_m").Select
    SolverReset

    '1
    SolverAdd CellRef:="$I$4", Relation:=1, FormulaText:="1"
    SolverOk SetCell:="$E$203", MaxMinVal:=2, ValueOf:=0, ByChange:="$I$3:$I$6", _
        Engine:=1, EngineDesc:="GRG Nonlinear"
    SolverSolve UserFinish:=True
    SolverReset

 End Sub
'----------------

Sub fitDiagram200s()    'Plotting fits in "fit_parameter" for 200s data

    Sheets("fit_parameter").Select

    Range("S44").Select
    ActiveSheet.Shapes.AddChart2(240, xlXYScatterSmoothNoMarkers).Select
    ActiveChart.SeriesCollection.NewSeries
    ActiveChart.FullSeriesCollection(1).Name = "=""Raw data"""
    ActiveChart.FullSeriesCollection(1).XValues = "=fit_parameter!$A$4:$A$202"
    ActiveChart.FullSeriesCollection(1).Values = "=fit_parameter!$C$4:$C$202"
    ActiveChart.SeriesCollection.NewSeries
    ActiveChart.FullSeriesCollection(2).Name = "=""stage a fit"""
    ActiveChart.FullSeriesCollection(2).XValues = "=fit_parameter!$A$5:$A$60"
    ActiveChart.FullSeriesCollection(2).Values = "=fit_parameter!$D$5:$D$60"
    ActiveChart.SeriesCollection.NewSeries
    ActiveChart.FullSeriesCollection(3).Name = "=""stage b fit"""
    ActiveChart.FullSeriesCollection(3).XValues = "=fit_parameter!$G$24:$G$202"
    ActiveChart.FullSeriesCollection(3).Values = "=fit_parameter!$J$24:$J$202"
```

```
    With ActiveChart
        .HasTitle = True
        .ChartTitle.Characters.Text = "Indent 1 - 200s"
        .Axes(xlCategory, xlPrimary).HasTitle = True
        .Axes(xlCategory, xlPrimary).AxisTitle.Characters.Text = "Time / [s]"
        .Axes(xlValue, xlPrimary).HasTitle = True
        .Axes(xlValue, xlPrimary).AxisTitle.Characters.Text = ChrW(916) & "h"
        .Axes(xlCategory, xlPrimary).MinimumScale = 0
        .Axes(xlCategory, xlPrimary).MaximumScale = 210
        .Axes(xlValue, xlPrimary).MinimumScaleIsAuto = True
        .Axes(xlValue, xlPrimary).MaximumScaleIsAuto = True
        .Parent.Top = Range("S44").Top
        .Parent.Left = Range("S44").Left
        .Parent.Height = 250
        .Parent.Width = 600
    End With

End Sub
'---------------

Sub fitDiagram30s()             'Plotting fits in "fit_parameter" for 200s data

                Sheets("fit_parameter").Select

    ActiveSheet.Shapes.AddChart2(240, xlXYScatterSmoothNoMarkers).Select
    ActiveChart.SeriesCollection.NewSeries
    ActiveChart.FullSeriesCollection(1).Name = "=""Raw data"""
    ActiveChart.FullSeriesCollection(1).XValues = "=fit_parameter!$M$4:$M$138"
    ActiveChart.FullSeriesCollection(1).Values = "=fit_parameter!$O$4:$O$138"
    ActiveChart.SeriesCollection.NewSeries
    ActiveChart.FullSeriesCollection(2).Name = "=""stage a fit"""
    ActiveChart.FullSeriesCollection(2).XValues = "=fit_parameter!$M$11:$M$138"
    ActiveChart.FullSeriesCollection(2).Values = "=fit_parameter!$P$11:$P$138"

    With ActiveChart
        .HasTitle = True
        .ChartTitle.Characters.Text = "Indent 1 - 30s"
        .Axes(xlCategory, xlPrimary).HasTitle = True
        .Axes(xlCategory, xlPrimary).AxisTitle.Characters.Text = "Time / [s]"
        .Axes(xlValue, xlPrimary).HasTitle = True
        .Axes(xlValue, xlPrimary).AxisTitle.Characters.Text = ChrW(916) & "h"
        .Axes(xlCategory, xlPrimary).MinimumScale = 0
        .Axes(xlCategory, xlPrimary).MaximumScale = 21
        .Axes(xlValue, xlPrimary).MinimumScaleIsAuto = True
```

```
        .Axes(xlValue, xlPrimary).MaximumScaleIsAuto = True
        .Parent.Top = Range("AA44").Top
        .Parent.Left = Range("AA44").Left
        .Parent.Height = 250
        .Parent.Width = 600
    End With

End Sub

'---------------

Sub mDiagram()  'Plotting of m curves for stage a and b after Peykov et al.

    Sheets("LC_m_dwell").Select

    Range("AO25").Select
    ActiveSheet.Shapes.AddChart2(240, xlXYScatterSmoothNoMarkers).Select
    ActiveChart.SeriesCollection.NewSeries
    ActiveChart.FullSeriesCollection(1).Name = "=""1"""
    ActiveChart.FullSeriesCollection(1).XValues = "=LC_m_dwell!$W$31:$W$157"
    ActiveChart.FullSeriesCollection(1).Values = "=LC_m_dwell!$X$31:$X$157"

    With ActiveChart
        .HasTitle = True
        .ChartTitle.Characters.Text = "m stage a 30s"
        .Axes(xlCategory, xlPrimary).HasTitle = True
        .Axes(xlCategory, xlPrimary).AxisTitle.Characters.Text = "ln strain-rate"
        .Axes(xlValue, xlPrimary).HasTitle = True
        .Axes(xlValue, xlPrimary).AxisTitle.Characters.Text = "ln H"
        .Axes(xlCategory, xlPrimary).MinimumScaleIsAuto = True
        .Axes(xlCategory, xlPrimary).MaximumScaleIsAuto = True
        .Axes(xlValue, xlPrimary).MinimumScaleIsAuto = True
        .Axes(xlValue, xlPrimary).MaximumScaleIsAuto = True
        .Parent.Top = Range("AI23").Top
        .Parent.Left = Range("AI23").Left
    End With

    Range("AO35").Select
    ActiveSheet.Shapes.AddChart2(240, xlXYScatterSmoothNoMarkers).Select
    ActiveChart.SeriesCollection.NewSeries
    ActiveChart.FullSeriesCollection(1).Name = "=""1"""
    ActiveChart.FullSeriesCollection(1).XValues = "=LC_m_dwell!$E$25:$E$44"
    ActiveChart.FullSeriesCollection(1).Values = "=LC_m_dwell!$F$25:$F$44"
```

```
    With ActiveChart
         .HasTitle = True
         .ChartTitle.Characters.Text = "m stage a 200s"
         .Axes(xlCategory, xlPrimary).HasTitle = True
         .Axes(xlCategory, xlPrimary).AxisTitle.Characters.Text = "ln strain-rate"
         .Axes(xlValue, xlPrimary).HasTitle = True
         .Axes(xlValue, xlPrimary).AxisTitle.Characters.Text = "ln H"
         .Axes(xlCategory, xlPrimary).MinimumScaleIsAuto = True
         .Axes(xlCategory, xlPrimary).MaximumScaleIsAuto = True
         .Axes(xlValue, xlPrimary).MinimumScaleIsAuto = True
         .Axes(xlValue, xlPrimary).MaximumScaleIsAuto = True
         .Parent.Top = Range("AI40").Top
         .Parent.Left = Range("AI40").Left
    End With

    Range("AO45").Select
    ActiveSheet.Shapes.AddChart2(240, xlXYScatterSmoothNoMarkers).Select
    ActiveChart.SeriesCollection.NewSeries
    ActiveChart.FullSeriesCollection(1).Name = "=""1"""
    ActiveChart.FullSeriesCollection(1).XValues = "=LC_m_dwell!$N$54:$N$222"
    ActiveChart.FullSeriesCollection(1).Values = "=LC_m_dwell!$O$54:$O$222"

   With ActiveChart
         .HasTitle = True
         .ChartTitle.Characters.Text = "m stage b 200s"
         .Axes(xlCategory, xlPrimary).HasTitle = True
         .Axes(xlCategory, xlPrimary).AxisTitle.Characters.Text = "ln strain-rate"
         .Axes(xlValue, xlPrimary).HasTitle = True
         .Axes(xlValue, xlPrimary).AxisTitle.Characters.Text = "ln H"
           .Axes(xlCategory, xlPrimary).MinimumScaleIsAuto = True
         .Axes(xlCategory, xlPrimary).MaximumScaleIsAuto = True
         .Axes(xlValue, xlPrimary).MinimumScaleIsAuto = True
         .Axes(xlValue, xlPrimary).MaximumScaleIsAuto = True
         .Parent.Top = Range("AI57").Top
         .Parent.Left = Range("AI57").Left
    End With

End Sub
'---------------
```

```
Sub stress_dependent_m_diagramm() 'Displaying stress-dependet m diagramm

    Sheets("Stress_dependent_m").Select
    Range("G44").Select
    ActiveSheet.Shapes.AddChart2(240, xlXYScatterSmoothNoMarkers).Select
    ActiveChart.SeriesCollection.NewSeries
    ActiveChart.FullSeriesCollection(1).Name = "=""1"""
    ActiveChart.FullSeriesCollection(1).XValues = "=Stress_dependent_m!$U$19:$U$187"
    ActiveChart.FullSeriesCollection(1).Values = "=Stress_dependent_m!$T$19:$T$187"

    With ActiveChart
        .HasTitle = True
        .ChartTitle.Characters.Text = "Stress␣dependent␣strain-rate␣sensitivity"
        .Axes(xlCategory, xlPrimary).HasTitle = True
        .Axes(xlCategory, xlPrimary).AxisTitle.Characters.Text = "Stress␣/␣[GPa]"
        .Axes(xlValue, xlPrimary).HasTitle = True
        .Axes(xlValue, xlPrimary).AxisTitle.Characters.Text = "m"
        .Axes(xlValue).ScaleType = xlScaleLogarithmic
        .Axes(xlCategory).ScaleType = xlScaleLogarithmic
        .Axes(xlValue, xlPrimary).MinimumScaleIsAuto = True
        .Axes(xlValue, xlPrimary).MaximumScaleIsAuto = True
        .SetElement (msoElementPrimaryValueGridLinesMinorMajor)
        .SetElement (msoElementPrimaryCategoryGridLinesMinor)
        .Axes(xlCategory, xlPrimary).MinimumScale = 0.01
        .Axes(xlCategory, xlPrimary).MaximumScale = 1
        .Axes(xlValue, xlPrimary).MinimumScale = 0.01
        .Axes(xlValue, xlPrimary).MaximumScale = 1
        .Axes(xlValue).CrossesAt = 0.01
        .Axes(xlCategory).CrossesAt = 0.01
        .Parent.Top = Range("G44").Top
        .Parent.Left = Range("G44").Left
        .Parent.Height = 250
        .Parent.Width = 400
    End With

End Sub
'---------------

Sub CommandButton1_Click() 'Assign functions to command buttons

    TextBox1 = Application.GetOpenFilename

End Sub
```

```
Private Sub CommandButton10_Click()

    Application.Calculate
    Unload Me

End Sub

Sub CommandButton2_Click()

    TextBox2 = Application.GetOpenFilename

End Sub

Sub CommandButton3_Click()

    TextBox3 = Application.GetOpenFilename

End Sub

Sub CommandButton4_Click()

    TextBox4 = Application.GetOpenFilename

End Sub

Sub CommandButton5_Click()

    TextBox11 = Application.GetOpenFilename

End Sub

Sub CommandButton6_Click()

    TextBox12 = Application.GetOpenFilename

End Sub

Sub CommandButton7_Click()

    TextBox13 = Application.GetOpenFilename

End Sub
```

```
Private Sub CommandButton8_Click()

 Application.Calculate
 empiric_fit
 continuous_m_fit

End Sub

Private Sub CommandButton9_Click()

    ActiveWorkbook.Sheets("LC_30s_E_H").Range("B2:L11") = ""
    ActiveWorkbook.Sheets("DC_m_CSR").Range("B2:L11") = ""
    ActiveWorkbook.Sheets("DC_m_CSR").Range("B23:L32") = ""
    ActiveWorkbook.Sheets("DC_m_CSR").Range("B44:L53") = ""

    ActiveWorkbook.Sheets("fit_parameter").Range("T3:T42") = 1
    ActiveWorkbook.Sheets("fit_parameter").Range("V3:V42") = 1
    ActiveWorkbook.Sheets("fit_parameter").Range("X3:X42") = 1
    ActiveWorkbook.Sheets("fit_parameter").Range("A3:B2011") = ""
    ActiveWorkbook.Sheets("fit_parameter").Range("G3:H2011") = ""
    ActiveWorkbook.Sheets("fit_parameter").Range("M3:N2011") = ""

    ActiveWorkbook.Sheets("LC_m_dwell").Range("A3:L12") = ""
    ActiveWorkbook.Sheets("LC_m_dwell").Range("R3:AC12") = ""
    ActiveWorkbook.Sheets("LC_m_dwell").Range("A23:B2031") = ""
    ActiveWorkbook.Sheets("LC_m_dwell").Range("J23:K2031") = ""
    ActiveWorkbook.Sheets("LC_m_dwell").Range("S23:T2031") = ""

    ActiveWorkbook.Sheets("Stress_dependent_m").Range("A3:B2011") = ""
    ActiveWorkbook.Sheets("Stress_dependent_m").Range("I3:I42") = 1
    Application.Calculate

End Sub
'---------------

Private Sub OptionButton1_Click() 'Assign functions to Option Buttons

    If OptionButton1.Value = True Then
        ActiveWorkbook.Sheets("LC_30s_E_H").Range("B16").Value = 0.2
        ActiveWorkbook.Sheets("Overview").Range("G5").Value = 1
        ActiveWorkbook.Sheets("Overview").Range("G4").Value = 0.2884
    End If

End Sub
```

```
Private Sub OptionButton2_Click()

    If OptionButton2.Value = True Then
        ActiveWorkbook.Sheets("LC_30s_E_H").Range("B16").Value = 0.44
        ActiveWorkbook.Sheets("Overview").Range("G5").Value = 3
        ActiveWorkbook.Sheets("Overview").Range("G4").Value = 0.2884
    End If

End Sub

Private Sub OptionButton3_Click()

    If OptionButton3.Value = True Then
        ActiveWorkbook.Sheets("LC_30s_E_H").Range("B16").Value = Val(TextBox5)
    End If

End Sub

Private Sub OptionButton4_Click()

    If OptionButton4.Value = True Then
        ActiveWorkbook.Sheets("LC_30s_E_H").Range("O3") = 0.07
        ActiveWorkbook.Sheets("LC_30s_E_H").Range("O4") = 1142
        ActiveWorkbook.Sheets("LC_m_dwell").Range("AJ6") = 0
        ActiveWorkbook.Sheets("LC_m_dwell").Range("AK6") = 2631.29
        ActiveWorkbook.Sheets("LC_m_dwell").Range("AL6") = 25.44
    End If

End Sub

Private Sub OptionButton5_Click()

    If OptionButton5.Value = True Then
        ActiveWorkbook.Sheets("LC_30s_E_H").Range("O3") = 0.12
        ActiveWorkbook.Sheets("LC_30s_E_H").Range("O4") = 833
        ActiveWorkbook.Sheets("LC_m_dwell").Range("AJ6") = 0
        ActiveWorkbook.Sheets("LC_m_dwell").Range("AK6") = 10193.86
        ActiveWorkbook.Sheets("LC_m_dwell").Range("AL6") = 24.98
    End If

End Sub
```

```
Private Sub OptionButton6_Click()

    If OptionButton6.Value = True Then
        ActiveWorkbook.Sheets("LC_30s_E_H").Range("O3") = Val(TextBox6)
        ActiveWorkbook.Sheets("LC_30s_E_H").Range("O4") = Val(TextBox7)
    End If

End Sub
'----------------

Private Sub TextBox1_Change() 'Assign functions to Textboxes

  Dim sh As Worksheet
  Dim rng As Range
  Dim ConnectionString
  Dim qt As QueryTable

  Set sh = ActiveWorkbook.Sheets("LC_30s_E_H")
  Set rng = sh.Range("A2")
  ConnectionString = "TEXT;" & TextBox1 & "␣"
  Set qt = sh.QueryTables.Add(ConnectionString, rng)
  With qt
    .RefreshStyle = xlOverwriteCells
    .AdjustColumnWidth = False
    .Refresh
  End With

  Set sh = ActiveWorkbook.Sheets("LC_m_dwell")
  Set rng = sh.Range("R3")
  ConnectionString = "TEXT;" & TextBox1 & "␣"
  Set qt = sh.QueryTables.Add(ConnectionString, rng)
  With qt
    .RefreshStyle = xlOverwriteCells
    .AdjustColumnWidth = False
    .Refresh
  End With

End Sub
```

```
Private Sub TextBox11_Change()

Dim sh As Worksheet
  Dim rng As Range
  Dim ConnectionString
  Dim qt As QueryTable

  Set sh = ActiveWorkbook.Sheets("LC_m_dwell")
  Set rng = sh.Range("A3")
  ConnectionString = "TEXT;" & TextBox11 & "␣"
  Set qt = sh.QueryTables.Add(ConnectionString, rng)
  With qt
    .RefreshStyle = xlOverwriteCells
    .AdjustColumnWidth = False
    .Refresh
  End With

End Sub

Private Sub TextBox12_Change()

  Dim sh As Worksheet
  Dim rng As Range
  Dim ConnectionString
  Dim qt As QueryTable

  Set sh = ActiveWorkbook.Sheets("fit_parameter")
  Set rng = sh.Range("A3")
  ConnectionString = "TEXT;" & TextBox12 & "␣"
  Set qt = sh.QueryTables.Add(ConnectionString, rng)
  With qt
    .RefreshStyle = xlOverwriteCells
    .AdjustColumnWidth = False
    .Refresh
  End With
  Set rng = sh.Range("G3")
  ConnectionString = "TEXT;" & TextBox12 & "␣"
  Set qt = sh.QueryTables.Add(ConnectionString, rng)
  With qt
    .RefreshStyle = xlOverwriteCells
    .AdjustColumnWidth = False
    .Refresh
  End With
```

```
  Set sh = ActiveWorkbook.Sheets("Stress_dependent_m")
  Set rng = sh.Range("A3")
  ConnectionString = "TEXT;" & TextBox12 & "␣"
  Set qt = sh.QueryTables.Add(ConnectionString, rng)
  With qt
    .RefreshStyle = xlOverwriteCells
    .AdjustColumnWidth = False
    .Refresh
  End With

  Set sh = ActiveWorkbook.Sheets("LC_m_dwell")

  Set rng = sh.Range("A23")
  ConnectionString = "TEXT;" & TextBox12 & "␣"
  Set qt = sh.QueryTables.Add(ConnectionString, rng)
  With qt
    .RefreshStyle = xlOverwriteCells
    .AdjustColumnWidth = False
    .Refresh
  End With
  Set rng = sh.Range("J23")
  ConnectionString = "TEXT;" & TextBox12 & "␣"
  Set qt = sh.QueryTables.Add(ConnectionString, rng)
  With qt
    .RefreshStyle = xlOverwriteCells
    .AdjustColumnWidth = False
    .Refresh
  End With

End Sub

Private Sub TextBox13_Change()

  Dim sh As Worksheet
  Dim rng As Range
  Dim ConnectionString
  Dim qt As QueryTable

  Set sh = ActiveWorkbook.Sheets("LC_m_dwell")
  Set rng = sh.Range("S23")
  ConnectionString = "TEXT;" & TextBox13 & "␣"
  Set qt = sh.QueryTables.Add(ConnectionString, rng)
```

```
  With qt
    .RefreshStyle = xlOverwriteCells
    .AdjustColumnWidth = False
    .Refresh
  End With

  Set sh = ActiveWorkbook.Sheets("fit_parameter")
  Set rng = sh.Range("M3")
  ConnectionString = "TEXT;" & TextBox13 & "␣"
  Set qt = sh.QueryTables.Add(ConnectionString, rng)
  With qt
    .RefreshStyle = xlOverwriteCells
    .AdjustColumnWidth = False
    .Refresh
  End With

End Sub

Private Sub TextBox14_Change()

    ActiveWorkbook.Sheets("LC_30s_E_H").Range("O3").Value = Val(TextBox14)

End Sub

Private Sub TextBox15_Change()

    ActiveWorkbook.Sheets("LC_30s_E_H").Range("O4").Value = Val(TextBox15)

End Sub

Private Sub TextBox16_Change()

    ActiveWorkbook.Sheets("LC_30s_E_H").Range("O4").Value = Val(TextBox16)

End Sub

Private Sub TextBox17_Change()

    ActiveWorkbook.Sheets("LC_30s_E_H").Range("O3").Value = Val(TextBox17)

End Sub
```

```
Private Sub TextBox18_Change()

    ActiveWorkbook.Sheets("LC_m_dwell").Range("AJ6").Value = Val(TextBox18)

End Sub

Private Sub TextBox19_Change()

    ActiveWorkbook.Sheets("LC_m_dwell").Range("AK6").Value = Val(TextBox19)

End Sub

Private Sub TextBox2_Change()

  Dim sh As Worksheet
  Dim rng As Range
  Dim ConnectionString
  Dim qt As QueryTable

  Set sh = ActiveWorkbook.Sheets("DC_m_CSR")
  Set rng = sh.Range("A2") 'Destination
  ConnectionString = "TEXT;" & TextBox2 & "␣"
  Set qt = sh.QueryTables.Add(ConnectionString, rng)
  With qt
    .RefreshStyle = xlOverwriteCells
    .AdjustColumnWidth = False
    .Refresh
  End With

End Sub

Private Sub TextBox20_Change()

    ActiveWorkbook.Sheets("LC_m_dwell").Range("AL6").Value = Val(TextBox20)

End Sub

Private Sub TextBox21_Change()

    ActiveWorkbook.Sheets("Overview").Range("G6").Value = Val(TextBox21)

End Sub
```

```
Sub TextBox3_Change()

  Dim sh As Worksheet
  Dim rng As Range
  Dim ConnectionString
  Dim qt As QueryTable

  Set sh = ActiveWorkbook.Sheets("DC_m_CSR")
  Set rng = sh.Range("A23") 'Destination
  ConnectionString = "TEXT;" & TextBox3 & "␣"
  Set qt = sh.QueryTables.Add(ConnectionString, rng)
  With qt
    .RefreshStyle = xlOverwriteCells
    .AdjustColumnWidth = False
    .Refresh
  End With

End Sub

Sub TextBox4_Change()

  Dim sh As Worksheet
  Dim rng As Range
  Dim ConnectionString
  Dim qt As QueryTable

  Set sh = ActiveWorkbook.Sheets("DC_m_CSR")
  Set rng = sh.Range("A44") 'Destination
  ConnectionString = "TEXT;" & TextBox4 & "␣"
  Set qt = sh.QueryTables.Add(ConnectionString, rng)
  With qt
    .RefreshStyle = xlOverwriteCells
    .AdjustColumnWidth = False
    .Refresh
  End With

End Sub

Private Sub TextBox5_Change()

    ActiveWorkbook.Sheets("LC_30s_E_H").Range("B16").Value = Val(TextBox5)

End Sub
```

```
Private Sub TextBox8_Change()

    ActiveWorkbook.Sheets("DC_m_CSR").Range("G16").Value = Val(TextBox8)

End Sub

Private Sub TextBox9_Change()

    ActiveWorkbook.Sheets("DC_m_CSR").Range("G37").Value = Val(TextBox9)

End Sub

Private Sub TextBox10_Change()

    ActiveWorkbook.Sheets("DC_m_CSR").Range("G58").Value = Val(TextBox10)

End Sub
```